Worcester Polytechnic Institute
Digital WPI

Masters Theses (All Theses, All Years) | Electronic Theses and Dissertations

2007-01-22

Phase modulating interferometry with stroboscopic illumination for characterization of MEMS

Matthew T. Rodgers
Worcester Polytechnic Institute

Follow this and additional works at: https://digitalcommons.wpi.edu/etd-theses

Repository Citation
Rodgers, Matthew T., "*Phase modulating interferometry with stroboscopic illumination for characterization of MEMS*" (2007). *Masters Theses (All Theses, All Years)*. 1157.
https://digitalcommons.wpi.edu/etd-theses/1157

This thesis is brought to you for free and open access by Digital WPI. It has been accepted for inclusion in Masters Theses (All Theses, All Years) by an authorized administrator of Digital WPI. For more information, please contact wpi-etd@wpi.edu.

Phase modulating interferometry with stroboscopic illumination for characterization of MEMS

A Thesis
submitted to the faculty of the

Worcester Polytechnic Institute

as a partial fulfillment of the requirements for the
Degree of Master of Science
in
Mechanical Engineering

by

Matthew T. Rodgers

15 December 2006

Approved:

Prof. Cosme Furlong, Major Advisor

Prof. Ryszard J. Pryputniewicz, Member, Thesis Committee

Prof. Gretar Tryggvason, Member, Thesis Committee

Mr. Mark Koslowske, Ceranova Corporation, Member, Thesis Committee

Prof. Mark Richman, Graduate Committee Representative

Phase modulating interferometry with stroboscopic illumination for characterization of MEMS

A Thesis
submitted to the faculty of the

Worcester Polytechnic Institute

as a partial fulfillment of the requirements for the
Degree of Master of Science
in
Mechanical Engineering

by

Matthew T. Rodgers

15 December 2006

Approved:

Prof. Cosme Furlong, Major Advisor

Prof. Ryszard J. Pryputniewicz, Member, Thesis Committee

Prof. Gretar Tryggvason, Member, Thesis Committee

Mr. Mark Koslowske, Ceranova Corporation, Member, Thesis Committee

Prof. Mark Richman, Graduate Committee Representative

Copyright © 2006

By

NEST – NanoEngineering, Science, and Technology
CHSLT – Center for Holographic Studies and Laser micro-mechaTronics
Mechanical Engineering Department
Worcester Polytechnic Institute
Worcester, MA 01609-2280

All rights reserved

ABSTRACT

This Thesis proposes phase modulating interferometry as an alternative to phase stepping and phase-shifting interferometry for use in the shape and displacement characterization of microelectromechanical systems (MEMS) [Creath, 1988; de Groot, 1995a; Furlong and Pryputniewicz, 2003]. A phase modulating interferometer is developed theoretically with the use of a stroboscopic illumination source and implemented on a Linnik configured interferometer using a software control package developed in the LabVIEW™ programming environment. Optimization of the amplitude and phase of the sinusoidal modulation source is accomplished through the investigation and minimization of errors created by additive noise effects on the recovered optical phase. A spatial resolution of 2.762 μm over a 2.97 × 2.37 mm field of view has been demonstrated with 4x magnification objectives within the developed interferometer. The measurement resolution lays within the design tolerance of a 500Å ± 2.5% thick NIST traceable gold film and within 0.2 nm of data acquired under low modulation frequency phase stepping interferometry on the same physical system. The environmental stability of the phase modulating interferometer is contrasted to the phase stepping interferometer, exhibiting a mean wrapped phase drift of $\langle \Delta\phi \rangle = 40.1$ mrad versus $\langle \Delta\phi \rangle = 91$ mrad under similar modulation frequencies. Shape and displacement characterization of failed μHexFlex devices from MIT's Precision Compliant Systems Laboratory is presented under phase modulating and phase stepping interferometry. Shape characterization indicates a central stage displacement of up to 7.6 μm. With a linear displacement rate of 0.75 Å/mV under time variant load conditions as compared to a nominal rate of 1.0 Å/mV in an undamaged structure [Chen and Culpepper, 2006].

ACKNOWLEDGEMENTS

First of all, I would like to thank my advisor, Prof. Furlong, and Prof. Pryputniewicz who provided me with the opportunity to study interferometry and MEMS systems at WPI. I would like to thank them and my committee for their assistance and support during my completion of this Thesis research. In addition, I gratefully acknowledge the support of the Center for Holographic Studies and Laser micro-mechaTronics (CHSLT) in Mechanical Engineering Department for the use of their facilities and equipment in my studies.

I would also like to acknowledge and thank Prof. Martin Culpepper and Mr. Shih-Chi Chen from the Precision Compliant Systems Laboratory at MIT for the use of their developed μHexFlex device in my experimental work.

I would particularly like to thank my family, and especially my fiancée Amanda O'Toole, for their assistance and unending support during my work over the last couple of years. Without them, I know I couldn't be where I am today.

TABLE OF CONTENTS

Copyright i

Abstract ii

Acknowledgements iii

Table of contents iv

List of figures vi

List of tables xii

Nomenclature xiii

Objective 1

1. Introduction 2

2. Background 6

2.1 MEMS material property variation 10

2.2 Nondestructive evaluation of MEMS 13

2.3 Interferometric options 15

2.4 Benefits of phase modulating interferometry 23

3. Theoretical analysis of phase modulating interferometry 27

3.1 General derivation of phase modulating interferometry with stroboscopic illumination 28

3.2 Use of sinusoidal reference excitation 32

3.3 Determination of reference excitation amplitude and phase 38

4. Implementation 49

4.1 Experimental system 50

4.2 Software development 54

4.2.1 Installation 58

4.2.2 Operation 59

5. Representative Results 62

5.1 Spatial resolution 62

5.2 Measurement resolution and repeatability 64

5.3 Environmental stability 77

5.4 MEMS application 81

5.4.1 Shape measurement 83
5.4.2 Quasi-static testing 89
6. Conclusions and future work 92
7. References 97
Appendix A. Integration of instantaneous intensity function 105
Appendix B. Additive noise effects on phase modulating interferometry 109
Appendix C. Front panel of the developed LabVIEW™ VI for control of the phase modulating interferometer 115
Appendix D. Block diagram of the developed LabVIEW™ VI for control of the phase modulating interferometer 119
Appendix E. Operation package installation 142
Appendix F. Standard operation flow chart 146
Appendix G. Detailed description of developed user interface 151

LIST OF FIGURES

Fig.	1.1.	Scale of various microscopic systems with comparison to MEMS [Zhang, 2004].	2
Fig.	2.1.	Worldwide revenue forecast for MEMS [MEMS Industry Group, 2006].	7
Fig.	2.2.	Share of MEMS revenues by device, 2007 [MEMS Industry Group, 2006].	7
Fig.	2.3.	MEMS development cycle [Exponent, Inc., 2000].	9
Fig.	2.4.	Variation in residual stress and biaxial modulus across a silicon wafer [Exponent, Inc., 2000].	12
Fig.	2.5.	Michelson interferometer [Kreis, 2005].	16
Fig.	2.6.	Monochromatic, red light, versus white light interferograms of a sample with $>\lambda/4$ step discontinuities demonstrating the ability to connect fringe orders using white light interferometry [Wyant, 2002].	21
Fig.	2.7.	Simulation of the interferometric signal I(t) and how it is integrated over the four quarters of the modulation period [Dubois, 2001].	25
Fig.	3.1.	Quadrature acquisition with stroboscopic illumination [Kuppers, et al., 2006].	35
Fig.	3.2.	Convergence of K_s and K_c for $\psi = 6$ rad, $\theta = 5$ rad and $d = 10\%$.	39
Fig.	3.3.	Convergence rate of K_s and K_c for $\psi = 6$ rad, $\theta = 5$ rad and $d = 10\%$.	40
Fig.	3.4.	Representation of K_s at 15% illumination duty cycle.	41
Fig.	3.5.	Representation of K_c at 15% illumination duty cycle.	41
Fig.	3.6.	Representation of K_s at 10% illumination duty cycle.	42
Fig.	3.7.	Representation of K_c at 10% illumination duty cycle.	42
Fig.	3.8.	Representation of K_s at 5% illumination duty cycle.	43
Fig.	3.9.	Representation of K_c at 5% illumination duty cycle.	43
Fig.	3.10.	Mask defined by the equivalency of K_s and K_c, $d = 5\%$.	45
Fig.	3.11.	Mask defined by the equivalency of K_s and K_c, $d = 15\%$.	45
Fig.	3.12.	Reference excitation amplitude and phase versus illumination duty cycle.	46

Fig. 3.13. Phase constant magnitude versus illumination duty cycle. The optimal operation range shown is within d = 14% to 18.5% and limited to 50% of the maximum magnitude. 47

Fig. 4.1. Schematic representation of PMI system described in this Thesis. 49

Fig. 4.2. Linnik configured interferometer [Wyant, 2002; Kreis, 2005]. 50

Fig. 4.3. PL-A741 quantum efficiency curve, peak λ = 660 nm [PixeLINK, 2006]. 51

Fig. 4.4. OD-620L spectral output showing peak and full width at half modulation points for determination of coherence length, l_c. l_c is determined to be 16.8 nm [Opto Diode, 2006]. 52

Fig. 4.5. Voltage dependent displacement of the actuator used for phase modulation during the experimentation conducted within this Thesis. 53

Fig. 4.6. Sample front panel of developed LabVIEW™ interface. 56

Fig. 4.7. Sample of developed LabVIEW™ block diagram. 57

Fig. 5.1. Recorded USAF 1951 negative glass target with group 7 outlined for containing the smallest resolvable element set [Edmund Optics, Inc., 2006]. 63

Fig. 5.2. Spline-fit intensity profile of pixels extracted along horizontally oriented bars in Group 7 of the USAF-1951 negative glass target. 64

Fig. 5.3. 500Å ± 2.5% goal film NIST traceable gauge used for characterization of optoelectronic holographic methodologies [Veeco Metrology Group, 2002]. 65

Fig. 5.4. Interferograms acquired with phase modulating interferometry (a); and with phase stepping interferometry (b). 67

Fig. 5.5. Sine, cosine and arctangent maps calculated with phase modulating interferometry (a); and with phase stepping interferometry (b). 69

Fig. 5.6. Deviations from planarity as determined by difference analysis using phase modulating interferometry operating at f = 100 Hz, d = 14% indicated a nominal film thickness of 503 Å ± 7 Å under PMI. PSI methods indicated a nominal film thickness of 501 Å ± 7 Å [Furlong, 2007]. 70

Fig. 5.7 Shape of reference flat recovered with sinusoidal modulation operating at f = 10 Hz and demonstrating a surface flatness of $\lambda/4$. 75

Fig. 5.8. Shape difference map, δ, between sinusoidal modulation and phase stepping. Both measurements performed at the operational frequency of f = 10 Hz. The sinusoidal variation, having amplitude of 0.4 nm and frequency of 3.4 cycles/mm, is attributed to a combination of the mean and mean squared errors in both the PMI and PSI systems. These errors are related to the phase modulation parameters and appear with a spatial frequency equal to twice the optical frequency, as explored in Appendix B and Creath [1988; 1992]. 76

Fig. 5.9. Wrapped phase map generated with sinusoidal modulating interferometry imaging a reference flat at f = 100 Hz and d = 14% showing points used in calculation of optical phase drift. 80

Fig. 5.10. Optical phase drift over time recovered with phase stepping interferometry and sinusoidal phase modulating interferometry operating at f = 2 Hz and f = 100 Hz respectively with d = 14%. Under these operating conditions, the PSI method exhibits a mean phase drift 7.5 times that demonstrated with PMI correlating with results presented by Kinnstaetter, et al. [1988] and Sasaki, et al. [1990b]. 80

Fig. 5.11. Scanning electron microscopy image of a prototype μHexFlex device [courtesy of: Shih-Chi Chen, MIT, 2004]. 82

Fig. 5.12. Layered TMA structure of μHexFlex device viewed through a scanning electron microscope [courtesy of: Shih-Chi Chen, MIT, 2004]. 83

Fig. 5.13. Recovered shape of 280 μm diameter central stage μHexFlex. 85

Fig. 5.14. Recovered shape of 375 μm diameter central stage μHexFlex demonstrating damage to the armature structure. 86

Fig. 5.15. Recovered shape of 540 μm diameter central stage μHexFlex using phase modulating interferometry with damage indicated to the TMA and armature structures. 87

Fig. 5.16. Recovered shape of 540 μm diameter central stage μHexFlex using phase stepping interferometry. 88

Fig. 5.17. Relative displacement points on central stage and substrate connection of active TMA. 90

Fig. 5.18. Displacement of the damaged μHexFlex device versus applied voltage as determined through the system developed in this Thesis. 91

Fig. C.1. Settings 1: Basic software controls, Base camera settings, Save Results. 116

Fig. C.2. Settings 2: Image processing settings, Output voltage controls, Save Results. 117

Fig. C.3. Settings 3: Operation/Plot mode, Camera triggering controls, Save Results. 118

Fig. D.1. Block diagram of developed LabVIEW™ system. 120

Fig. D.2. Block diagram case structure set 1. 121

Fig. D.3. Block diagram case structure set 2. 122

Fig. D.4. Block diagram case structure set 3. 123

Fig. D.5. Block diagram case structure set 4. 124

Fig. D.6. Block diagram case structure set 5. 125

Fig. D.7. Default event, when there has been no changes on the user interface, continue program with all prior settings. 126

Fig. D.8. Event structure 1a, when the gamma has been adjusted: Stop the camera feed while adjusting the camera gamma value and restart the camera feed. 127

Fig. D.9. Event structure 1b, when the gamma has been adjusted: adjusting the camera gamma value when the camera is not providing an image feed. 128

Fig. D.10. Event structure 2, if the shutter exposure time has been adjusted, send the new value to the camera system. This setting is not read when the camera is operating in "Low Integrate" trigger mode. 129

Fig. D.11. Event structure 3a, update the current camera trigger settings based on parameters found on the user interface and operate under the new settings. Parameters are explained in Appendix F. 130

Fig. D.12. Event structure 3b, update the current camera trigger settings based on parameters found on the user interface. Deactivate reading of the trigger settings for camera operation. 131

Fig. D.13. Event structure 4, this event enables the "Trigger Update" button on the interface to set triggering parameters on selected camera system. 132

Fig. D.14. Event structure 5a, this event begins the display of the unprocessed camera feed if the trigger signal is being generated at a frequency above 0 Hz. 133

Fig. D.15. Event structure 5b, this event displays the unprocessed camera feed but does not allow for image processing when ether the camera trigger signal is not output or the modulation frequency is set to 0 Hz. 134

Fig. D.16. Event structure 6, this event reads the current value of the "Wrapped Phase Map" and "Modulation" buttons from the user interface. 135

Fig. D.17. Event structure 7, this event sets the gain value of the acquired images based on the currently selected value on the user interface. 136

Fig. D.18. Event structure 8a, this event stops the current image feed to set the pixel addressing mode and value as explained Appendix F. It then re-starts the feed stream and re-opens any image displays if previously enabled. 137

Fig. D.19. Event structure 8b, this event sets the pixel addressing mode and value as explained Appendix F when the camera feed has not been enabled. 138

Fig. D.20. Event structure 9a, Event Structure 9a, this event stops the current camera feed to alter the region of interest (ROI) within camera view both in size and location. ROI values must be multiples of 8 and width/height must be equal for proper display and processing. No error checking has been implemented to ensure that the selected ROI is within the imaging array area. 139

Fig. D.21. Event Structure 9b, this event alters the region of interest (ROI) within camera view both in size and location when camera feed is not previously enabled. Restrictions from figure D.20 apply. 140

Fig. D.22. Event structure 10, this event calculates the modulation and synchronization parameters for output voltage generation based on current UI settings and data read from the excitation parameter file (Default Excel file is excite.xls). 141

Fig. F.1. Turn on the developed code and ensure that the raw camera feed is ready for processing. 148

Fig. F.2. Remove the DC component of the illumination signal and begin modulation output control for image processing. 149

Fig. F.3. View the wrapped phase map or the optical modulation map and save the results to the selected directory. End the program using the implemented program stop. 150

LIST OF TABLES

Table	2.1.	Microsensor families.	8
Table	2.2.	Comparison of phase evaluation methods without a spatial carrier Sasaki, et al., 1986a; [Dorrio and Fernandez, 1998; Dubois, 2001, Kreis, 2005].	24
Table	3.1.	Reference excitation amplitude and phase versus illumination duty cycle.	46
Table	4.1.	System connectivity chart.	50
Table	5.1.	Shape measurement comparison between sinusoidal modulation and phase stepping.	75
Table	5.2.	Mean optical phase map drift under phase stepping interferometry at f = 2 Hz and sinusoidal modulating interferometry at f = 10 Hz and 100 Hz.	81
Table	5.3.	μHexFlex quasi-static loading conditions.	89
Table	E.1.	Virtual instruments installed with LabVIEW™ IMAQ modules.	143
Table	E.2.	Programming control blocks required for operation of the PixeLINK PL-741 monochrome CMOS camera system.	144

NOMENCLATURE

$\langle\ \rangle$	infinite time average
$\langle \Delta\phi \rangle$	mean optical phase map drift, mrad
$\langle X \rangle_{\text{rms}}$	geometric or root-mean-squared average of data set x
α	reference modulation phase, rad
$\Delta\lambda$	spectral output width at half output power
$\Delta\phi$	Unwrapped recovered optical phase, rad
$\Delta\psi_{actual}$	actual modulation step during phase stepping
$\Delta\psi_{ideal}$	ideal modulation step during phase stepping
Δt	Acquisition time, sec
ε	optical phase error, rad.
ε_{XY}	strain component in XY-plane
γ	fringe contrast
λ	wavelength of illumination source
λ_0	primary diode output wavelength
η	tangent of the optical phase with additive noise contribution
ψ	mirror excitation phase, rad
σ	standard deviation of data set x
σ_{XY}	stress component in XY-plane
ϕ	interference phase distribution, rad
ϕ_R	reference phase modulation, rad
Σ_s, Σ_c	linear combinations of four sequential frames
θ	relative phase between illumination and reference modulation
ω	reference mirror excitation frequency, rad angular frequency of illumination
d	illumination/camera exposure duty cycle
f_0	natural frequency of an unloaded piezoelectric actuator
f_0'	natural frequency of a piezoelectric actuator with additional mass
i, j	orthogonal coordinates

k	wave number, $2\pi/\lambda$
k_z	wave vector, wave number taken in the z-direction
l	optical path length, reference arm
l_c	coherence length of illumination source
l_l	line length of the USAF 1951 target
m	power series index
m_{eff}	effective mass of a piezoelectric actuator equal to 1/3 the mass of the ceramic stack
n	general Gaussian zero mean additive noise contribution
n'	total number of elements in data set x
n_1, n_2, n_3, n_4, n_p	additive noise on sequential frames, Gaussian zero mean noise
p	acquired frame number: 1,2,3, or 4
t	time, sec
$t_{\min}$	minimum settling time of a piezoelectric actuator.
x	one to multi-dimensional data set
x_{ij}, x_k	data point within data set x
(x,y)	spatial coordinates on the imaging array
z	amplitude of sinusoidal phase modulation, nm
CD	compact disk containing installation files included with this Thesis
CMOS	complementary metal oxide semiconductor
D	optical path length difference
$\|D\|$	mean absolute deviation
E	isotropic modulus of elasticity
E_0	electrical field strength of a planar illumination wavefront
E_1, E_2, E_3, E_4, E_p	discreet complex amplitude of sequential frames, frame: 1, 2, …p
G	isotropic bulk modulus
I	intensity of an illumination source
I_1, I_2, I_3, I_4, I_p	continuous complex amplitude of sequential frames, frame: 1, 2, 3 …p
I_B	instantaneous photon flux or unmodulated dc component of an illumination intensity

$\bar{I}_B$	average photon flux or unmodulated dc component of an illumination intensity
I_M	instantaneous modulated irradiance intensity
$\bar{I}_M$	average modulated irradiance intensity
IRQ	inter-quartile range
$J_n(Y)$	*n*-order Bessel function of the first kind, with respect to variable y
K_s, K_c	sine and cosine phase constants, respectively
LIGA	acronym for a German fabrication process involving **Li**thographie, **G**alvanoformung, **A**bformung
M	additional mass coupled to a piezoelectric actuator
MEMS	microelectromechanical systems
N	N-bucket phase stepping algorithm
N_s, N_c	summed additive noise contribution
NDE	nondestructive evaluation
NIST	National Institute of Standards and Technology
OEHM	optoelectronic holographic methods
PMI	phase modulating interferometry
PSI	phase-shifting interferometry
Q_{XY}	stiffness matrix, *XY* component
R	Pearson product-moment correlation coefficient
ROI	region of interest within a full field of the imaging array
RMS	root-mean-square
T	reference modulation period, sec
TMA	thermomechanical actuator
UI	user interface
V	interference fringe contrast or the magnitude of the complex quantity whose phase describes the position of the constructive and destructive interference regions relative to a reference
X, Y	arbitrary constants
Z	recovered shape, nm

OBJECTIVE

The objective of this Thesis is the review and implementation of a wavefront sensing technology as an alternative to traditional phase stepping or phase-shifting methodologies. It is expected that this will allow for a reliable measurement resolution of 1 nm, or better, allowing for nondestructive shape and displacement characterization of MEMS devices. This Thesis will compare results obtained under multiple modulation frequencies to those obtained with low frequency phase-shifting interferometry to demonstrate the quality of the developed system under high modulation frequencies.

1. INTRODUCTION

Microelectromechanical systems (MEMS) have evolved from the integrated circuit (IC) industry as an effort to radically miniaturize the scale of electromechanical systems while increasing performance and decreasing the cost of the final product. These goals evolved from the success of the IC industry with their bulk-fabrication techniques and their incredible economies of scale [Judy, 2001]. Today, MEMS has come to represent an entire field of systems in the nanometer to millimeter size, excepting IC devices, where the smallest characteristic dimension is on the order of a micron [Judy, 2001; Hsu, 2002; Pryputniewicz, 2005; Kuppers, et al., 2006]. The scale of these devices from ~10 nm to 1 mm is shown in Fig. 1.1 relative to other common microscale and mesoscale systems.

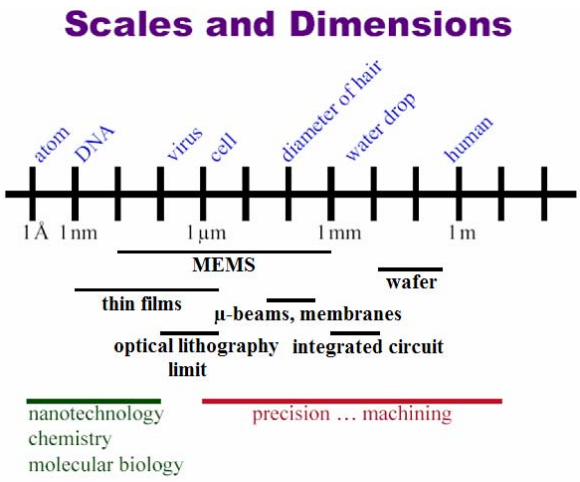

Fig. 1.1. Scale of various microscopic systems with comparison to MEMS [Zhang, 2004].

During the development of early MEMS devices, it became apparent that bulk, continuum material property data could no longer be applied when working at scales

where crystalline structure and thermo-mechanical fabrication effects became dominant factors. At the microscale, these effects create variations in material properties between and within fabrication batches [Osterberg and Senturia, 1997; Rai-Choudhury, 2000]. Similarly, miniaturization required a new approach to system design due to the effects of force scaling. To ensure that MEMS devices function as designed, many are enabled with integrated microstructures for in-situ measurements of material properties [Liwei, et al., 1997; Osterberg and Senturia, 1997; Sandia, 2006]. However, these microstructures require additional space on the fabrication wafers that could be spent providing additional mechanical complexity or allowing for an increase in the number of devices and hence an improvement in the economics of fabrication and design. Consequently, noninvasive, noncontact techniques are needed to measure the geometric and material property data over the full device.

For materials characterization, scaling laws require a measurement resolution of 0.1 – 1 nm in MEMS structures. Interferometric techniques are needed to achieve this accuracy over a full field of view. The invention of phase-shifting interferometry (PSI) was a major breakthrough in the field of homodyne interferometry, providing a method to measure the optical phase with unprecedented accuracy [Creath, 1992]. Implemented on almost all types of interferometric imaging systems, through use of various algorithms, PSI allows extraction of a phase map from several intensity fringe patterns. Classic phase-shifting interferometry requires integration of 3 or more intensity maps during a linear variation in the optical phase over a 2π phase variation [Creath, 1988; Kreis, 2005]. Later, phase stepping interferometry was developed where the intensity integration occurs at discreet phase steps. These techniques provide an RMS accuracy of $\lambda/100$ in a

well-calibrated system [Creath, 1988]. As the acquisition speed increases, the phase error level increases due to increasing phase-shift miscalibration error. At high frequency, the reference excitation waveform becomes distorted due to jerk and other inertial effects on the reference mirror. Increasing the number of recorded interferograms reduces the degradation in the recovered phase-shift error at the expense of increasing processing time [de Groot, 1995a].

This Thesis implements phase modulating interferometry (PMI) as an alternative technique to minimize the impact of rapid acquisition speeds on the recovered phase map while providing measurement resolution on the order of 1 nm or better. When initially proposed by Sasaki and Okazaki [1986a], phase modulating interferometry combined 4 bucket integration with a sinusoidal reference excitation providing continuous reference motion with a waveform that will remain undistorted at high excitation frequencies. A variant of this initial work has been developed that operated in quadrature under stroboscopic illumination. These variations allow for both the rapid acquisition of interferograms and the use of stop-illumination techniques for the capture of rapid motions, vital in dynamic and in-situ measurements of MEMS devices.

Unlike commonly used PSI methods, PMI requires reference excitation amplitude of less than the illumination wavelength. However, this excitation amplitude is a strongly non-linear function of the stroboscopic illumination duty cycle. Additionally, both the quadrature and integrating bucket methods require a known phase difference between the illumination/acquisition period and the reference excitation period [Dubois, 2001; Sasaki, and Okazaki, 1986a]. Additive noise concerns of the PMI system are presented in this Thesis and used in the determination of the reference excitation amplitude and phase.

Error in the recovered phase map is then proportional to the error in these two parameters.

The phase modulating system, reported in this Thesis, was implemented in a Linnik configuration and is controlled with software designed in the LabVIEW™ graphical programming environment [LabVIEW™ 7.1, 2006]. The implementation required synchronization of the illumination source with the reference excitation and camera acquisition time. Representative Results are presented showing feasibility of the developed PMI technique for high resolution measurements of shape and semi-static loading situations of MEMS.

2. BACKGROUND

MEMS, or microelectromechanical systems, is an approach to fabrication that uses the materials and processes of microelectronics fabrication to convey the advantages of miniaturization, multiple components and microelectronics to the design and construction of integrated microstructures and electromechanical systems [Hsu, 2002; MEMS Industry Group, 2006]. In development since the late 1960s, MEMS has evolved from the integrated circuit industry as an effort to radically miniaturize operation scale over traditional mesoscale devices while increasing performance and reducing product cost [Judy, 2001]. As an enabling technology, MEMS revolutionized many industries by allowing development of smart products, augmenting the computational ability of microelectronics with the perception and control capabilities of microsensors and microactuators and expanding the space of possible designs and applications [MEMS Exchange, 2006].

According to MEMS Industry Group, MEMS and MEMS related applications have rapidly grown 15% to 20% per year over the last decade into an estimated $8.3 billion dollar industry in 2007, as shown in Fig. 2.1, with one-third of that revenue in pressure and inertial sensors, as presented in Fig. 2.2 [MEMS Industry Group, 2006].

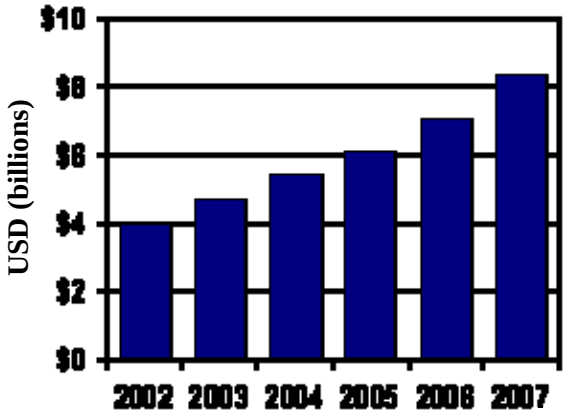

Fig. 2.1. Worldwide revenue forecast for MEMS [MEMS Industry Group, 2006].

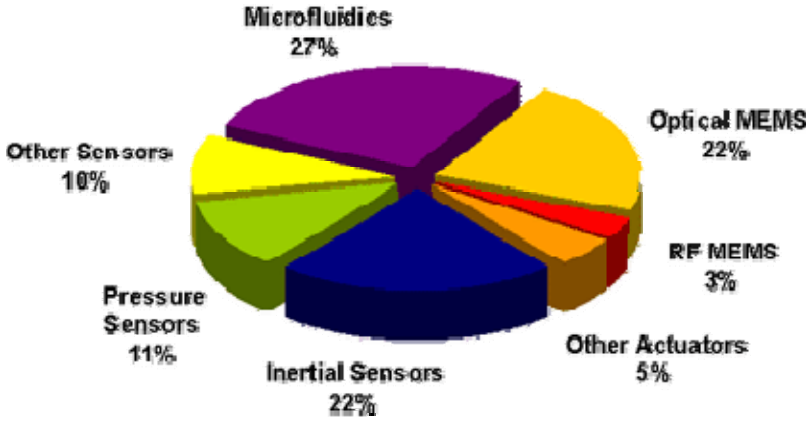

Fig. 2.2. Share of MEMS revenues by device, 2007 [MEMS Industry Group, 2006].

From Figs 2.1 and 2.2, it is apparent that MEMS devices are found ubiquitously throughout the modern world. Applications stemming from the groups presented in Fig. 2.2 include inertial navigation systems, integrated optomechanical components for image display, embedded sensors and actuators for condition maintenance, shown in Table 2.1, and much more [Furlong, 2004a].

Table 2.1. Microsensor families.

Position	Pressure	Inertial	Magnetometers
Thermal	Chemical	Radio frequency	Electrochemical
Field effect transistors	Biosensors	Molecular-specific	Cell-based
Neural systems	Gas	Fluid Flow	

Much of this industry growth is focused on the development of micro-sensors with higher spatial resolutions and temporal bandwidth than their macroscale counterparts while requiring less operating power [Judy, 2001]. Typically, it can take 10^{+} yrs and millions of dollars to develop a new sensor or a MEMS platform.

Over the years, most of the development money has been spent on pressure sensors and accelerometers and, as such, these two areas are the furthest developed MEMS technology [Electronic Design, 2000; MEMS Industry Group, 2006]. However, little standardization exists within industry in all but the simplest designs though organizations, such as the American Society of Mechanical Engineers and the Institute of Electrical and Electronics Engineers, have begun developing standards for adoption as industry norms. With increasing commercialization, there has been a greater push towards the acceptance of these standards particularly in MEMS testing and packaging procedures.

Testing issues must be included in the overall design of the device/package in the early phase of development to minimize the final cost of the device. Modern testing can be as much as 33% of the overall development cost of a MEMS device [MEMS

Exchange, 2006]. Testing can and must occur at multiple stages of MEMS development as illustrated in Fig. 2.3. This figure presents a typical MEMS development cycle with testing requirements at each stage of the design process. These tests include materials characterization during fabrication and accelerated lifecycle testing to ensure the longevity of the developed components.

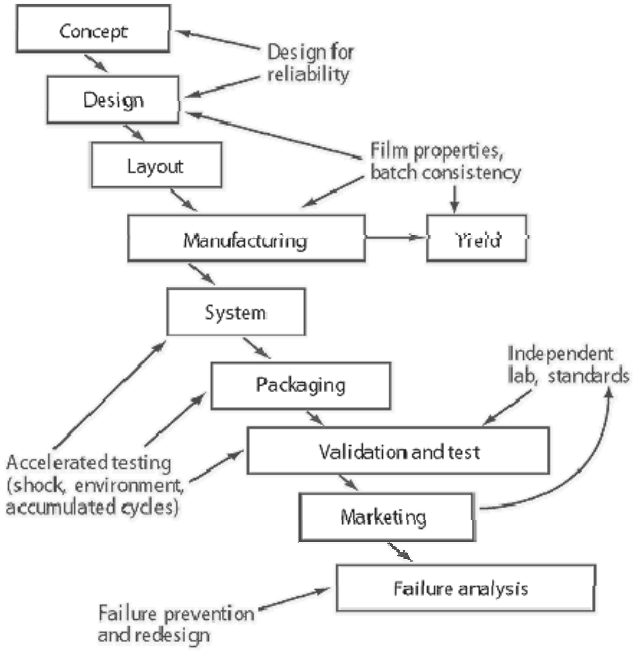

Fig. 2.3. MEMS development cycle [Exponent, Inc., 2000].

A major concern within these testing procedures is the unknown reliability of many MEMS devices due to uncertainty in the long-term stability of these devices. As a consequence of scaling in micro-components and fabrication variability, bulk, continuum material property data are not applicable to MEMS devices where crystalline structure and thermo-mechanical fabrication effects are dominant factors. Only greater knowledge of the basic material properties and failure mechanisms of the materials employed in

MEMS designs will allow for a wider acceptance of these systems [MEMS Industry Group, 2006].

2.1. MEMS material property variation

MEMS fabrication falls into three main families: surface micromachining, bulk micromachining, and lithographic techniques [Hsu, 2002]. Surface micromachining is based on the deposition and etching of different structural layers. Starting with a silicon wafer or other substrate, layers are grown and selectively etched by a wet or dry etch involving an acid or ionized gas respectively. While surface micromachined components may someday grow to as many layers as is needed, modern MEMS devices use up to five structural layers [Pryputniewicz, 2005; Sandia, 2006].

Bulk micromachining defines structures by selectively etching inside a substrate creating structures within a substrate. Like surface micromachining, bulk micromachining can be performed with wet or dry etches. As this process involves the selective removal of material, the particular etchant used is strongly dependant on the fabrication speed and quality requirements. Wet isotropic etching provides the same etch rate in all directions while undercutting masking material. Wet anisotropic etch rate depends on the crystalline plane orientation within the substrate material. Consequently, the lateral etch rate can be much larger or smaller than the vertical etch rate and resulting structures have angled walls, with the angle being a function of the crystal orientation of the substrate. Dry etching involves the removal of material by gaseous etchants though requires the periodic deposition of an etching protective material to minimize the side

wall angle in an etched cavity [Rai-Choudhury, 2000; Hsu, 2002; Krauss, 2002; Furlong, 2004a].

Lithographic techniques include the LIGA molding process. LIGA, a German process, is an acronym for X-ray lithography (**Li**thographie), electroplating (**G**alvanoformung), and molding (**A**bformung). Developed in the 1980s, LIGA was one of the first major techniques to allow for manufacturing of high-aspect-ratio structures with lateral dimensions below one micron and thicknesses up to 500μm [Hsu, 2002; Furlong, 2004a]. This technique allows for the creation of 3-D microstructures defined by 2-D lithographic patterns. The height-to-width ratio capability is relevant to the manufacturing of miniature components that can withstand high pressure and temperature, and can transfer useful forces or torques [Sandia, 2006].

Variation in the structure and material properties of MEMS devices exists between fabrication sites and within fabrication batches. Consequently, the material properties of a common MEMS material deposited by one manufacturer can vary substantially from that deposited by another. Further variation is present between and within wafer batches during production runs [Exponent Inc., 2000]. As seen in Fig. 2.4, a silicon nitride film applied across a single crystal silicon wafer may exhibit a nonlinear spatial variation in residual stresses on the order of 20 MPa. This variation illustrates the need for full field of view testing for accurate characterization of the fabricated structures.

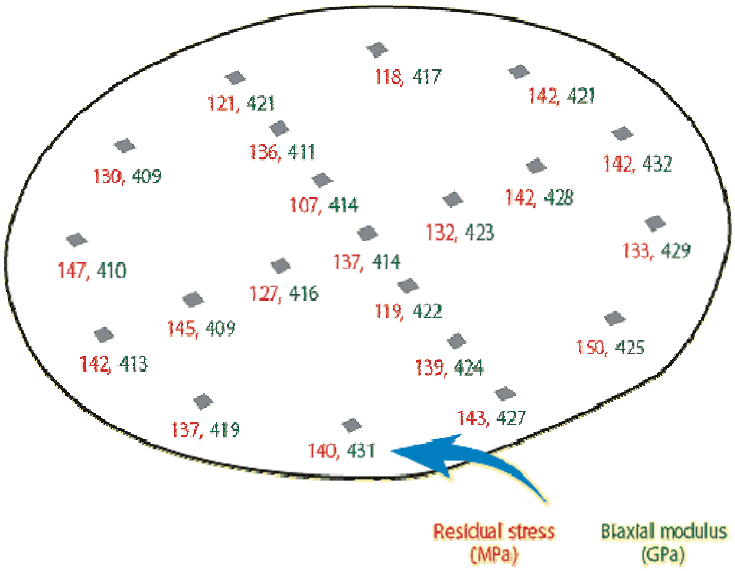

Fig. 2.4. Variation in residual stress and biaxial modulus across a silicon wafer [Exponent, Inc., 2000].

Much of this material property and fabrication property variation is due to the particular application of many materials used in MEMS structures. Silicon and other materials had been commonly used in the integrated circuit industry for decades. However, their application as thin film structures results in numerous mechanical properties which must be known for each material where traditionally only electrical characterization was required [Judy, 2001]. As with meso- and macroscale structures, critical mechanical properties include elastic modules, yield strength, fracture toughness, fatigue resistance, corrosion resistance, creep behavior, and residual stress.

Similarly, the novel capabilities of MEMS devices allow for operation under conditions unknown in the macro world. Micromirrors found on the DigitalMicromirror Device from Texas Instruments, Inc. commonly operate in excess of 1 trillion of cycles without failure [Douglass, 1998]. However, this total number of accumulated actuation cycles extends far beyond what has been required in "macro" applications. As with

macroscale devices, microscale devices can experience fatigue and wear from contacting surfaces during individual actuation cycles. However, little information about fatigue or wear is available under these conditions for either macro- or MEMS devices. As a result, lifetime predictions are device specific and, due to fabrication variations, are not always largely validated by statistics [Rai-Choudhury, 2000].

2.2. Nondestructive evaluation of MEMS

Nondestructive evaluation (NDE) is used to "evaluate prototype designs during product development, to provide feedback for process control during manufacturing, and to inspect the final product prior to service" without affecting the object's future usefulness [Shull, 2002]. The basic principle of NDE is finding and measuring physical phenomena that will interact with and be influenced by the test specimen without altering functionality. Functionally, choosing the proper NDE method from all available techniques requires considering of the following factors:

1) understanding the physical property to be inspected.
2) understanding the physical properties of the NDE methods.
3) understanding the interaction between the method and the test sample.
4) understanding the potential and limitations of the technology.
5) understanding of surrounding economic, environmental, and other factors.

Before using any NDE method, there must be some knowledge of the properties of interest. In MEMS, an investigator may be interested in the modulus of elasticity of an object of interest. This requires information on how modulus of elasticity may be calculated or how it may affect the system of interest, whether through dynamic or static effects. This knowledge works to drive NDE method choice. If the structure of interest is a laminated plate with homogenous and isotropic material properties, modulus of elasticity may be determined through investigation of the stress-strain relationships within that structure, assuming an application of general plate theory, the Kirchhoff hypothesis, and planar stress. These assumptions allow for calculation of the modulus of elasticity, bulk modulus, and Poisson's ratio within that object, assuming knowledge of the applied stresses and resultant strains [Boresi and Sidebottom, 1985; Guckel, et al., 1985]. Many NDE methods may be used to extract the stress and/or strain information needed for these calculations.

Larger samples may use an ultrasonic technique for determination of these elastic constants by investigating wave propagation through the sample, though typically this requires contact by a transducer/receiver. In a small system, this contact may have a significant influence on the recovered data. An X-ray system may be used in 2-D or 3-D as a way to measure the shape and hence deformations of the object of interest. The major disadvantages to this technique are the high cost, danger, and potential for imaging artifacts to make analysis difficult. Positively, X-ray computed tomography has been applied to objects from 5 μm to 2 m which is on the scale of MEMS devices [Haddad, et al., 1994; Tonner and Stanley, 2002]. Similarly, various optical techniques exist which allow for shape measurements of the system of interest. As with X-ray computed

tomography, this shape information is then used to determine the deformations of the system of interest and hence the strains resulting from an applied stress. However, unlike X-ray methods, optical techniques have demonstrated subnanometer shape measurement resolution.

2.3. Interferometric options

Interferometry uses changes in an optical wavefront to measure how an object behaves under loading. Where many techniques exist to record these changes, each have different strengths and weaknesses when used in a NDE application. Modern techniques include, and are not limited to, the following categories: homodyne interferometry, spatial and temporal heterodyne interferometry, digital holographic interferometry, and white light interferometry [Dyson, 1970; Sirohi and Kothiyal, 1991; Greivenkamp and Bruning, 1992; Wyant, 2002; Kreis, 2005]. Homodyne systems consider the relative optical phase-shift between coherent reference and object beams. In a multiple path interferometer, the relative phase between the two beams is directly proportional to the wave number, k, and the shape of the object of interest, Z. A Michelson-type interferometer, presented in Fig. 2.5., recovers shape proportional to twice the optical path length difference, D.

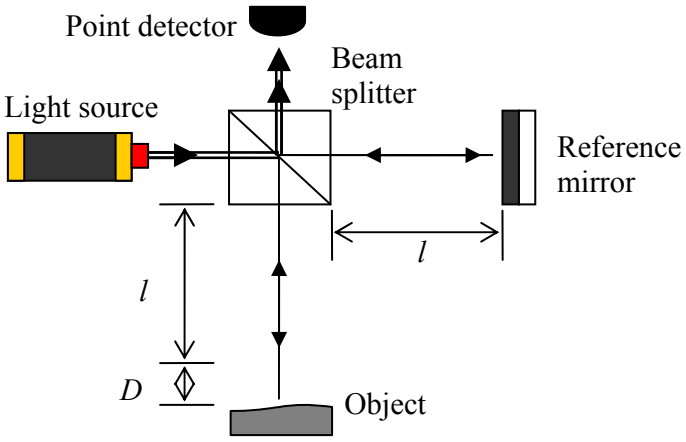

Fig. 2.5. Michelson interferometer [Kreis, 2005].

The object shape can then be recovered as

$$Z = \frac{\Delta\phi}{2 \cdot k} = \frac{\Delta\phi}{\frac{4\pi}{\lambda}} = \frac{\Delta\phi \cdot \lambda}{4\pi} \quad , \tag{2.1}$$

where λ is the illumination wavelength, $\Delta\phi$ is the recovered optical phase, and k is the wave number along the optical path [Kreis, 2005]. Typical methods for extraction of the optical phase from acquired interferograms include phase stepping or phase-shifting of the reference beam path length. The optical phase map magnitude and directionality can then be solved for by acquisition of three or more interferograms with relative phase differences [Kreis, 2005].

Phase stepping interferometry can be separated into temporal and spatial methods. In this Thesis, all comparisons are made with regards to temporal phase-shifting which requires that the phase be stepped with time, usually in a uniform manner within the whole field by using a modulator device [Creath, 1988; Greivenkamp and Bruning, 1992]. During this process, a series of interferograms with a certain phase increment between them is obtained. Once these phase-shifted patterns have been combined using a

phase-shifting algorithm, we can obtain the phase values modulo 2π for all of the full field of view points simultaneously. This method can provide as accuracy level of up to $\lambda/1000$ if the ambient conditions and experimental setup are well controlled [Creath, 1988, 1992; Haasteren and Frankena, 1994; Dorrio and Fernandez, 1998]. However, due to the need to obtain different separate patterns in time, temporal phase stepping methods cannot be applied to dynamic processes without the application of a stroboscopic illumination source or implementation of an acquisition system that is rapid relative to the dynamic processes being studied as standard methods assume that the background intensity, contrast, and phase be stationary over the interferogram acquisition period [Creath, 1988; Kreis, 2005]. The number of interferograms acquired depends on the particular phase extraction algorithm employed where larger numbers are used to reduce sensitivity to systematic noise and environmental effects [Surrel, 1993; de Groot and Deck, 1996; Ruiz, et al., 2001].

Historically, temporal phase-shifting algorithms were restricted to combinations of three or four interferograms where modern algorithms have been demonstrated with linear combinations of up to seven interferograms [Hariharan, et al., 1987; de Groot, 1995a; Surrel, 1996]. Using windowing to increase the insensitivity to variations in phase steps has become a common practice with the acquisition of seven or more interferograms as the larger the data set, the more accurately it can be windowed [de Groot, 1995a; Schmit and Creath, 1996; Ruiz, et al., 2001].

In terms of performance, the four bucket PSI algorithm has been shown to be a significant improvement over the three-bucket algorithm with regards to vibration sensitivity, at the cost of slightly larger memory requirements and slightly longer

processing time [Surrel, 1993; de Groot, 1995a; Ruiz, et al., 2001]. A five bucket algorithm analyzed by Hariharan, et al. [1987] has been shown to be minimally sensitive to small phase step errors at the expense of increased processing time and memory requirements. While increases in the number of acquired data samples correlates with a decrease in sensitivity to phase step errors, the number of data samples is typically limited by processing speed, computer memory limitations, and "the limited phase-shift range of piezoelectric transducer actuators" [Surrel, 1993; Deck, 2003].

Spatial phase-shifting interferometry differs from temporal phase-shifting interferometry by simultaneously acquiring a set of phase-shifted interferograms while preserving the measurement accuracies of temporal phase-shifting. These interferograms are either captured on multiple imaging devices or on a singular array that is later subdivided numerically [Koliopoulos, 1992; Dorrio and Fernandez, 1998; 4D Technology, Inc., 2006]. A spatial separation of the interferograms can be achieved with rotational polarizing components, diffraction gratings, or computer generated diffractive optical elements [Dorrio and Fernandez, 1998; North-Morris, et al., 2002; 4D Technology, Inc., 2006]. In this method, errors due to environmental instabilities are avoided with the simultaneous acquisition of the patterns. However, other types of errors appear due to variations in the different camera systems used or within different parts of the same imaging array [Koliopoulos, 1992]. Consequently, additional data processing is needed to match the measurement accuracy of temporal phase stepping therefore real-time evaluation methods are obtained at the cost of measurement accuracy [Kwon, et al, 1987].

By contrast, temporal heterodyning uses the interference of two optical waves of different frequencies which produces an intensity oscillating at a beat frequency equal to the frequency difference [Sirohi and Kothiyal, 1991]. These systems split the reference and object beams by use of an acousto-optic modulator. A Zeman splitter may be used to separate the beam within the laser head, through use of powerful magnets [Chapman, 2002]. Another technique involves the use of a dual mode laser with beat frequency of 1 GHz or above. Alternatively, acousto-optic modulators can be used to shift the beam path between multiple output angles creating a misalignment between the object and reference beams. However, this approach increases the level of physical complexity within the interferometric system while introducing a secondary frequency shift into the reference beam requiring an additional photo-detector to determine the shifted beat signal after modulation. Regardless of how the beat frequency is created, these systems measure the returned optical phase by timing the arrival of zero crossings on the sinusoidal illumination signal [Chapman, 2002].

Spatial heterodyning relies on the addition of a carrier frequency on the interference pattern. This technique, alternatively known as a Fourier-transform method, was proposed as an alternative to traditional homodyne and heterodyne techniques [Takeda, et al., 1982]. A spatial carrier frequency may be generated interferometrically though the addition of a tilt to the reference mirror in a homodyne system or through the use of a holographic grating. Modern applications include projection of a computer generated fringe pattern allowing for the determination of optical phase through a single interferogram while solving for the sign ambiguity problem. This technique relies on the projection or creation of a carrier fringe pattern higher than the spatial variations present

within the recovered optical phase. This condition limits the measurement resolution of a spatial heterodyne system to the ability of the holographic system to both project and recover the carrier frequency signal without aliasing [Kreis, 2005]. However, measurement accuracy of both spatial and temporal heterodyne interferometry has been found to be on the same order as temporal phase stepping interferometry though typically requiring greater experimental complexity and processing time [Dorrio and Fernandez, 1998].

Digital holography uses a digital imaging system to record holograms for later numerical reconstruction [Kreis, 2005]. The angle between the object and reference wavefronts must be controlled to produce holograms which are resolvable by a given imaging system. Recovery of the object surface requires the numerical reconstruction of the wavefront at the image plane by use of the Fresnel transform [Kreis, 2005]. The image plane or observation plane appears at the coordinates where the real image can be reconstructed. At this plane, the wavefront reflected from the object of interest converges to a sharp image. Shape information can then be extracted from the calculated object wave field. Phase-shifting digital holography, involving the capture of three or more digital holograms with a mutual shift in the reference wave, can be used for shape characterization of MEMS [Furlong and Pryputniewicz, 2003]. The primary advantage to the phase-shifting approach is the elimination of the DC-component and twin image within the reconstructed wave field though at the expense of an increased system stability requirement [Kreis, 2005]. If these stability requirements are met, digital holographic methods have been shown to be $\lambda/100$ accurate [Dorrio and Fernandez, 1998; Mann, et. al, 2005].

White-light interferometric techniques rely on the application of a short coherence length white light source instead of the more commonly used laser light sources as demonstrated in Fig. 2.6 [Wyant, 2002; Kreis, 2005]. Traditionally, laser light has been used as its long coherence length simplifies the procedures required for the creation of interference fringes as the interferometer path lengths no longer have to be matched as closely as if a short coherence length white light source is used. However, laser light interference fringes can appear within any stray reflections, possibly resulting in incorrect measurements. The strict optical path length matching requirements of short coherence white light systems eliminates this concern while providing a powerful measurement tool [Wyant, 2002]. While homodyne phase-shifting interferometry has proven extremely powerful and useful in many research and commercial systems, possessing a measurement resolution of $\lambda/100$, the height difference between two adjacent data points must be less than $\lambda/4$, where λ is the wavelength of the light source [Creath, 1988; Wyant, 2002]. If the slope is greater than $\lambda/4$ per detector pixel then height ambiguities of multiples of half-wavelengths exist. However, the use of white light makes it possible to connect fringe orders across this step at similar measurement resolutions.

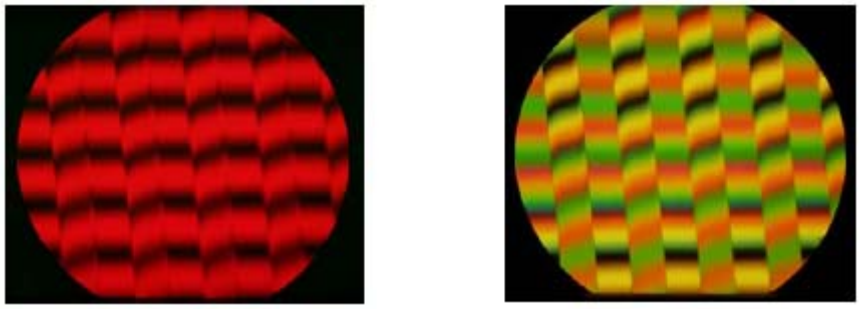

Fig. 2.6. Monochromatic, red light, versus white light interferograms of a sample with $>\lambda/4$ step discontinuities demonstrating the ability to connect fringe orders using white light interferometry [Wyant, 2002].

Coherence probe interferometers are used to obtain height measurements on structures exhibiting large steps or rough surfaces. With a short coherence length source, good contrast fringes will appear only when the two interferometric paths are closely matched. Consequently, if the path length of either the object or reference arms is adjusted, the maximum fringe contrast will translate along the instrument sensitivity vector. The height variations across the sample can then be determined by looking at the locations at which the fringe contrast is maximized. As the translation of the fringe contrast is controlled there are no sign ambiguities in the recovered height map. Additionally, as the maximum fringe contrast is obtained when the sample is in focus, there will be no focus errors during surface measurement [Caber, 1993; Wyant, 2002].

The major drawback of measurements with this type of scanning interferometer is that only a single surface height is being measured at a time. As a result, transient event may be overlooked or misinterpreted. Additionally, a large number of measurements and calculations are required to accurately determine surface height values, where typical sampling intervals can range from 50 to 100 nm. [Caber, 1993; de Groot, et al., 2002]. "To obtain the location of the peak fringe contrast, and hence the surface height information, this irradiance signal is detected using an [imaging] array. The signal is sampled at fixed intervals […] as the sample path is varied. [The signal is then digitally filtered and rectified by square-law detection.] The peak of the filter output is located and the vertical position corresponding to the peak is noted. Interpolation between sample points can be used to increase the resolution of the instrument beyond the sampling interval. This type of measurement system produces fast, non-contact, true three-dimensional area measurements for both large steps and rough surfaces to

nanometer precision. [Wyant, 2002]." With this processing 0.1 nm accuracy levels have been demonstrated [Zygo Corporation, 2006].

2.4. Benefits of phase modulating interferometry

While the invention of phase-shifting interferometry (PSI) was a major breakthrough in the field of interferometry by providing a method to measure the optical phase to an unprecedented accuracy, this Thesis proposes phase modulating interferometry (PMI) for the nondestructive evaluation of MEMS devices [Creath, 1988; Schwider, 1990]. Originally proposed in Sasaki and Okazaki [1986a, 1986b] and expanded in Dubois [2001], this method answers some of the limitations inherent in classic homodyne and heterodyne techniques while combining strengths of each. By continuously modulating an illumination wave front and using a four bucket algorithm, shown in Fig. 2.8, it has been demonstrated that a time-varying interference pattern can be detected and analyzed to a measurement accuracy of 1.0 nm under a 600 nm illumination source. This is possible because the amplitude and phase of the modulation signal is chosen to minimize the effects of Gaussian additive noise on the recovered optical phase map. As shown in Table 2.2 and discussed in Sasaki and Okazaki [1986a], Sasaki, et al. [1990a, 1990b], Dubois [2001], and Dorrio and Fernandez [1998], sinusoidal phase modulating interferometry has demonstrated an accuracy level of 0.1 nm which is on par with that obtained with temporal phase modulating interferometry though at the cost of higher processing complexity. This increased complexity is offset by an increased immunity to static and dynamic environmental and systematic noise effects

below the modulation frequency versus both temporal and spatial phase stepping interferometry [Sasaki and Okazaki, 1986a, 1986b; Creath, 1988; Suzuki, et al., 1994; de Groot and Deck, 1996; Dorrio and Fernandez, 1998; Dubois, 2001; Kreis, 2005].

Table 2.2. Comparison of phase evaluation methods without a spatial carrier [Sasaki and Okazaki, 1986a; Suzuki, et al., 1994; Dorrio and Fernandez, 1998; Dubois, 2001, Kreis, 2005].

	Method			
	Temporal phase stepping methods	Spatial phase stepping methods	Heterodyne interferometric methods	Sinusoidal phase modulating interferometry
Required interferograms	≥ 3	≥ 3	continuous detection	≥ 4
Accuracy	very high	high	very high	very high
Influence of static noise	low	high	low	low
Influence of dynamic noise	high	low	high	low
Experimental requisites	high	low	very high	very high

In Sasaki and Okazaki [1986a, 1986b] and Dubois [2001], the developed interferometric systems operate under sinusoidal modulation in four integrating bucket mode, as shown in Fig. 2.7.

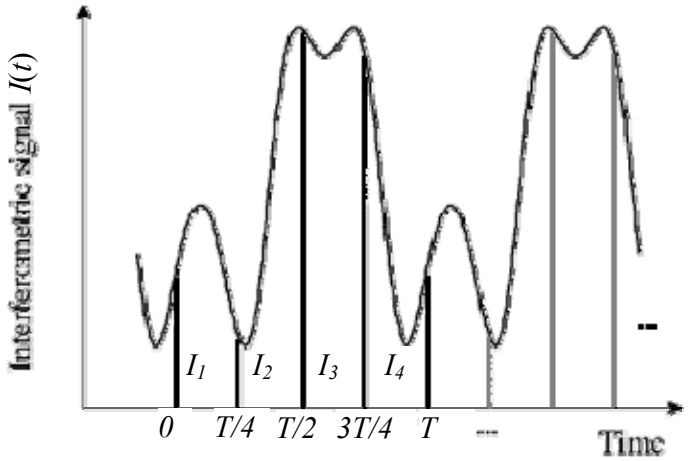

Fig. 2.7. Simulation of the interferometric signal $I(t)$ and how it is integrated over the four quarters of the modulation period [Dubois, 2001].

According to Fig. 2.7, this integration is performed by a two-dimensional detector array with a charge storage period equal to one-quarter of the period of the sinusoidal phase modulation, $T/4$. Interferograms are then acquired over sequential quarters to generate a set of four interferograms for data processing. This combination of sequential acquisition periods each over one part of the modulation cycle is known as an integrating bucket method. Sinusoidal modulation was chosen to minimize errors within the recovered optical phase map by minimizing the jerk experienced by translation of a reference mirror. PSI techniques involve 3 or more stepped motions of a reference mirror to solve the underlying interferometric equations. Each stepped motion involves the rapid acceleration and deceleration of the attached reference mirror. Increasing acquisition speed results in greater operational jerk creating nonlinearities in the reference modulation. A 10% modulation miscalibration error correlates with an error in the recovered optical phase map of 0.20 radians in a 4-frame algorithm or ~20nm under a 620nm illumination source [Creath, 1992; Surrel, 1993]. An increase in the number of acquired interferograms will reduce the phase error to 0.0796 radians at the expense of

increased processing requirements [Surrel, 1993]. The sinusoidal modulation of the PMI system minimizes the jerk of the reference arm demonstrating a theoretical phase measurement accuracy of less than 0.5 - 0.8 nm under a 600 nm illumination source [Sasaki and Okazaki, 1986b]. Experimentally, these errors have been found to be from 0.5 – 1.0 nm when operating under a 200 Hz modulation signal [Sasaki and Okazaki, 1986a, 1990a; Dubois, 1999, 2001].

While the previously presented four-bucket method has been proven for the analysis of static structures, the currently defined system has not been demonstrated with dynamic studies. Due to the relatively long acquisition period, the observable intensity field becomes modulated by the square of the zero order Bessel functions of the first kind, $J_0(Y)$. In harmonic vibration studies, the fringes become contours of equal vibration amplitudes at the spatial vibration nodes. Additionally, fringe contrast decreases with increasing fringe order with the maximal contrast existing at the nodes of the vibration mode [Kreis, 2005]. Application of a stroboscopic illumination signal converts the J_0 fringes into a sinusoidally modulated fringe pattern, greatly simplifying extraction of the optical phase map due to the complexity of the Bessel function term.

The focus of this work is the derivation and implementation of the phase modulating interferometric system that uses both stroboscopic illumination and a reduced exposure period. The addition of these physical attributes will allow for use of the PMI system in both dynamic and static studies.

3. THEORETICAL ANALYSIS OF PHASE MODULATING INTERFEROMETRY

Sasaki and Okazaki [1986a] and Dubois [2001] have presented the derivation of a phase modulating system using the 4 integrating bucket method and a sinusoidal reference excitation. This approach assumes a constant illumination source and requires multiple excitation periods to fully capture the modulation waveform. The latter limitation is based on the recording media used due to the finite time required between interferogram acquisition periods. This prevents the continuous capture of a single reference excitation waveform, particularly at the rapid reference excitation frequencies required for rapid display of the wrapped phase map.

Additionally, this approach is limited with regards to dynamic systems as it requires an exposure time which may be long compared to the period of excitation. This situation is known as time average holographic interferometry. In this case, the intensity of the recovered fringes is modulated by the zero order Bessel function of the first kind.

Stroboscopic illumination allows for an acquisition time which is on the order of the dynamic system motion. As the illumination period becomes short relative to the motion of the system of interest, the recovered interferogram is the same as that recovered with double-exposure holographic interferometry and so is only modulated by a cosinusoidal term. This results in the ideal case for optical phase recovery [Kreis, 2005].

To allow for the capture of both dynamic and static systems, the effect of stroboscopic illumination on phase modulating interferometry is presented with a focus on a sinusoidal reference excitation.

3.1. General derivation of phase modulating interferometry with stroboscopic illumination

The intensity distribution of a holographic interferogram as recovered by an imaging system is a function of the unmodulated DC component of an illumination intensity, $I_B(x,y)$, the interference fringe contrast, $V(x,y)$, and the interference phase distribution, $\phi(x,y)$. At one instant of time, the full-field intensity is of the form

$$I(x,y) = I_B(x,y) \cdot \{1 + V(x,y) \cdot \cos[\phi(x,y)]\} \quad , \tag{3.1}$$

or

$$I(x,y) = I_B(x,y) + I_M(x,y) \cdot \cos[\phi(x,y)] \quad , \tag{3.2}$$

where $I_M(x,y)$ describes the modulated amplitude of interference fringes [Kreis, 2005]. Extraction of the phase distribution requires the solution of a system of equations due to the multiple unknowns in the general equation. This system must also be posed in a way that eliminates the phase ambiguity present in the above equations with respect to the phase distribution due to the even, periodic nature of the cosine function. Traditional phase-shifting and phase stepping methods provide a means for extraction of the optical phase and solution of the sign ambiguity. This is accomplished through the acquisition of multiple intensity distributions with mutual phase-shifts. Nonlinear equations, of the form shown in Eq. 3.3, can then be solved for the optical phase over the full field of view. When the reference phase-shift, $\phi_R(x,y)$, between each interferogram, is known a minimum of three intensity distributions must be found to solve for $I_B(x,y)$, $I_M(x,y)$, and $\phi(x,y)$ [Kreis, 2005],

$$I(x,y) = I_B(x,y) + I_M(x,y) \cdot \cos[\phi(x,y) + \phi_R(x,y)] \quad . \tag{3.3}$$

While phase stepping or shifting rely, respectively, on discreet step or saw tooth variation in the optical phase to provide the known phase term within recovered interferograms, phase modulating interferometry uses a known continuously varying phase variation [Sasaki and Okazaki, 1986a; Kreis, 2005]. In this Thesis, the continuously variant signal is accomplished with motions of a piezoelectric actuator attached to the reference mirror. Phase modulation is differentiated from phase-shifting by eliminating the linear phase variation requirement, allowing for the application of a continuous phase modulation function. With this implementation, the overshoot and settling experienced by piezoelectric actuators during discontinuous motion can be reduced or eliminated.

As shown in documentation from Physik Instrumente, L.P. [2005], piezoelectric actuators undergoing discontinuous motions experience an instantaneous displacement overshoot of 10 -15 % under low displacement steps. The actuator then requires a finite settling time to attain its nominal displacement. As shown in Eq. 3.4, the minimum settling time is related to the natural frequency of the actuator and attached components. When operating below 10% of the resonant frequency, the minimum settling time is given by [Physik Instrumente, L.P., 2005]

$$t_{\min} = \frac{1}{3f_0'} \quad . \tag{3.4}$$

The additional mass of the reference mirror and surrounding structure alters the natural frequency of the unloaded actuator, f_0. While the resonant frequency of the unloaded actuator is normally given by a manufacturer, the loaded natural frequency, f_0', can be found by

$$f_0' = f_0 \sqrt{\frac{m_{eff}}{M + m_{eff}}} \quad , \tag{3.5}$$

where M is the additional mass coupled to the piezoelectric actuator and m_{eff} is the effective mass of a piezoelectric actuator equal to 1/3 the mass of the ceramic stack [Physik Instrumente, L.P., 2005]. For a piezoelectric actuator with a resonant frequency of 2 kHz and negligible loaded masses, the minimum settling time will be approximately 0.5 ms. This settling time will be greatly increased at modulation frequencies approaching the effective natural frequency and with the attachment of masses to the piezoelectric stack.

The significant overshoot coupled with the settling time may result in an average modulation error of 5 - 10% during phase stepping [Surrel, 1993]. As phase stepping relies on constant phase steps, this modulation error will correspond to a mean error in the recovered optical phase map described by Eq. 3.6 [Surrel, 1993],

$$\langle \varepsilon \rangle = \frac{1}{2N \sin\left(\frac{2\pi}{N}\right)} \frac{\Delta\psi_{actual}}{\Delta\psi_{ideal}} \cdot 2\pi \quad . \tag{3.6}$$

From Eq. 3.6, it is apparent that the mean optical phase map error decreases with larger N-bucket algorithms and increases with larger modulation errors. For the case of a 5% modulation error, the mean phase error becomes 39.25 mrad for N = 4.

As shown, this modulation error may be due to actuator overshoot and settling time, however, other factors including hysteresis and creep may contribute to an error in the modulation step [Physik Instrumente, L.P., 2005]. Hysteresis and creep describe positional errors during open-loop operation due to crystalline polarization effects and molecular effects within a piezoelectric material. "The amount of hysteresis increases

with increasing voltage applied to the actuator. The "gap" in the voltage/displacement curve of a piezoelectric actuator typically begins around 2% and widens to a maximum of 10% to 15% under large-signal conditions. If, for example, the drive voltage of a 50 μm piezoactuator is changed by 10%, the position repeatability is on the order of 1% of full travel or 1 μm [Physik Instrumente, L.P., 2005]." Creep is a change in displacement with time without corresponding changes in the voltage source due to changes in the remnant polarization changes within the piezoelectric material. For rapid to moderate acquisition systems, the effect of creep on the resulting phase map errors will be minimal as, in practice, creep is typically a few percent over an hour [Physik Instrumente, L.P., 2005]. Phase modulating interferometry minimizes both hysteresis and creep effects relative to phase stepping or phase-shifting due to the periodic and continuous motion of the piezoelectric actuator [Physik Instrumente, L.P., 2005].

To eliminate the effects of overshoot and settling time while minimizing hysteresis, a sinusoidal reference excitation signal is implemented within this Thesis to the piezoelectric actuator. This creates a time dependent instantaneous intensity equation which must be integrated over the acquisition time to determine the recovered interferogram intensity. Additionally, the application of the sinusoidal modulation signal minimized the jerk experienced by the reference mirror at high frequencies while maintaining a relatively simple form for integration.

3.2. Use of sinusoidal reference excitation

Use of a sinusoidal reference excitation creates a reference phase term of the form

$$\phi_R(t) = \psi \sin(\omega \cdot t + \theta) \quad , \tag{3.7}$$

where the spatial dependence terms are dropped for simplicity. The value of ψ is related to the amplitude of the sinusoidal phase modulation, z, by

$$\psi = \frac{4\pi}{\lambda} z \quad , \tag{3.8}$$

where λ the wavelength of illumination [Kreis, 2005]. The reference phase excitation is then also a function of the angular frequency of excitation, ω, and the relative phase between the excitation and illumination cycles, θ. Consequently, the sinusoidal reference excitation, Eq. 3.7, has units of radians and therefore can be incorporated into the continuous interferometric intensity distribution. With the addition of this excitation, the resultant intensity distribution is of the form

$$I(t) = I_B(t) + I_M(t) \cdot \cos[\phi + \psi \sin(\omega \cdot t + \theta)] \quad . \tag{3.9}$$

To determine the intensity recovered at the imaging system, the intensity equation must be integrated over the acquisition period. Both, the trigonometric identity shown as Eq. 3.10,

$$\cos(X - Y) = \cos(X)\cos(Y) + \sin(X)\sin(Y) \quad , \tag{3.10}$$

and the Bessel function identities [Abramowitz and Stegun, 1970] in Eq. 3.11,

$$\cos\left[X\sin(Y)\right] = J_0(X) + 2\sum_{k=1}^{\infty}\left[J_{2k}(X)\cos(2k\cdot Y)\right] \quad ,$$

and (3.11)

$$\sin\left[X\sin(Y)\right] = -2\sum_{k=0}^{\infty}\left\{J_{2k+1}(X)\sin\left[(2k+1)\cdot Y\right]\right\} \quad .$$

are needed to rewrite Eq. 3.9 into integrable form. The time variant intensity is now given by,

$$\begin{aligned} I(t) &= I_B(t) + I_M(t)\cos(\phi)J_0(\psi) \\ &+ 2I_M(t)\cos(\phi)\left(\sum_{k=1}^{\infty}\left\{J_{2k}(\psi)\cos\left[2k(\omega\cdot t+\theta)\right]\right\}\right) \\ &+ 2I_M(t)\sin(\phi)\left(\sum_{k=0}^{\infty}\left\{J_{2k+1}(\psi)\sin\left[(2k+1)(\omega\cdot t+\theta)\right]\right\}\right) \end{aligned} \quad . \tag{3.12}$$

As discussed previously, a four integrating bucket method was proposed to define the acquisition period for static structures [Sasaki and Okazaki, 1986a; Dubois, 2001]. This technique defines the charge storage period of the imaging sensor as one quarter of the reference excitation period. Four images are then recorded through integration of the time-varying signal during the four quarters of the modulation period, *T*, allowing for recovery of optical phase. As demonstrated in Dubois, 2001, this approach provides a mathematically complex result describing the recovered illumination intensity map.

During the study of static structures, the resultant phase map remains cosinusoidally modulated allowing for sub-fringe measurement resolution. However, in dynamic studies a long exposure time compared to the period of sample motion causes the acquired fringe pattern to become modulated by the zero order Bessel function of the first kind. These fringes will have relatively low contrast compared the cosinusoidally

modulated pattern as the dark centers of the fringes correspond to zeros of the Bessel function, J_0, while the intensity of the bright fringes degrades with distance from the nodal line in a vibrating structure. Physically, these changes in fringe contrast result from the motions of the system of interest. As with static structures, some regions will reflect more light towards the recording media during their motion. As a result, these regions will appear brightest. A nodal line, in a plate or other simple structure, does not move and so will be providing light during the full acquisition period. Other regions may appear as a nodal line if the physical system becomes more complex and/or the motions more uncertain. In the case of pure torsional vibration viewed along the length of a shaft, the surface line facing the imaging array will appear as if it was a nodal line due to the orthogonal motions of the structure.

To record cosinusoidally modulated fringes during dynamic measurements, a short exposure time relative to the frequency of motion is required. Stroboscopic illumination is commonly used in meeting this need. The interferogram can then be exposed over multiple periods of motion until the total required exposure has been reached. To accomplish this with phase modulating interferometry, the charge storage period of the imaging array is redefined as a short time span around a particular point in the reference excitation for each image. For added simplicity in the derivation, it is assumed that these points are in quadrature with respect to the reference excitation period. As a result the time-dependent intensity is then integrated by

$$I_p = \frac{1}{\Delta t} \cdot \int_{\frac{pT}{4}-\frac{\Delta t}{2}}^{\frac{pT}{4}+\frac{\Delta t}{2}} I(t)dt \quad , \tag{3.13}$$

where T is the reference modulation period, Δt is the acquisition, or exposure, time of the imaging array, and p defines the frame number, 1, 2, 3, or 4. This means that the illumination will occur at the quadrature points of the reference excitation signal. As shown in Fig. 3.1, there are four interferograms acquired during each modulation period during each stroboscopic illumination amplitude peak.

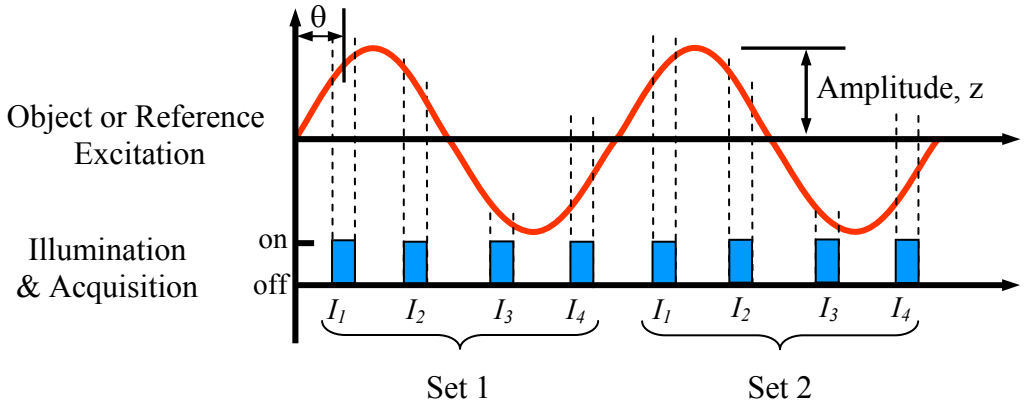

Fig. 3.1. Quadrature acquisition with stroboscopic illumination [Kuppers, et al., 2006].

Through appropriate integration, presented in Appendix A, based on Eq. A.8, the intensity recovered at the recording element becomes

$$
\begin{aligned}
I_p &= \bar{I}_B + \bar{I}_M \cos(\phi) J_0(\psi) \\
&+ \frac{2\bar{I}_M T}{\pi} \cos(\phi) \left\{ \sum_{m=1}^{\infty} \left[\begin{array}{l} (-1)^{m \cdot p} \, \frac{J_{2m}(\psi)}{2m} \cdot \\ \cos(2m\theta) \cdot \sin(m \cdot 2\pi d) \end{array} \right] \right\} \\
&+ \frac{2\bar{I}_M T}{\pi} \sin(\phi) \left(\sum_{m=0}^{\infty} \left\{ \begin{array}{l} \frac{J_{2m+1}(\psi)}{2m+1} \cdot \\ \sin\left[(2m+1) \left(\frac{p\pi}{2} + \theta \right) \right] \sin\left[(2m+1) \cdot 2\pi d \right] \end{array} \right\} \right)
\end{aligned}
\quad , \tag{3.14}
$$

for each acquired frame where the stroboscopic illumination duty cycle, d, is related to both the exposure time and the period of the reference excitation by

$$
d = \frac{\Delta t}{T} \quad , \tag{3.15}
$$

based on an integration procedure defined in Dubois [2001]. This form of the acquired intensity equation is independent of the reference excitation frequency or acquisition period which is advantageous during optimization of the reference excitation amplitude and phase, considered in the following Section.

Extraction of the optical phase requires the solution of a system of no less than 4 equations concerning 4 acquired interferograms. The optical phase of the object of interest can be calculated through a linear combination of 4 acquired frames given by

$$
\Sigma_s = \left(-I_1 + I_2 + I_3 - I_4 \right) \cdot \sin(\phi) \cdot K_c(\psi, \theta) \quad , \tag{3.16}
$$

and

$$
\Sigma_c = \left(-I_1 + I_2 - I_3 + I_4 \right) \cdot \cos(\phi) \cdot K_s(\psi, \theta) \quad , \tag{3.17}
$$

where $K_s(\psi, \theta)$ and $K_c(\psi, \theta)$ are the sine and cosine phase constants, respectively. These terms are solely functions of the reference mirror motion assuming at a constant illumination duty cycle. Mathematically, they are given as:

$$K_s(\psi,\theta) = \sum_{m=0}^{\infty}\left\{\frac{J_{2m+1}(\psi)}{2m+1}\cdot\sin\left[(2m+1)(\pi+\theta)\right]\cdot\sin\left[(2m+1)(\pi\cdot d)\right]\right\}+\ldots$$
$$\sum_{m=0}^{\infty}\left\{\frac{J_{2m+1}(\psi)}{2m+1}\cdot\sin\left[(2m+1)\left(\frac{\pi}{2}+\theta\right)\right]\cdot\sin\left[(2m+1)(\pi\cdot d)\right]\right\} \quad , \tag{3.18}$$

and

$$K_c(\psi,\theta) = \sum_{m=1}^{\infty}\left[(-1)^m\frac{J_{2m}(\psi)}{2m}\cdot\cos(2m\theta)\cdot\sin(2m\pi\cdot d)\right]+\ldots$$
$$\sum_{m=1}^{\infty}\left[\frac{J_{2m}(\psi)}{2m}\cdot\cos(2m\theta)\cdot\sin(2m\pi\cdot d)\right] \quad . \tag{3.19}$$

To remove the sign ambiguity, a ratio of Σ_s and Σ_c is used to extract the optical phase through the use of an arctangent calculation as

$$\tan(\phi) = \frac{K_s(\psi,\theta)}{K_c(\psi,\theta)}\frac{\Sigma_s}{\Sigma_c} \quad . \tag{3.20}$$

While Eq. 3.17 will provide the optical phase of an object for any known reference excitation amplitude and phase, these properties can be optimized to minimize the effects of additive noise on the recovered results, improving both accuracy and measurement repeatability.

Additive noise has the same power everywhere in the frequency domain. This arises, for example, from the fast dynamics along various degrees of freedom within a system, from the non-zero temperature of a system (thermal noise), or from electronic read-time bias [Gitterman, 1999]. This Thesis assumes a zero mean Gaussian noise distribution as confirmed experimentally [Luth, 1989]. The contribution of this noise on the acquired intensity distribution is given by a new term *n* and causes the instantaneous intensity term to take the form,

$$I(x,y) = I_B(x,y) + I_M(x,y) \cdot \cos[\phi(x,y) + \phi_R(x,y)] + n \quad . \tag{3.21}$$

Following the above derivation, the recovered optical phase will suffer an error, ε, and take the following form, as shown in Appendix B,

$$\tan(\phi + \varepsilon) = \frac{K_c}{K_s} \cdot \frac{\Sigma_s + N_s}{\Sigma_c + N_c} \quad , \tag{3.22}$$

where N_s and N_c (Eqs B.5 and B.6, Appendix B) represent the error contribution within each acquired interferogram, assuming a high signal to noise ratio. These error parameters are of the same form as the linear interferogram combinations, Σ_s and Σ_c. As demonstrated in Eqs B.18, B.19 and B.20, the mean, mean squared and standard deviation of the recovered error can be minimized when the phase constants are equivalent and their magnitudes are maximized. These two conditions can be used towards optimization of the reference excitation amplitude and phase parameters.

3.3. Determination of reference excitation amplitude and phase

As demonstrated in Appendix B, the mean and mean squared error functions indicate that the sine and cosine constants, K_s and K_c, respectively, must be maximized and equivalent to minimize the additive noise effects on the recovered optical phase [ATIS, 2006]. However, the optimization of these parameters is non-trivial due to the periodic nature of both functions and the infinite Bessel function summation in each equation. The convergence characteristics of these infinite power series must be investigated to provide a functional limit to the power series terms for calculations.

Convergence is tested over $\psi = 0$ to 2π and $\theta = -2\pi$ to at d = 1% to 25%. The convergence and convergence rate was calculated numerically using MatLab 7.3 [2006] using a 100x100 point grid and whole number duty cycles (1%, 2%, etc.). As shown in Figs 3.2 and 3.3, K_s and K_c converge to their final values within six iterations of the power series for $\psi = 6$ rad, $\theta = 5$ rad and $d = 10\%$.

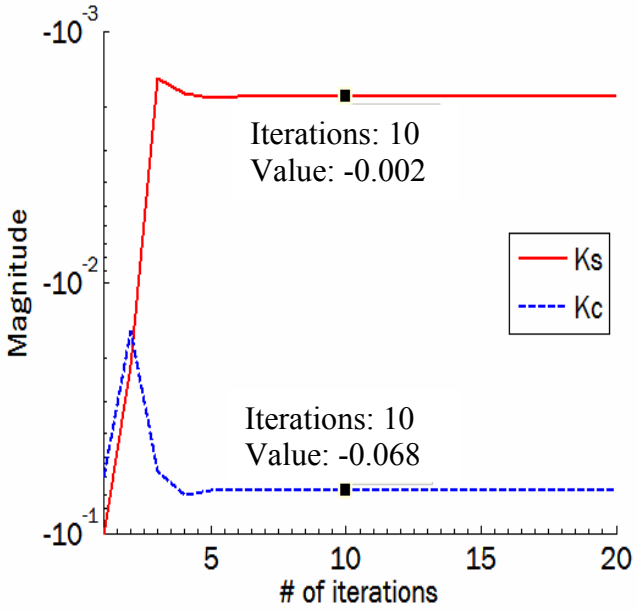

Fig. 3.2. Convergence of K_s and K_c for $\psi = 6$ rad, $\theta = 5$ rad and $d = 10\%$.

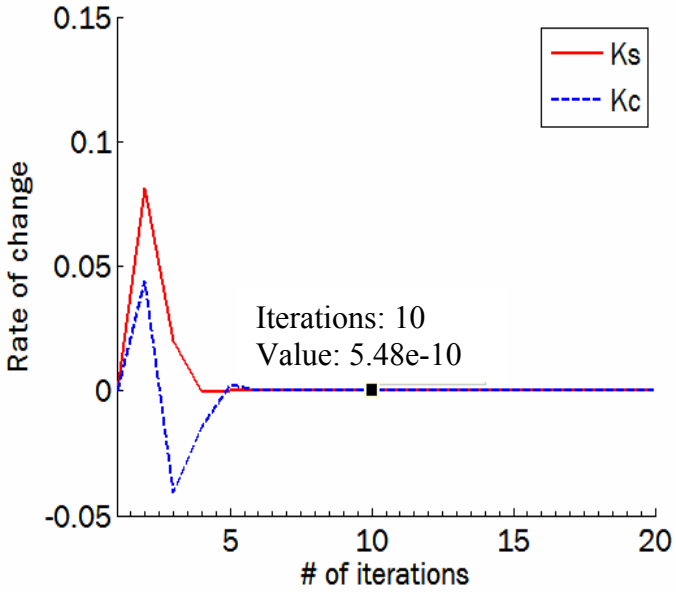

Fig. 3.3. Convergence rate of K_s and K_c for $\psi = 6$ rad, $\theta = 5$ rad and $d = 10\%$.

Similarly, convergence is reached for both the sine and cosine constants within 8 iterations of the infinite power series to a convergence rate of 1e-9 or better based on the maximum change found between subsequent iterations. This convergence is a result of the rapid amplitude decrease of Bessel functions of the first kind at increasing orders. As the Bessel function is a multiplicative factor, subsequent iterations of the power series have increasingly small effects on the value of the phase constants. Consequently, all subsequent calculations are done at a power series limit of 10 to ensure convergence within the range of ψ and θ of interest.

With the acceptable summation limit, the behavior of the K_s and K_c can be investigated relative to the variables in each equation. According to the derived equations, K_s and K_c are periodic with respect to the reference excitation amplitude and phase values. However, they are also dependent on the duty cycle of the stroboscopic

illumination source. Figures 3.4 to 3.9, display periodicity of these constants between 0 and 2π radians in both amplitude and phase. Multiple stroboscopic duty cycles are presented to illustrate its effects on the calculated phase constant maps.

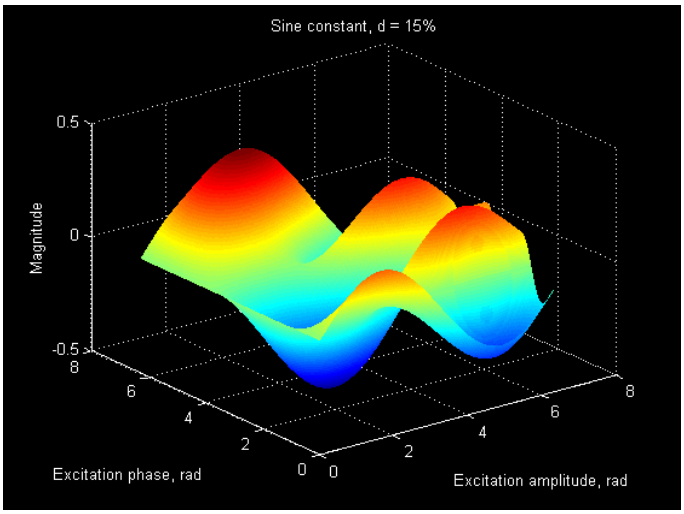

Fig. 3.4. Representation of K_s at 15% illumination duty cycle.

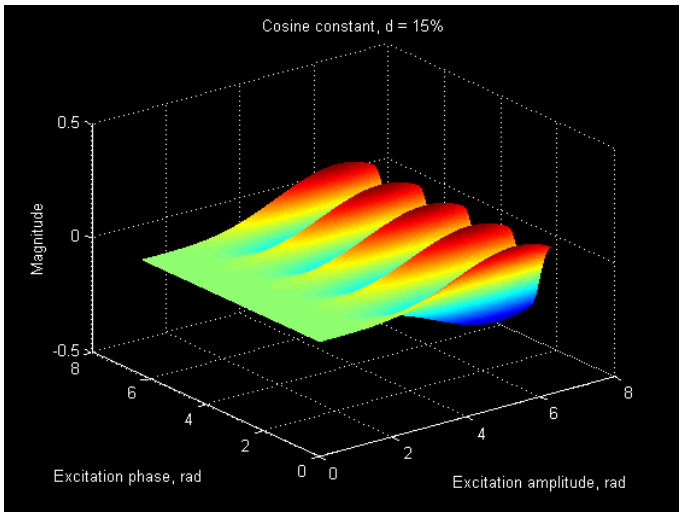

Fig. 3.5. Representation of K_c at 15% illumination duty cycle.

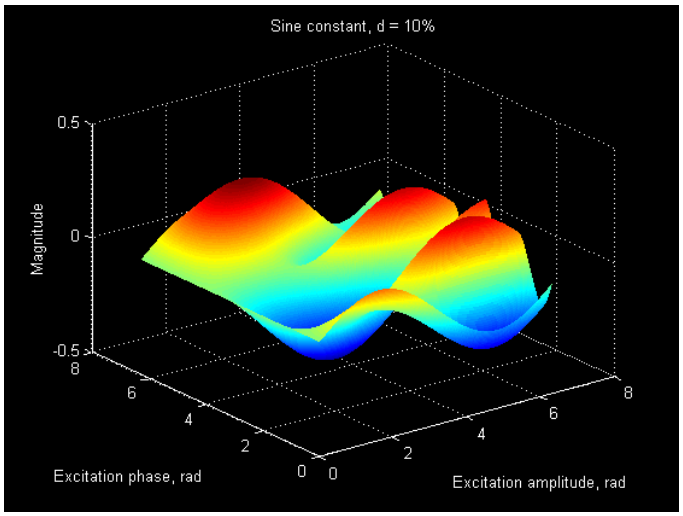

Fig. 3.6. Representation of K_s at 10% illumination duty cycle.

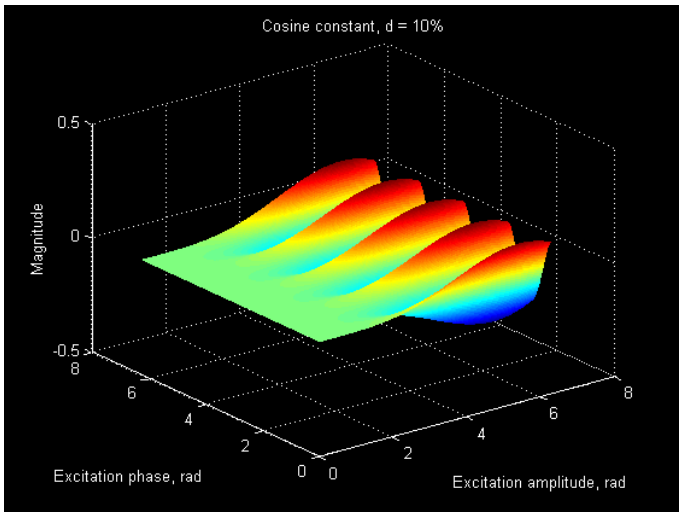

Fig. 3.7. Representation of K_c at 10% illumination duty cycle.

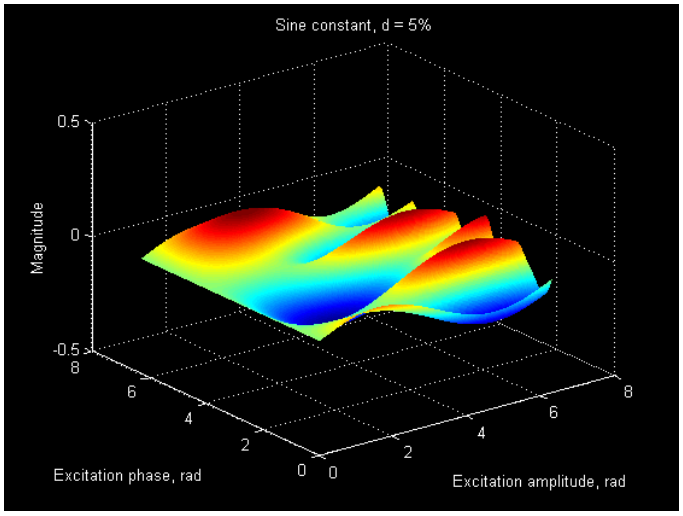

Fig. 3.8. Representation of K_s at 5% illumination duty cycle.

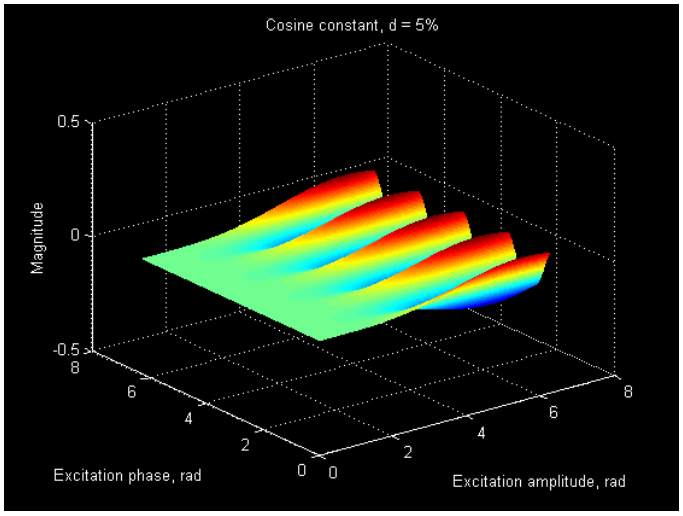

Fig. 3.9. Representation of K_c at 5% illumination duty cycle.

From Figs 3.4 to 3.9 and Eqs 3.18 and 3.19, it is shown that amplitude of the sine and cosine constants is varies sinusoidally from an absolute maximum of K_s and K_c of 0.21 and 0.20 respectively at d = 14% to zero as the stroboscopic duty cycle approaches zero or 25%. As expected, from Eqs 3.18 and 3.19, the magnitude of the sine and cosine constants at a given duty cycle is sinusoidally related to the excitation phase. Similarly,

the magnitudes of the phase constants are nonlinearly related to the excitation amplitude due to dependence on Bessel function of the First Kind. Additionally, as shown in the sine constant term, the magnitude decreases more rapidly at lower excitation amplitudes shifting the relative magnitudes of local peaks. From these observations, it becomes apparent that the calculation of ψ and θ should be done independently at each illumination duty cycle of interest.

The periodic nature of K_s and K_c will lead to multiple points of intersection between the surfaces over the $0 - 2\pi$ range resulting in the appearance of many local maxima. For simplicity, this Thesis solves for a combination of parameters that indicate the location of a local maximum that requires a minimal value of amplitude in the reference excitation. This is advantageous at higher reference excitation frequencies with respect to the jerk experienced by the reference mirror as the jerk experienced under sinusoidal modulation will scale by ω^3.

Due to the complex nature of the sine and cosine constant terms, optimal values of ψ and θ were solved iteratively rather than in a closed form solution using Mathcad [Mathcad r.12, 2004]. Graphically, the system of equations can be solved by

1) the generation of a mask showing the locations of equivalency between K_s and K_c at a given illumination duty cycle,
2) application of that mask to the corresponding map of either constant,
3) estimation of the local maxima location with respect to amplitude and phase.

As shown in Figs 3.10 and 3.11, the masks generated in step 1) demonstrate a stronger dependence on the illumination duty cycle than may be expected given the periodicity presented in Figs 3.4 to 3.9. From Figs 3.10 and 3.11, lines of equivalency between the

planes described by K_s and K_c are shown at d = 5 % and 15 %. These lines indicate regions where the mean error is zero although determination of local maxima is required to optimize ψ and θ. The complex forms of the 2-dimensional masks are suggestive of an underlying equation which may be applied towards the determination of ψ and θ in a closed form solution, though that work is beyond the scope of this Thesis.

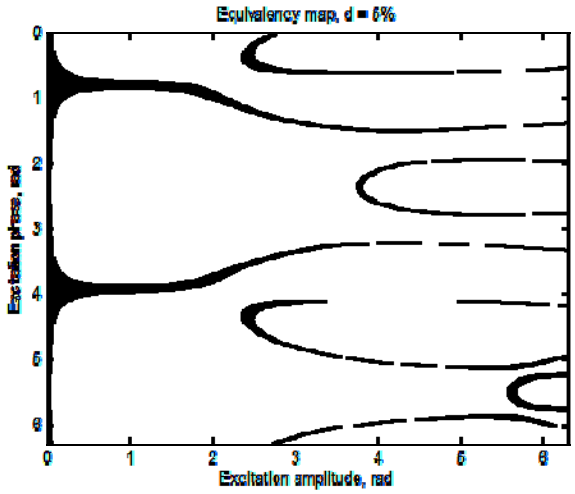

Fig. 3.10. Mask defined by the equivalency of K_s and K_c, d = 5%.

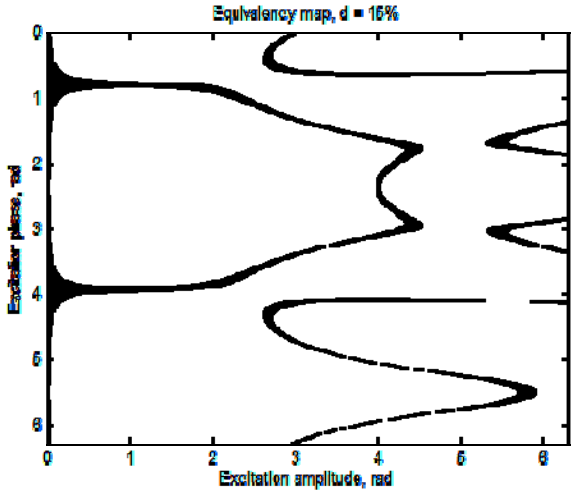

Fig. 3.11. Mask defined by the equivalency of K_s and K_c, d = 15%.

After appropriate calculation, optimal values of ψ and θ can be determined as a function of the illumination duty cycle. The values chosen for this Thesis are presented in Table 3.1 as well as in Figs 3.12 and 3.13.

Table 3.1. Reference excitation amplitude and phase versus illumination duty cycle.

Duty Cycle, *d* (%)	**Amplitude, ψ (rad)**	**Phase, θ (rad)**	**Duty Cycle, *d* (%)**	**Amplitude, ψ (rad)**	**Phase, θ (rad)**
0.001	5.143	0.369	13.000	5.119	0.257
1.000	5.156	0.372	14.000	5.331	0.006
2.000	5.159	0.371	15.000	5.538	0.020
3.000	5.164	0.369	16.000	5.777	0.021
4.000	5.170	0.367	17.000	5.997	0.008
5.000	5.177	0.364	18.000	6.172	-0.020
6.000	5.185	0.359	19.000	6.293	-0.061
7.000	5.192	0.354	20.000	6.370	-0.106
8.000	5.197	0.347	21.000	6.426	-0.146
9.000	5.200	0.338	22.000	6.473	-0.178
10.000	5.197	0.327	23.000	6.152	-0.204
11.000	5.188	0.312	24.000	6.558	-0.225
12.000	5.166	0.290	25.000	6.813	-0.083

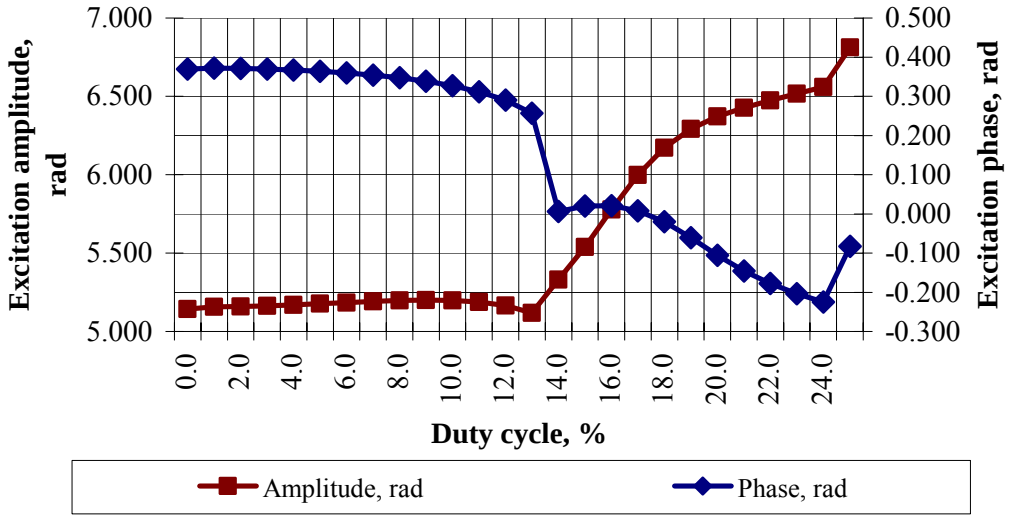

Fig. 3.12. Reference excitation amplitude and phase versus illumination duty cycle.

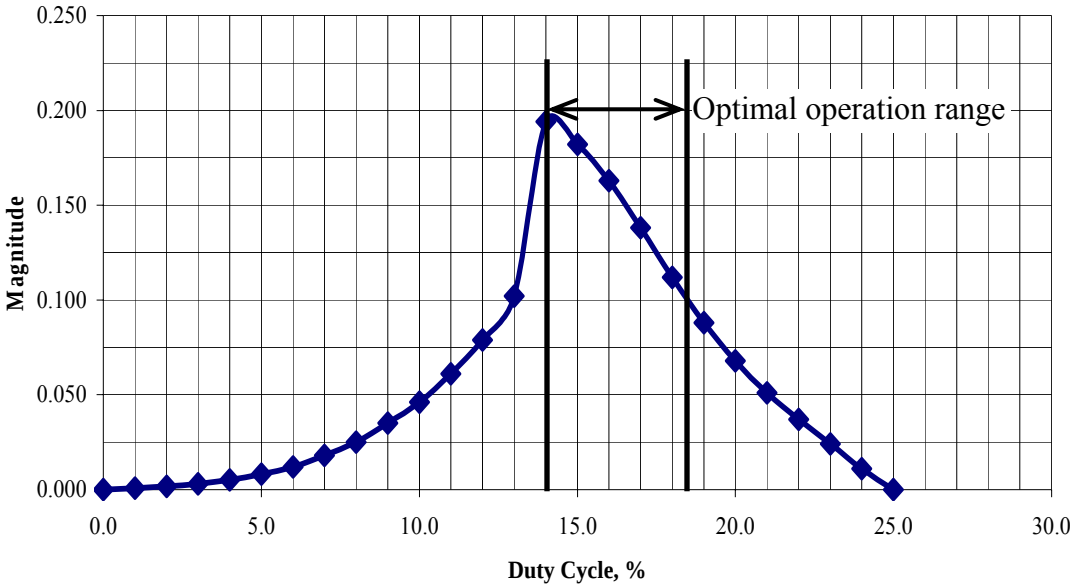

Fig. 3.13. Phase constant magnitude versus illumination duty cycle. The optimal operation range shown is within d = 14% to 18.5% and limited to 50% of the maximum magnitude.

The plots shown in Figs 3.12 and 3.13 highlight the highly nonlinear relationship between the illumination duty cycle with both the reference excitation amplitude and phase. Though not a completely unexpected behavior given the mathematical system being solved, this observation indicates that implementation of the sinusoidally modulated system requires care in the selection of the illumination duty cycle as linear interpolation may not provide an accurate estimation of parameters away from those explicitly calculated. This is most apparent between an illumination duty cycle of 13% and 14% due to a discontinuity within that range at d = 13.45%. Other implementation recommendations become apparent when considering the charted data.

As found in Appendix B, the mean squared additive error is inversely related to the squared magnitude of the sine and cosine constants. This condition led to the maximization of the equations describing those values and, in part, allowed for the

creation of the plots described in Figs 3.12 and 3.13. However, as shown in Fig. 3.13, the optimization of ψ and θ leads to a variation in magnitude of K_s and K_c with respect to the duty cycle, d. This causes the value of the mean squared additive error to be proportional to the stroboscopic duty cycle used. As shown in Fig. 3.13, a maximum constant magnitude exists at d = 14%. Therefore the mean squared additive error will be minimized when operating at this duty cycle. Also from Fig. 3.13, the optimal operation range is d = 14 to 18% where the magnitude of the upper limit is half of the maximum. It becomes apparent that the stroboscopic duty cycle should not be set between 13% and 14% as a discontinuity exists in the above charts. By refining the calculated values within this range, a step discontinuity appears at d = 13.45%. Consequently, while interpolation appears to provide a reasonable estimation of the excitation magnitude and phase values within the operational range, it cannot be applied from d = 13% to 14% though the magnitude of the sine and cosine constants is high in this region.

Figure 3.13 provides operational limits to the sinusoidal phase modulation system. Between d = 0% to 5%, the magnitude of the phase constants is $<{}^{1}/_{10}{}^{th}$ of peak. This indicates that while operation is possible under ideal conditions, any small errors will be accentuated due to the inverse relationship between mean squared error and phase constants magnitude shown in Appendix B. Operation at these low illumination duty cycles requires alternative combinations of excitation amplitude and phase parameters that may provide a higher phase constant magnitude. However, this limitation may be dealt with by increasing the reference excitation frequency until the acquisition time at the higher duty cycle is that required experimentally.

4. IMPLEMENTATION

Realization of a phase modulating interferometer requires a controllable imaging system with a stroboscopic illumination source coupled to an optical path length modulation system. The derived technique assumes synchronization between the optical path length modulation and the stroboscopic illumination period. Similarly, the optical path length modulation amplitude and relative phase must be set to minimize errors in the recovered optical phase map due to additive noise effects. This synchronization is accomplished through software control of a National Instruments analog output card [National Instruments, 2006] controlling a piezoelectric phase modulator [Furlong and Pryputniewicz, 2004b], illumination source [Opto Diode, 2006], and CMOS camera system [PixeLINK, 2006]. The configured interferometric system, with all required external components, is schematically presented in Fig. 4.1 with signal I/O connections indicated in Table 4.1.

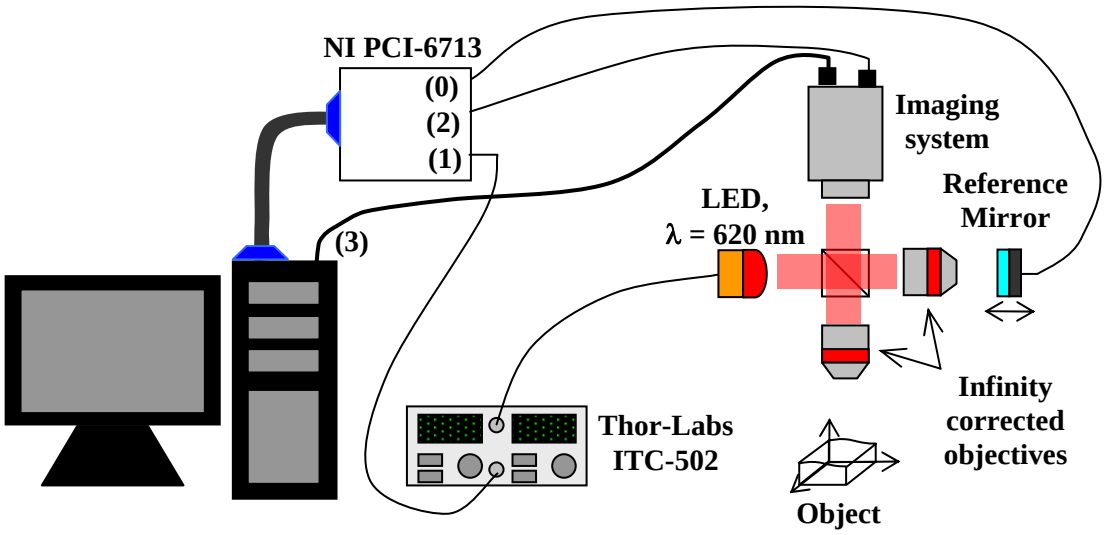

Fig. 4.1. Schematic representation of PMI system described in this Thesis.

Table 4.1. System connectivity chart.

Input	Output	Cable	Purpose
PCI-6713: Ch. 0	Piezoelectric phase modulator	BNC	Reference path modulation
PCI-6713: Ch. 1	ITC-502, Analog Mod.	BNC	Illumination modulation
PCI-6713: Ch. 2	PL-A741, vision control	BNC	Camera trigger control
ITC-502, Analog Mod.	OD-620L	BNC	Illumination power supply
Computer	PL-A741, data port	FireWIRE	Data exchange

4.1. Experimental system

A Linnik configured interferometer was chosen as the platform for this PMI system [Dyson, 1970; Greivenkamp and Bruning, 1992; Kreis, 2005]. As shown in Fig. 4.2, this configuration is very similar to the Michelson configuration. The primary difference between the two systems is the addition of an infinity corrected objective along each arm of the interferometer.

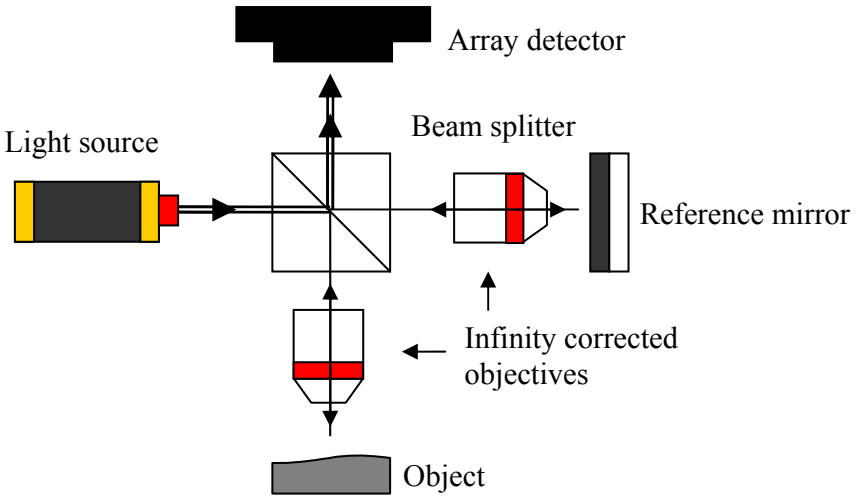

Fig. 4.2. Linnik configured interferometer [Wyant, 2002; Kreis, 2005].

These objectives allow for adjustment of the system magnification power while providing a relatively simple means for maintaining the same unmodulated optical path length in each arm. An advantage to this configuration is the wide variety of allowable illumination sources both long and short coherence.

For this work, a PixeLINK PL-A741 1.3 megapixel monochrome camera is used as the imaging system due to its high-performance and FireWire control capabilities [PixeLINK, 2006]. As presented in Fig. 4.3, the PL-A471 has peak quantum efficiency at 660 nm meaning that an illumination source at this wavelength will require a lower output power to generate the same acquired intensity value. Therefore, the control system will generate the lowest stroboscopic modulation amplitude at this wavelength, decreasing the response time and overshoot of the illumination source [Thor Labs, 2006; Opto Diode, 2006].

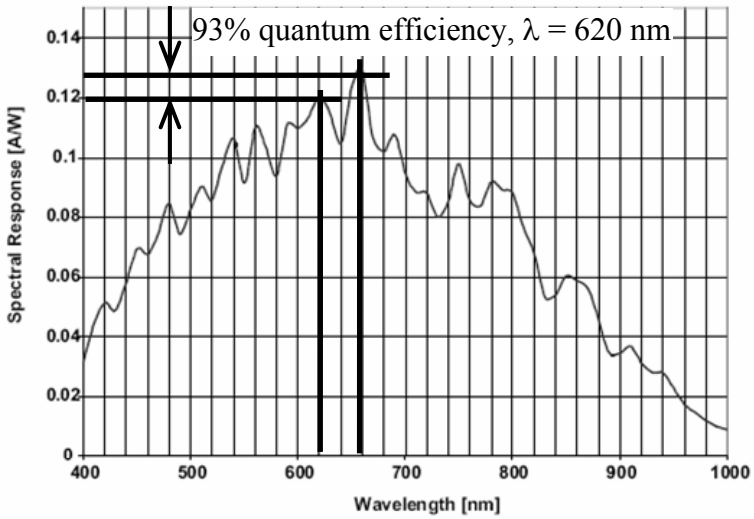

Fig. 4.3. PL-A741 quantum efficiency curve, peak λ = 660 nm [PixeLINK, 2006].

Consequently, a high output LED from Opto Diode was chosen as the stroboscopic illumination source due to the multiple illumination wavelengths available. The chosen OD-620L has 23 mW of power output at 300 mA with a primary wavelength of 617 nm. The camera is highly sensitive to this wavelength, as seen in Fig. 4.3, demonstrating a quantum efficiency of 93%. The coherence length was calculated as 16.8 μm based on Eq. 4.1 and the published spectral output curve shown in Fig. 4.4.

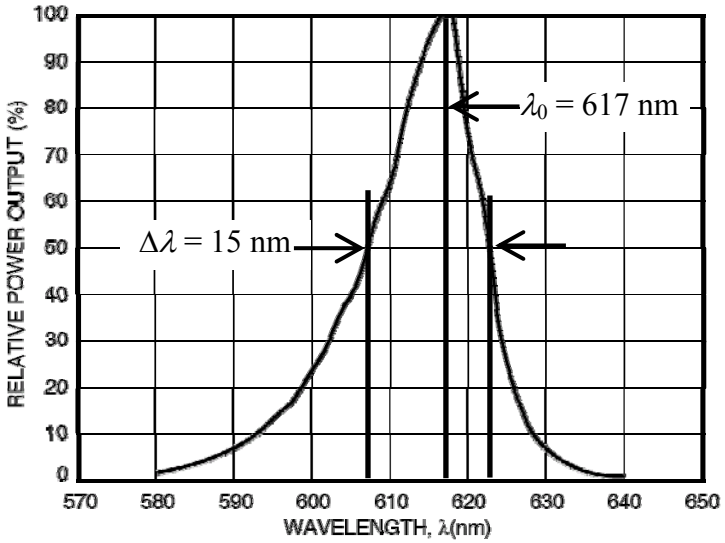

Fig. 4.4. OD-620L spectral output showing peak and full width at half modulation points for determination of coherence length, l_c. l_c is determined to be 16.8 nm [Opto Diode, 2006].

$$l_c = \sqrt{\frac{2\ln(2)}{\pi}} \cdot \frac{\lambda_0^2}{\Delta\lambda} \quad . \tag{4.1}$$

where λ_0 is the peak output wavelength of the Opto Diode LED (617 nm) and $\Delta\lambda$ is the full width at half modulation (15 nm) as shown in Fig. 4.4.

A Thor Labs ITC502 ±200mA /16W bench top laser diode controller was used for illumination control due to an output noise level of <1.5μA and setting resolution of

±10μA output noise and low temperature drift while providing analog modulation in constant current mode at a maximum frequency of 500kHz. Output current is modulated with an input voltage signal at 20 mA/V ±5% [Thor Labs, 2006].

The piezo-actuator used in this Thesis was previously modified from a commercially available piezoelectric device from RadioShack® [RadioShack, 2006]. The voltage to displacement ratio was found to be 100.58 nm/V through application of the five phase-shifting algorithm developed by Hariharan, et al. [1987]. The linearity of the displacement curve is demonstrated in Fig. 4.5 where the voltage dependent displacement is correlated to a linear fit with a $R^2 = 0.99$ to a $\sigma = 10.5$ nm or 1.70% at 620 nm.

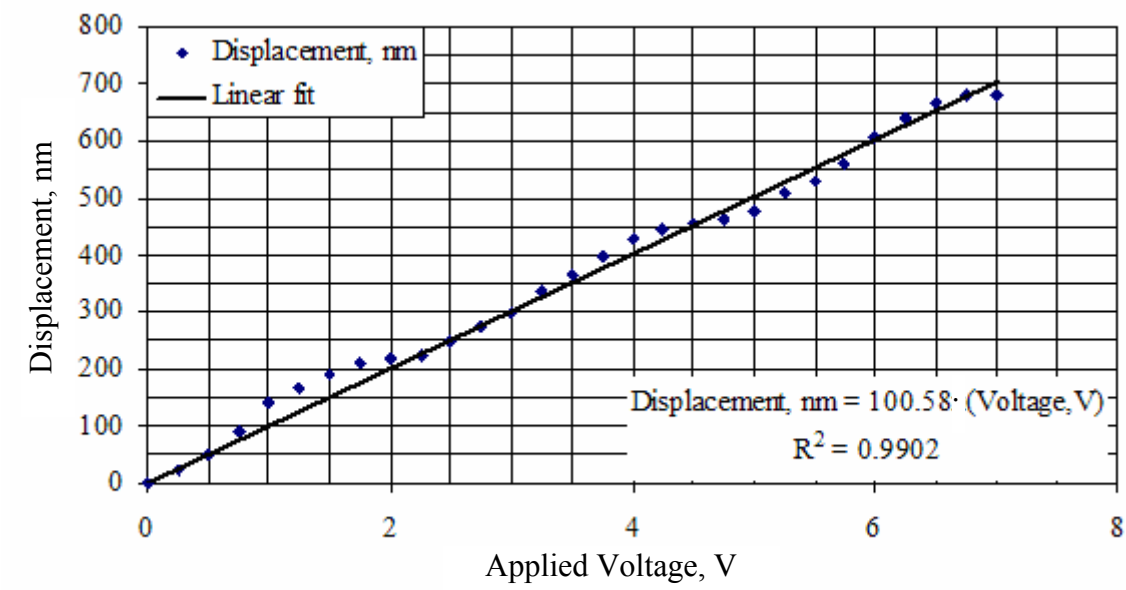

Fig. 4.5. Voltage dependent displacement of the actuator used for phase modulation during the experimentation conducted within this Thesis.

This high degree of linearity in the displacement curve presented in Fig. 4.5 indicates that no additional calibrations are required to ensure a linear displacement of the actuator as

this 1% modulation error will correspond to a maximum error in the recovered phase map of 0.65 nm at $\lambda = 620$ nm under PSI operation which is within the published experimental uncertainty of both systems [Sasaki and Okazaki, 1986a; Creath, 1988; Sasaki, et al., 1990a; Surrel, 1993]. This can be assumed for the lifecycle of the actuator as piezoelectric actuators have demonstrated a lifespan in excess of 10^9 cycles with minimal changes in their displacement characteristics when operating under low to moderate displacements under controlled environmental conditions [Physik Instrumente, L.P., 2005]. However, the magnitude of the displacement rate should be verified, as above, before each experiment with this actuator system to correct for any drift experienced due to any changes in the environment or fixturing.

Control and modulation signals are generated by the National Instruments PCI-6713 card controlled through the LabVIEW™ programming environment. This card provides 12-bit arbitrary waveform generation at 1 MS/s between a maximum range of ±10 V at frequencies on up to 8 channels [LabVIEW™ 7.1, 2006]. Individual channels are automatically synchronized with a relative output phase of 0 rad based on an internally created trigger signal. Additional control is available through the National Instrument Measurement & Automation Explorer (MAX) configuration utility for debugging and testing purposes.

4.2. Software development

The LabVIEW™ programming environment was chosen to meet the control needs of the phase modulating interferometer due to its ease of use and ability to interface

with both FireWire systems and the National Instruments PC control cards [LabVIEW™ 7.1, 2006]. LabVIEW™ is a graphical development environment for creating flexible and scalable design, control, and test applications rapidly and at minimal cost from National Instruments. With LabVIEW™, software development becomes four to 10 times faster than in other programming languages because of its specific design for engineers and scientists [National Instruments, 2006]. Additionally, it automatically multitasks and multithreads tasks to optimize processing time. Unlike text based programs, the "code" is written in a block diagram format similar to a flow chart design allowing for rapid debugging and program augmentation [LabVIEW™ 7.1, 2006].

A LabVIEW™ program will, inherently, have two components: the front panel and the block diagram. The front panel is, simply, the user interface (UI). It is automatically generated during block diagram programming though the final version is fully customizable as with comparable graphical programming languages. A subsection of the developed UI is presented in Fig. 4.6. A more complete view of the developed front panel is presented in Appendix C.

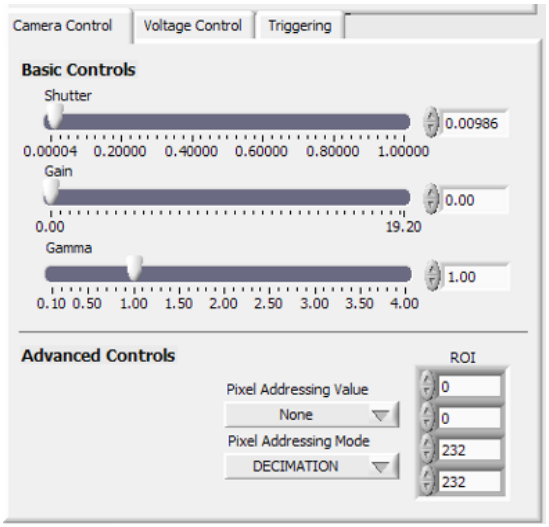

Fig. 4.6. Sample front panel of developed LabVIEW™ interface.

The block diagram side of a LabVIEW™ program contains the developed code as written for this Thesis. While code can be imported from standard C, C++, MatLab, etc. most programs are inserted by way of the LabVIEW™ VI system. These VIs or virtual instruments are pre-parsed, pre-compiled code blocks which can be used to accomplish tasks much like commands in standard programming languages. By wiring corresponding terminals of various VIs during application development, it is possible to perform the required tasks [Bitter et al., 2000; LabVIEW™ 7.1, 2006]. At the heart of LabVIEW™ is structured dataflow diagramming. It is, in fact, a much richer computational model than the control flow of popular text-based languages because it is inherently parallel while C/C++ and BASIC are not. As traditional languages must rely on library calls operating system functions to achieve parallelism, the compiler can not ensure shared sections of code are properly protected within the operating system, making it difficult to build parallel programs. These problems do not exist in LabVIEW™ as the compiler does not have to parse the diagram, because it is already

parsed [LabVIEW™ 7.1, 2006]. A small sample of the code written for the interferometric system is presented in Fig. 4.7.

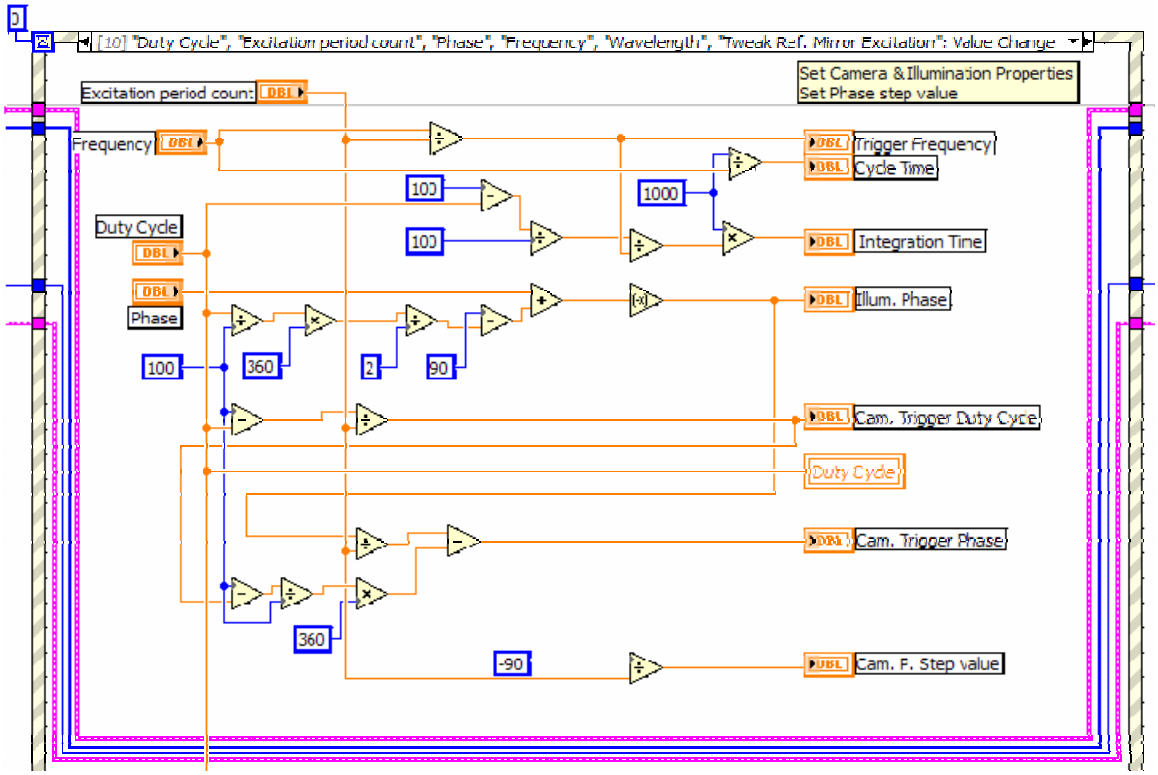

Fig. 4.7. Sample of developed LabVIEW™ block diagram.

According to Fig. 4.7, each icon represents a particular task or value where the blue and orange wires are used to connect these icons and so define the program flow. In this case, the integration time of the camera can be traced to find its dependence on the reference excitation frequency, the stroboscopic illumination duty cycle, and a term called the excitation period count which defines the number of stroboscopic pulses included in each acquisition period. Appendix D shows the full block diagram code developed for the interferometric system with descriptions of individual code sections.

4.2.1. Installation

The developed software was written in LabVIEW™ 7.1 with the NI-IMAQ 3.1 (IMAQ™ Vision for LabVIEW™) and NI Measurement & Automation Explorer 4.0.2 (MAX) packages. The NI-IMAQ (IMage AcQuisition) package expands the base LabVIEW™ image acquisition/processing/saving capabilities. NI MAX includes features for configuring and testing input\output capabilities, as well as storing, scaling, calibration, and channel-aliasing information, important for achieving short time to first measurement and for maintaining and troubleshooting test systems without additional programming. Performance increases with MAX because multiple threads can access the NI-DAQmx driver at the same time as long as those threads are executing different NI-DAQmx tasks. Functionally, this allows multiple channels to execute synchronously on multiple channels of the same PCI card [LabVIEW™ 7.1, 2006].

Direct camera control is accomplished through the camera's FireWire port and TTL signals from the PCI-6713. FireWire control is based on VIs provided by PixeLINK. These supplied VIs require the NI-IMAQ 3.1 package due to their reliance on high end image processing functions not available in the base LabVIEW™ 7.1 installation package. This Thesis has adapted these VIs for simple parameter modifications within the operating LabVIEW™ environment. It is suggested that camera properties be preset using external PixeLINK Capture OEM software for speed and ease of use as the PL-A741 will maintain operational settings while it is powered. Software and hardware installation procedures are outlined in Appendix E.

4.2.2. Operation

Due to the requirements of the phase modulating interferometer, a flow chart was developed to direct the programming work. This chart, presented in Appendix F, demonstrates a standard operational procedure. Functionally, the developed code must:

1. Control the imaging camera (gain, gamma, shutter period, etc.).
2. Display the raw images returned from the camera.
3. Generate the magnitude and phase of the reference modulation signal relative to the illumination cycle.
4. Synchronize both the reference modulation and the illumination cycles with the camera acquisition period.
5. Acquire four interferograms over the reference modulation period.
6. Calculate and display the wrapped phase and optical modulation maps based on the presented mathematics.
7. Save the acquired interferograms and calculated maps.

Synchronization of the analog signals requires the frequency and relative phase of each output channel be known. To ensure synchronization, the signal controlling the reference modulation also serves as the trigger frequency for the system. As a result, all other output parameters can be fixed relative to the phase and frequency of this modulation signal. As such, the user interface only allows direct control of the phase or frequency parameter of this signal, excepting a parameter known as “excitation period count.” While the amplitude of the stroboscopic illumination signal is independently

controllable, its frequency can only be adjusted by modification of the excitation period count. This parameter allows for the acquisition time to occur over multiple reference excitation periods. The result is a linear averaging in the resultant interferogram at a particular phase on the reference modulation signal which serves to reduce transient effects, both environmental and systematic [Agilent Technologies, Inc., 1999]. Additionally, when there is poor reflectivity from an object of interest, this parameter provides a means of increasing the number of photons absorbed by the CMOS array without adjustment of the reference modulation signal frequency. Appendix G provides a detailed description of additional user interface parameters as displayed in Appendix C.

Limitations in the developed code will be further discussed in the Future Work Section of this Thesis; however, several operational issues must be noted. Of primary concern is the square region of interest requirement in the developed software. As the base PixeLINK VIs and OEM control are optimized for viewing by the user, they do not capture nor display a continuous stream of images from the A741 camera system. Directly tapping this video feed for processing results in periodically missing frames preventing display of the correct optical phase map. As a result, the base code was adapted so that frames would be acquired as needed and recovered as a 2-D array rather than as a coherent image. While this approach prevents the loss of image data, it limits the speed of the system and requires a square region of interest to correctly display the originally acquired frame. Due to a non-standard indexing used in the PixeLINK camera system, all other region of interests will not display correctly in the currently developed software package. Functionally, this approach also requires the camera trigger signal to

be the first thing turned on when operating the system. Otherwise the system will lock up as it waits for the camera to provide a frame to the processing code.

Additionally, the developed program is not configured for true real-time display of the unwrapped phase map. The current display is at a rate of several frames per second. This limitation is primarily due to the need to generate a sinusoidal waveform within the developed code. This creation process requires a significant portion of the processing time and so greatly slows the overall program speed. Processing time may be reduced in further developments through external creation of the sinusoidal signal or the addition of other LabVIEW™ packages for further optimization.

5. REPRESENTATIVE RESULTS

The measurement and spatial resolution of the phase modulating system was tested to provide experimental verification of the presented mathematics as well as of the developed control system. The spatial resolution and field of view were tested, noninterferometrically, with a negative 1951 USAF glass target by Edmund Optics™ [Edmund Optics, Inc., 2006]. Measurement resolution and accuracy was determined through measurement of a 500Å ± 2.5% thick gold film National Institute of Standards and Technology (NIST) traceable gauge [Veeco Metrology Group, 2002]. Lastly, shape and displacement testing of a series of μHexFlex devices from the Precision Compliant Systems Laboratory at MIT was conducted demonstrating the applicability of the phase modulating system in MEMS applications. All shape and displacement measurements were verified with a phase stepping algorithm also implemented through the LabVIEW™ environment on the same system. With a developed interface functionally identical to the phase modulating controls, the use of phase stepping allows for rapid measurement comparisons. Shape measurement results correlate to within 0.2 nm between the two interferometric techniques.

5.1. Spatial resolution

The 1951 USAF shows several groups of test target elements, which conform to Military-Standard-150A. Each group consists of six elements, which are progressively smaller by

$$l_l = \frac{2.5mm}{2^{Group+(Element-1)/6}} \quad , \tag{5.1}$$

where l_l is the line length in millimeters for a given group and element [Glynn, 2002]. The elements within a group are numbered from 1 to 6 and group numbers progress from 0 - 9. The first element of even-numbered groups is at the lower right, with the remaining five elements, 2 through 6, at the left as shown in Fig. 5.1.

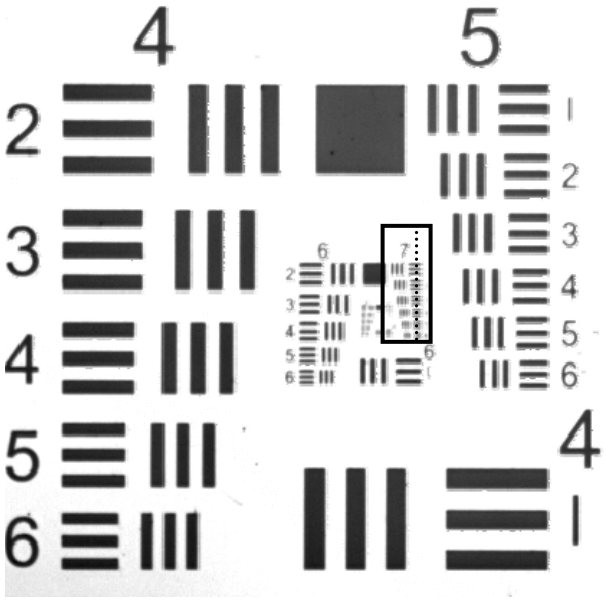

Fig. 5.1. Recorded USAF 1951 negative glass target with group 7 outlined for containing the smallest resolvable element set [Edmund Optics, Inc., 2006].

As shown, the negative glass target allows for the lines within each group to appear dark relative to the reflective surface surrounding each element set. Due to the age of the standard, no standardized quantitative metric exists to determine the ultimate spatial resolution recoverable from the target. With the advent of modern imaging arrays, it has become common practice to extract a line profile along the least resolvable elements,

given by the dotted line in Fig. 5.1, and determine the ultimate spatial resolution at the element containing individually resolvable lines at a contrast level of 10% based on a spline data fit, as shown in Fig. 5.2.

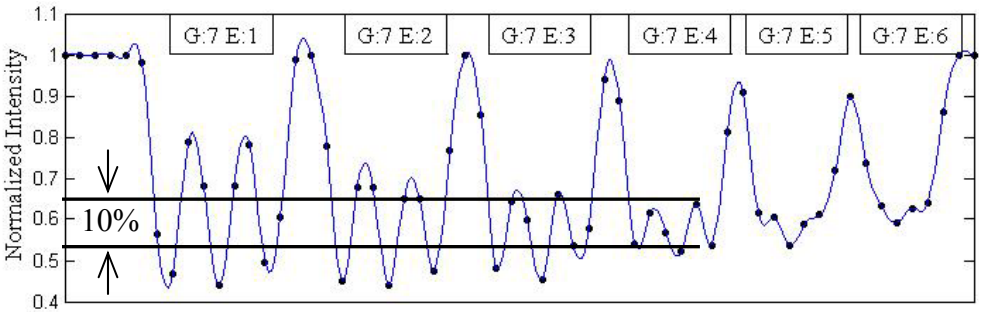

Fig. 5.2. Spline-fit intensity profile of pixels extracted along horizontally oriented bars in Group 7 of the USAF-1951 negative glass target.

Through this procedure the limiting element set is found to be group 7 element 4 at a spatial frequency of 181.019 line pairs/mm or spatial resolution of 2.762 μm.

Similarly, a pixel profile taken along to the element lines can be used to determine the field of view of the imaging array. For a 4x magnification and use of a 1280 × 1024 imaging array, the maximum field of view is found as 2.967 × 2.373 mm or 432 pixels/mm.

5.2. Measurement resolution and repeatability

The sensitivity, accuracy, and precision of the phase modulating system are characterized with the aid of a 500 Å ± 2.5% gold film NIST traceable gauge specifically designed, constructed and certified for OEHM measurements [Veeco Metrology Group,

2002]. This characterization is important to determine the reliability and applicability in high-resolution measurements, as required in MEMS devices. Figure 5.3 depicts the chosen gauge.

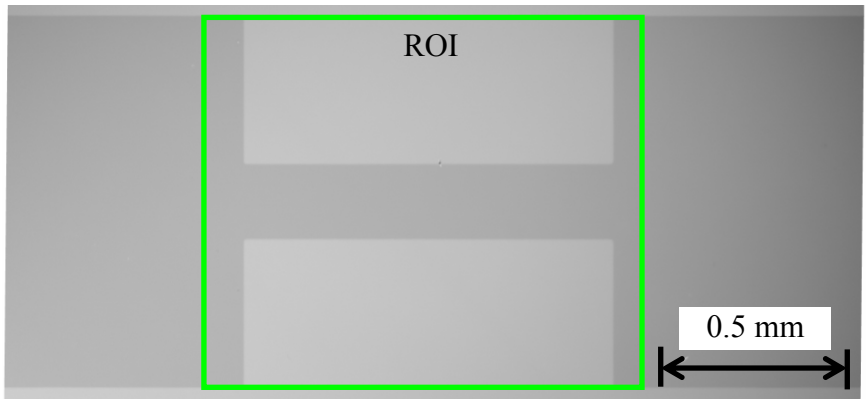

Fig. 5.3. 500Å ± 2.5% goal film NIST traceable gauge used for characterization of optoelectronic holographic methodologies [Veeco Metrology Group, 2002].

Measurements are carried out using a 4x magnification with a CMOS camera containing 1280 × 1024 active pixels at 8-bit digitization with a region of interest indicated in Fig. 5.3. Measurements involve:

1) performing high-resolution phase modulation calibration [Hariharan et al., 1987],
2) optimizing the beam ratio between the reference and objective arms to maximize the fringe contrast,
3) adjustment of the interferometric and focal planes to maximize contrast at the surface of the gold film,
4) removal of carrier fringe pattern from the full field of view,
5) adjustment of operation properties within developed control system,

a) wavelength: 620 nm,

b) modulation frequency: 50 Hz,

c) stroboscopic amplitude: 0.25 V,

d) illumination duty cycle: 14%,

e) trigger mode: Low Integrate,

f) trigger polarity: Positive (PMI) / Negative (PSI).

Both phase modulating and phase stepping interferometry techniques were used for shape extraction to demonstrate the correspondence of both methods on the developed system. Before experimentation, the displacement rate of the phase modulator is verified to be 100.58 nm/V [Hariharan, et al., 1987]. Determination of the optical phase is similar in each technique. The implemented systems require the acquisition of four interferograms at known relative phase values. These interferograms, seen in Fig. 5.4, represent an interferograms acquired at 1.33 radian phase-shifts in phase modulating mode and a $\pi/2$ phase-shift under phase stepping.

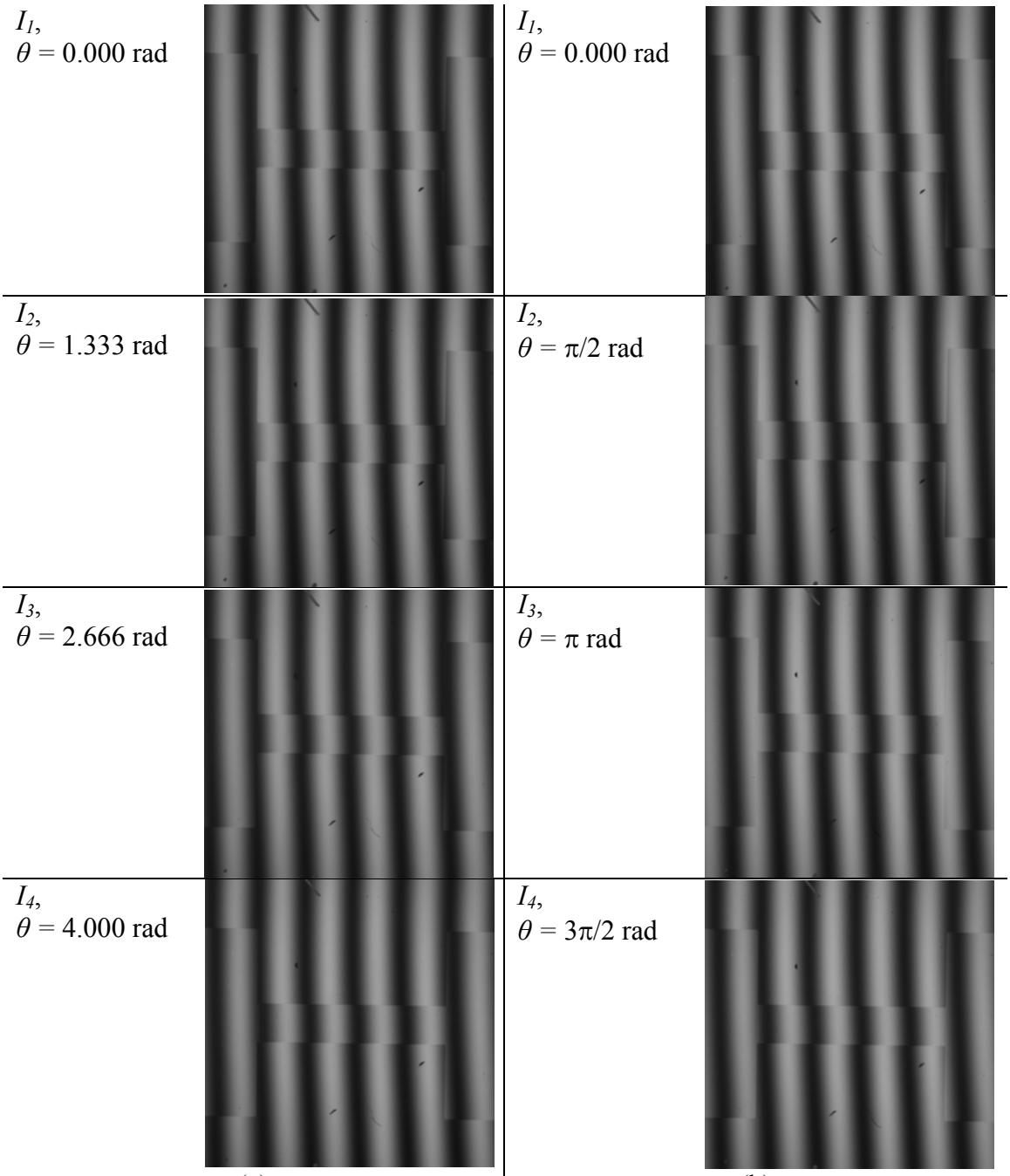

Fig. 5.4. Interferograms acquired with phase modulating interferometry (a); and with phase stepping interferometry (b).

Extraction of the optical phase requires the arctangent calculation of a sine and cosine term in both techniques. Phase modulating interferometry calculates the sine or numerator as

$$\Sigma_s = -I_1 + I_2 + I_3 - I_4 \quad , \tag{5.2}$$

and the cosine or denominator as

$$\Sigma_c = -I_1 + I_2 - I_3 + I_4 \quad , \tag{5.3}$$

as shown in Section 3, where I_1 to I_4, represent the interferograms acquired at the quadrature points of the sinusoidal modulation signal. Similarly, phase stepping calculates the sine and cosine terms with

$$\Sigma_s = I_1 - I_3 \tag{5.4}$$

and

$$\Sigma_c = -I_2 + I_4 \quad , \tag{5.5}$$

respectively using a standard four phase step algorithm with relative phase-shifts of $\pi/2$ from 0 to $3\pi/2$ radians [Kreis, 2005]. An arctangent function is then applied to a ratio of the calculated sine and cosine maps, as shown in Fig. 5.5, to extract the wrapped optical phase [Furlong, 2007]. As shown, the recovered wrapped phase maps are visually indistinguishable through the methods used to obtain each are significantly different. To determine the accuracy and repeatability of these data sets, they must be processed and quantitatively compared.

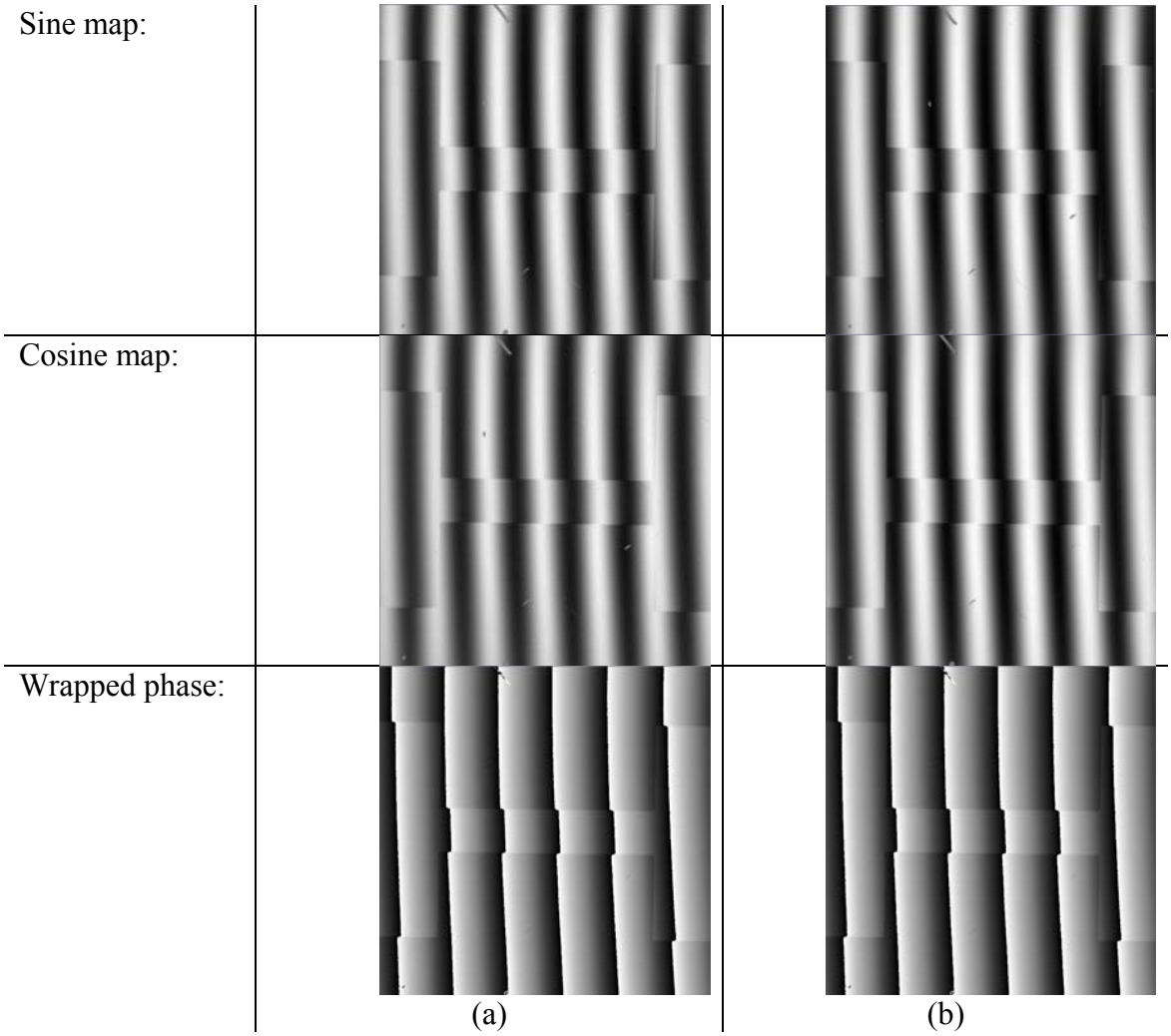

Fig. 5.5. Sine, cosine and arctangent maps calculated with phase modulating interferometry (a); and with phase stepping interferometry (b).

After gross removal of the object's tilt and all 2π discontinuities within the wrapped phase map, the recovered unwrapped data can be scaled by the wavelength of the illumination source to determine the shape of the object of interest. The recovered shape information is then imported into Imageware Surfacer to perform a difference analysis that evaluates the difference between a calculated plane and the measured shape information [Metrix, Inc., 2006]. Calculation of film thickness is accomplished by

extracting the difference value at multiple locations on both the substrate and gold film. These points, shown in Fig. 5.6, serve to eliminate any small tilt on the object of interest, as well as the effects of aberrant peaks or valleys within the recovered shape information.

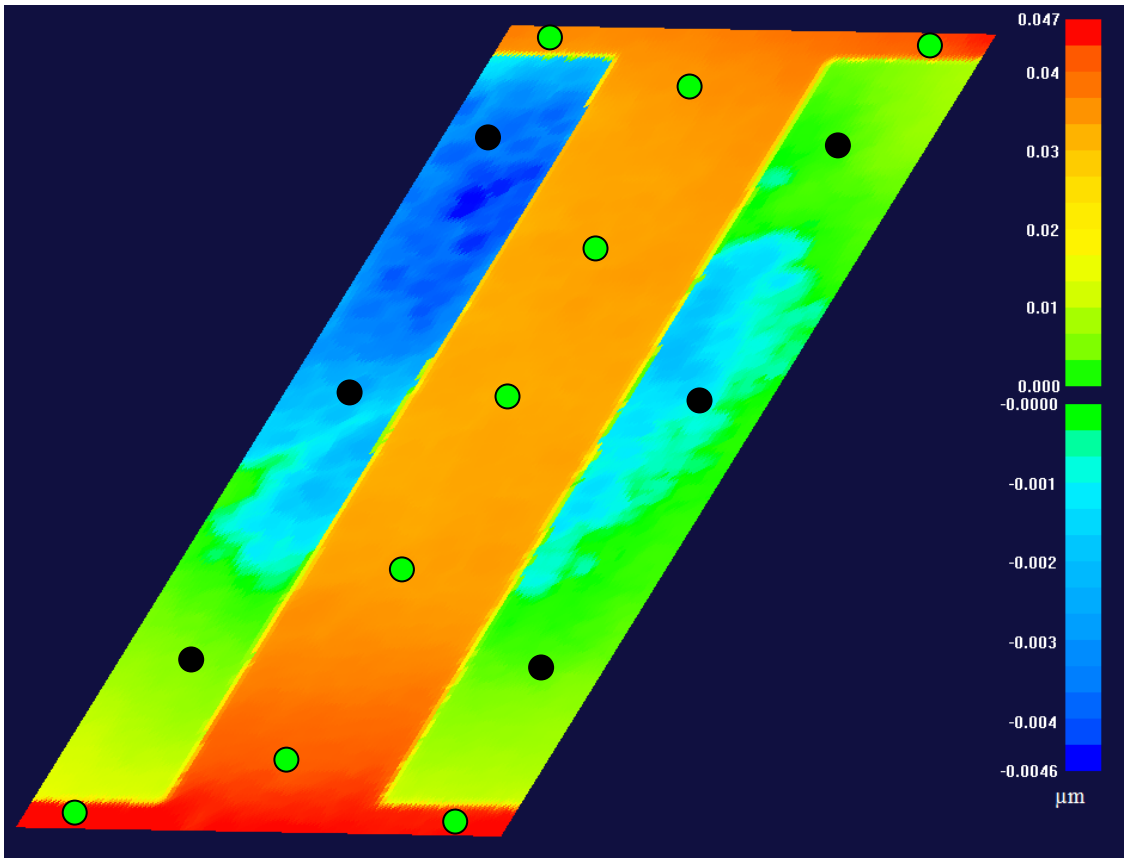

Fig. 5.6. Deviations from planarity as determined by difference analysis using phase modulating interferometry operating at f = 100 Hz, d = 14% indicated a nominal film thickness of 503 Å ± 7 Å under PMI. PSI methods indicated a nominal film thickness of 501 Å ± 7 Å [Furlong, 2007].

The recovered shape information indicates a nominal film thickness of 503 Å ± 7 Å under a sinusoidal phase modulation at f = 100 Hz and d = 14%. Similarly, phase stepping interferometry indicates a nominal film thickness of 501 Å ± 7 Å at f = 2 Hz and

d = 14%. These results are comparable to those indicated by Furlong [2007] with phase stepping interferometry and lie within the specified tolerance of the gauge device.

To demonstrate the reproducibility of the results obtained with phase modulating interferometry over a range of modulation frequencies, a low frequency test is conducted using both phase stepping and phase modulating interferometry through a statistical comparison of shape measurement results obtained by imaging of a reference flat under a f = 10 Hz modulation cycle. This is determined by taking two measurements, subtracting them, and looking at their root-mean-square (RMS) difference, standard deviation, absolute mean deviation, inter-quartile range, and linear correlation of the difference maps [Cohen, 1988; Creath, 1988; Montgomery, 2003; Gorard, 2004]. This difference should be less than $\lambda/100$ for comparison of well calibrated systems and less than $\lambda/300$ under low modulation conditions [Sasaki and Okazaki, 1986a; Sasaki, et al., 1990a; Creath, 1988].

The quadratic mean, or RMS value, may be used as it is less sensitive to outliers though will always be greater than or equal to the arithmetic mean, given by $\langle X \rangle$. The RMS can be calculated by

$$\langle X \rangle_{rms} = \sqrt{\frac{1}{n'} \sum_{m=1}^{n'} x_m^2} \quad , \tag{5.6}$$

where x is the data set of interest, k indicates a particular value from the data set, and n the total number of values present in data set x. The RMS is directly related to the standard deviation, σ, of a given data set by

$$\langle X \rangle_{rms}^2 = \langle X \rangle^2 + \sigma^2 \quad . \tag{5.7}$$

The shape measurement data acquired from both techniques has been adjusted so that its arithmetic mean will be equal to zero forcing the RMS value to be equal to the standard deviation of the data set. This mean is most useful when investigating data which contains both positive and negative components, as with a difference analysis as the arithmetic mean may be equal to zero though a large scatter may exist in the data set.

The standard deviation, σ, is equal to the square root of the variance of the data set. The standard deviation measures the spread of a data set from its arithmetic mean value or its overall uncertainty. In a large population, 75% of all data points will lie within 2σ. Larger values of standard deviation indicate that a given data may suffer from a high amount of noise or other experimental errors. It is calculated by,

$$\sigma = \sqrt{\frac{1}{n' - 1} \sum_{m=1}^{n'} \left(x_m - \langle X \rangle\right)^2} \quad , \tag{5.8}$$

which is necessarily always greater than or equal to zero due to the squared difference term.

The mean absolute deviation is an alternative to traditional standard deviation calculations. As shown in Gorard [2004], the standard deviation typically over estimates the statistical dispersion of a data set due to the use of the squared difference term. The mean absolute deviation, as given by

$$|D| = \frac{1}{n'} \sum_{m=1}^{n'} \left|x_m - \langle X \rangle\right| \quad , \tag{5.9}$$

typically uses the arithmetic mean of a data set and can be shown to be always less than or equal to the standard deviation [Gorard, 2004]. If the arithmetic mean is found to be an inappropriate measure of the central tendency of a data set, it can be replaced by the

RMS value within the presented equation. It has been shown that for an experimental data set with any level of randomness the mean absolute deviation "more efficient than the standard deviation … for distributions other than perfect normal [and is] closely related to a number of other useful analytical techniques [Gorard, 2004]." Both the standard deviation and mean absolute deviation are presented here to demonstrate the low level of data error in the acquired measurements while providing a secondary point of reference between the data sets.

The inter-quartile range serves as an additional comparison tool measures the spread of the middle 50% of the data when sorted from smallest to largest. As with the standard deviation, the smaller the IRQ value the tighter the data set. The IRQ is used as a way to remove the effects of outliers on a data set during analysis. This is most appropriately used when it is known that some degree of randomness exists in a data set independent of the measurable results. A common application of the IRQ is the removal of the outer 25% of the data set for linear correlation calculations [Cohen, 1988].

Correlation between the acquired data sets is calculated with the Pearson product-moment correlation coefficient. This method investigates linear relationships between two or more data sets by calculation of an R^2 value ranging from 0 to 1 with larger values indicating a stronger the linear relationship. This coefficient is calculated from [Cohen, 1998]

$$R^2 = \frac{\sum_{j}^{m}\sum_{k}^{n}\left(a_{jk} - \langle A\rangle\right)\cdot\left(b_{jk} - \langle B\rangle\right)}{\sqrt{\left[\sum_{j}^{m}\sum_{k}^{n}\left(a_{jk} - \langle A\rangle\right)^2\right]\cdot\left[\sum_{j}^{m}\sum_{k}^{n}\left(b_{jk} - \langle B\rangle\right)^2\right]}}\ , \tag{5.10}$$

where a and b are data sets of size m × n and, as previously, $\langle X \rangle$ indicates the arithmetic mean of a particular data set, x.

These statistical measures are used to describe the shape data presented here obtained with sinusoidal phase modulating interferometry and that with phase stepping interferometry. For comparison, testing is conducted at a 4x magnification under a modulation frequency of 10 Hz and stroboscopic duty cycle of 14%. A 2.32 × 2.32 mm region of interest is imaged of a reference flat demonstrating a flatness of $<\lambda/4$. Four carrier fringes are introduced over this region to ensure a high contrast ratio and, hence, high data quality. As measurements are taken full field, the contrast ratio is calculated as

$$V = \frac{I_{\max} - I_{\min}}{I_{\max} + I_{\min}} \quad , \tag{5.11}$$

with application of a low pass filter to the raw interferograms to reduce the effects of random noise, where I_{max} and I_{min} are the maximum and minimum interferogram intensity values respectively. From this equation, the contrast is then found to be 87.33 %, indicating an excellent fringe contrast and, consequently, high data quality [Kreis, 2005].

The tilt corrected shape, shown in Fig. 5.7, demonstrates the overall flatness of the reference flat as recovered with sinusoidal modulation.

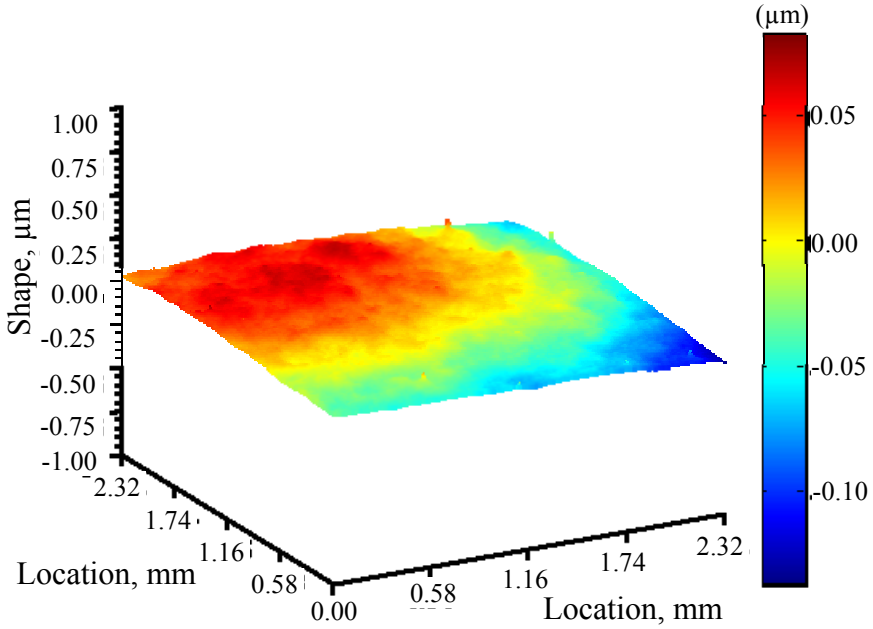

Fig. 5.7. Shape of reference flat recovered with sinusoidal modulation operating at f = 10 Hz and demonstrating a surface flatness of $\lambda/4$.

For comparison, the arithmetic mean of the shape maps recovered with sinusoidal modulation and phase stepping is set to zero. As shown in Table 5.1, the low modulation frequency shape measurements demonstrate an RMS difference of 0.256 nm and similar mean absolute deviations. However, the significant difference between the standard deviation and mean absolute deviation values indicates the presence of multiple outliers in the data set. These outliers may be due to dust particles on the reference flat.

Table 5.1. Shape measurement comparison between sinusoidal modulation and phase stepping.

Sinusoidal modulation	Phase stepping
$\lvert\Delta\langle Z\rangle_{rms}\rvert$ = 0.256 nm	
σ = 18.262 nm	σ = 18.518 nm
|D| = 0.015 nm	|D| = 0.018 nm

To verify the full field correlation of the two methods, a difference map is generated and presented in Fig. 5.8. This difference map is found by subtracting the shape information obtained using phase stepping interferometry from that obtained with sinusoidal phase modulating interferometry.

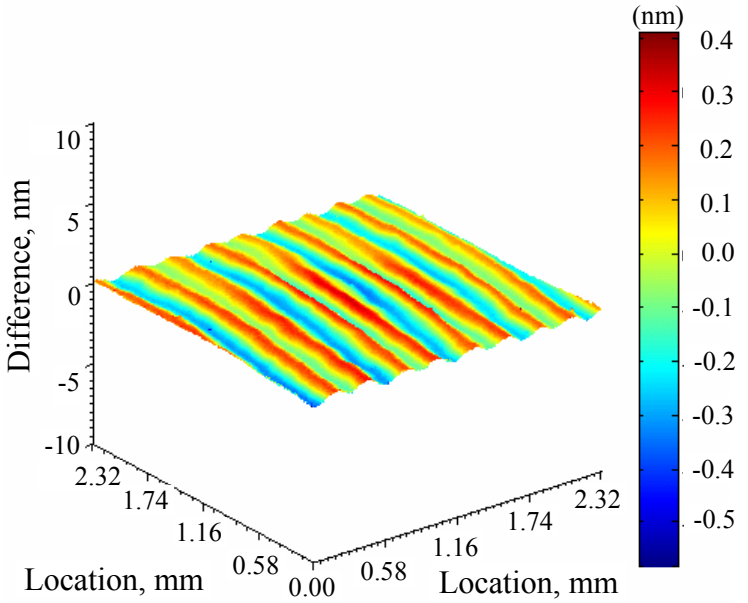

Fig. 5.8. Shape difference map, δ, between sinusoidal modulation and phase stepping. Both measurements performed at the operational frequency of $f = 10$ Hz. The sinusoidal variation, having amplitude of 0.4 nm and frequency of 3.4 cycles/mm, is attributed to a combination of the mean and mean squared errors in both the PMI and PSI systems. These errors are related to the phase modulation parameters and appear with a spatial frequency equal to twice the optical frequency, as explored in Appendix B and Creath [1988; 1992].

From Fig. 5.8., we see that the difference between the shape maps has a full range of ~1 nm with an inter-quartile range of 0.220 nm. As shown, the difference map appears to have a sinusoidal pattern equal to twice the four fringe carrier frequency. This variation is expected based on the effects of additive noise on the recovered shape. As presented in this Thesis in Appendix B, the mean squared error is proportional to twice

the optical frequency. Similarly, errors in phase stepping interferometry have been shown to be similarly proportional to twice the optical frequency [Creath, 1988; Surrel, 1993]. As the difference map is not normally distributed, standard deviation is no longer an appropriate measure of the distribution, however, the mean absolute deviation, |D|, can be found to be 0.134 nm. By calculating the correlation coefficient between the two data maps, the degree of randomness between the acquired shape measurements can be found. Using the Pearson product-moment correlation coefficient, the two shape measurements are found to correlate to 0.9856 and to 0.9956 with removal of data external to the IRQ. This extremely high coefficient demonstrates the equivalency of the shape measurement results between the two interferometric methods at this low modulation frequency. As shown through testing of the optical gauge, the reproducibility of these results applies under modulation frequencies up to 100 Hz and has been demonstrated in the hundreds of Hertz range [Sasaki, et al., 1990b; Dorrio and Fernandez, 1998].

5.3. Environmental stability

It is believed that a four bucket phase modulating interferometer will exhibit greater phase stability than a four bucket phase stepping interferometer implemented on the same device and that this stability will increase with modulation frequency.

As mentioned in Section 3.1, the accuracy of temporal phase stepping interferometry is related to phase modulator errors appearing from hysteresis and overshoot of piezoelectric actuators, random vibrations during constant phase step periods, and high frequency distortions of the modulator [Creath, 1988; Kinnstaetter, et

al., 1988; Surrel, 1993; de Groot, et al., 1996; Dorrio and Fernandez, 1999; Dubois, 2001; Ruiz, et al., 2001]. However, increasing the number of interferograms acquired for phase calculations will decrease the sensitivity of the PSI system to low frequency effects at the cost of increased computing power and processing time [Creath, 1988; Surrel, 1993; de Groot, 1995b; Ruiz, et al., 2001]. With traditional PSI algorithms, it has been shown that the use of a seven-bucket algorithm is several orders of magnitude less sensitive to external, low frequency noise and vibration than a three-bucket algorithm while a four-bucket algorithm provides a 2x to 3x improvement over the three-bucket algorithm, at the cost of minimally larger memory requirements [de Groot, 1995b; Surrel, 1996].

Alternatively, four bucket sinusoidal phase modulating interferometry has been shown to be almost insensitive to external perturbations such as mechanical vibrations at low frequency, compared with the modulation frequency [Sasaki et al, 1990b]. In part, this decreased sensitivity is due to a reduction in hysteresis experienced by a phase modulator during sinusoidal displacement [Physik Instrumente, L.P., 2005]. Additionally, individual interferograms are acquired over multiple modulation periods at constant phase locations on the sinusoidal modulation signal. The result is a linear averaging within each resultant interferogram that leads to a low frequency filtering which serves to reduce transient effects, both environmental and systematic, on the recovered optical phase map [Sasaki et al, 1990a; Agilent Technologies, Inc., 1999; Physik Instrumente, L.P., 2005]. Consequently, it is expected that at lower modulation frequencies the sensitivity of the PMI system to external vibrations will approach that of a phase stepping interferometer operating under similar conditions [Sasaki et al, 1990a].

To experimentally verify the stability of the developed phase modulating interferometer, the mean wrapped phase drift is observed for f = 10 Hz and 100 Hz and compared to results obtained with a four-bucket phase stepping interferometer operating at f = 2 Hz. All experiments are conducted under a stroboscopic duty cycle of 14%. As previously, the displacement rate of the phase modulator is verified with a five-bucket PSI algorithm presented in Hariharan, et al. [1987] and found to be 100.58 nm/V. A reference flat containing five carrier fringes and exhibiting $\lambda/4$ flatness is observed for these trials. Additionally, the interferometer is enclosed to minimize the effects of air turbulence on the results.

Interferogram sets are acquired once every 10s over a 20 minute window where each interferogram has an exposure time of 10 ms. Instantaneous phase is calculated by extracting the value of the wrapped phase map at the points highlighted in Fig. 5.9 and calculating the mean. The phase drift is then taken as the change in this mean between sequential interferogram sets. When the absolute change in this mean value is plotted over the 20 minute interval with the minimum set to zero, the mean phase drift becomes the DC-offset of the data. Phase drift observed during operation of the phase stepping interferometer and the phase modulating interferometer operating at f = 2 Hz and f = 100 Hz, respectively is presented in Fig. 5.10.

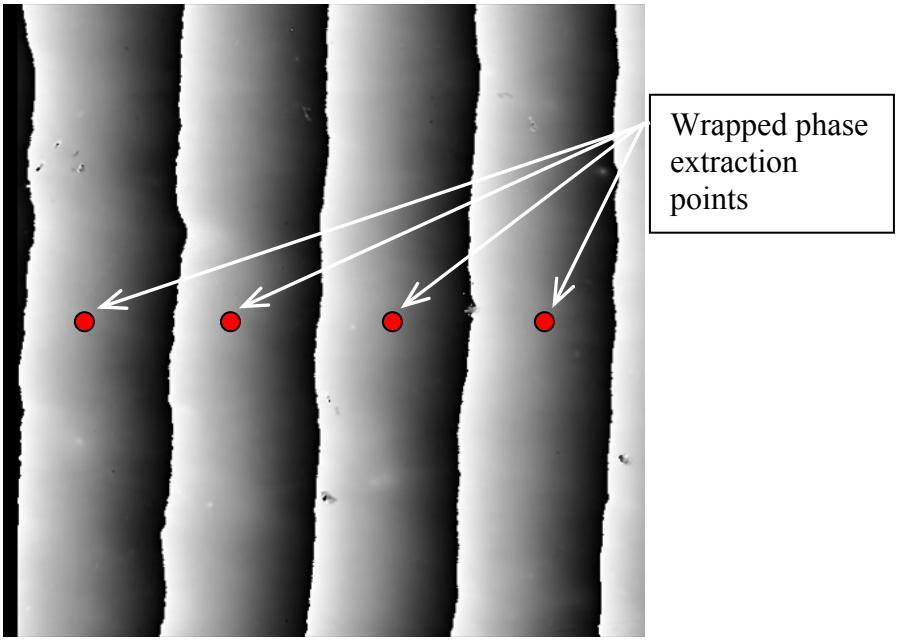

Fig. 5.9. Wrapped phase map generated with sinusoidal modulating interferometry imaging a reference flat at f = 100 Hz and d = 14% showing points used in calculation of optical phase drift

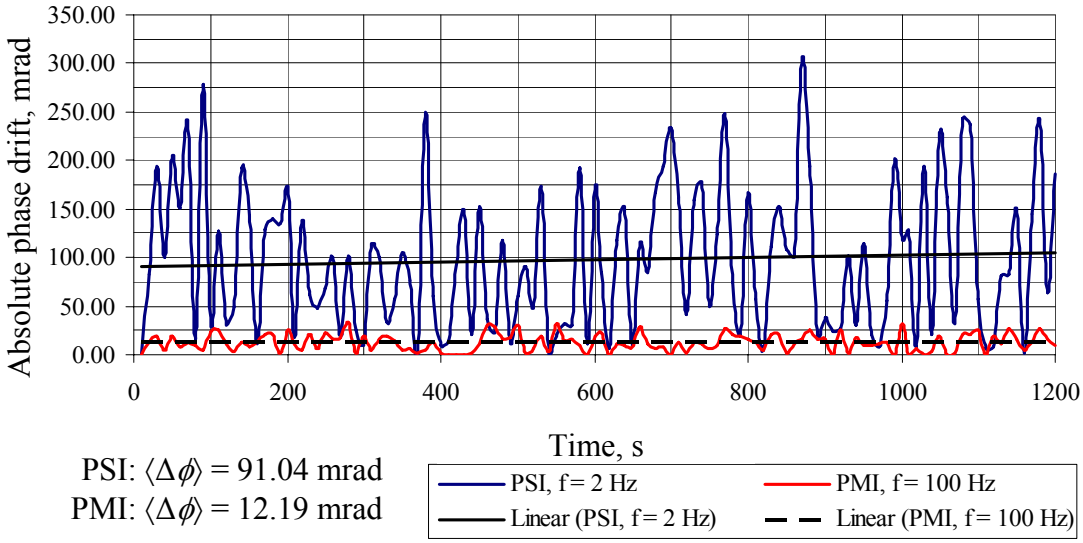

PSI: $\langle \Delta\phi \rangle$ = 91.04 mrad
PMI: $\langle \Delta\phi \rangle$ = 12.19 mrad

Fig. 5.10. Optical phase drift over time recovered with phase stepping interferometry and sinusoidal phase modulating interferometry operating at f = 2 Hz and f = 100 Hz respectively with d = 14%. Under these operating conditions, the PSI method exhibits a mean phase drift 7.5 times that demonstrated with PMI correlating with results presented by Kinnstaetter, et al. [1988] and Sasaki, et al. [1990b].

Table 5.2. Optical phase map drift under phase stepping interferometry at f = 2 Hz and sinusoidal modulating interferometry at f = 10 Hz and 100 Hz.

Phase stepping interferometry, f = 2 Hz	$\langle \Delta\phi \rangle$ = 91.0 mrad	σ = 75.6 mrad
Phase modulating interferometry, f = 10 Hz	$\langle \Delta\phi \rangle$ = 40.1 mrad	σ = 33.3 mrad
Phase modulating interferometry, f = 100 Hz	$\langle \Delta\phi \rangle$ = 12.2 mrad	σ = 8.91 mrad

As seen in Fig. 5.10 and highlighted in Table 5.2, the observed phase drift is greatest in the phase stepping interferometer over the 20 minute test period and is comparable to results presented in Kinnstaetter, et. al [1988]. As predicted, both the mean absolute phase drift and standard deviation decrease in a logarithmic manner with increasing modulation frequency in the phase modulating interferometer due to a decreasing sensitivity to external vibration and modulator errors [Sasaki, 1990a; Dubois, 2001;]. The mean phase drift recovered by the PMI system operating at f = 100 Hz correlates with the 10.1 to 11.6 mrad drifts demonstrated in Sasaki, et al. [1990b] and Dubois [2001] at illumination wavelengths of λ = 760 nm and λ = 545 nm, respectively.

5.4. MEMS application

The shape of and the time variant loading displacement of the prototype μHexFlex device is presented to demonstrate the applicability of the developed phase modulation system with MEMS characterization. The μHexFlex device is being developed under Dr. Martin Culpepper by Mr. Shih-Chi Chen to answer a growing need for low-cost, six-axis, millimeter-scale positioning system for operation in devices including “endoscopic scanners, integrated alignment mechanisms in micro-optic

devices, and positioners that are used in SEMs [Chen and Culpepper, 2006]." As shown in Fig. 5.11, the μHexFlex consists of a central stage, ranging from 280 μm to 540 μm in diameter in the studied devices, attached to the surrounding substrate via an amplification flexure and micro-scale thermomechanical actuators (TMAs), Fig. 5.12. These TMAs provide in- and out of-plane actuator displacements that, in combination, cause displacement in one to six axes through the creation and control of thermomechanical stresses between structural silicon layers separated by an insulating silicon dioxide layer [Chen and Culpepper, 2006].

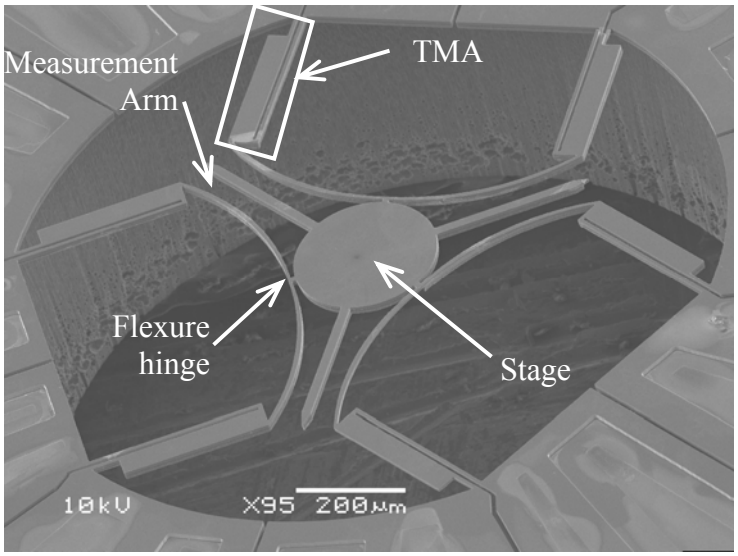

Fig. 5.11. Scanning electron microscopy image of a prototype μHexFlex device [courtesy of: Shih-Chi Chen, MIT].

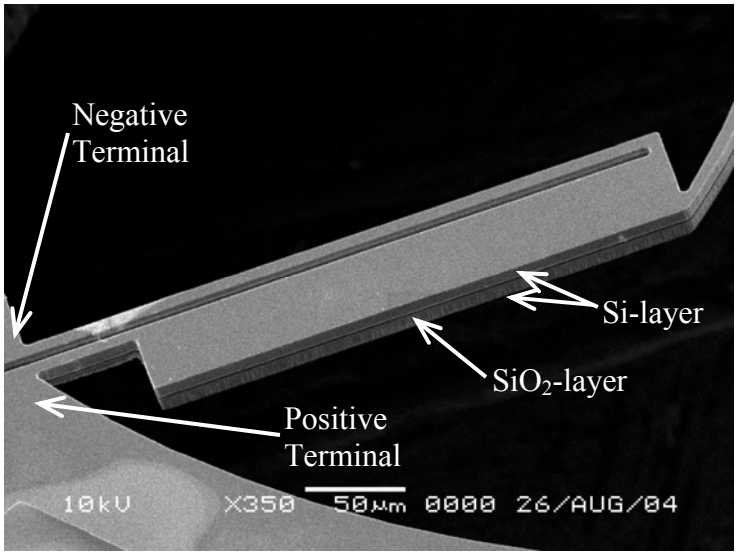

Fig. 5.12. Layered TMA structure of µHexFlex device viewed through a scanning electron microscope [courtesy of: Shih-Chi Chen, MIT].

While these devices are currently in the prototype stage, the research objective is the creation of on-site positioning within enclosed spaces. Previous testing has found the µHexFlex to have a nominal displacement resolution of 1 Å/mV with a standard deviation of 8 nm due to uncertainties in the thermal materials and actuation control [Chen and Culpepper, 2006]. Currently, a need exists for full-field shape characterization and bidirectional quasi-static displacement testing for further characterization and system development.

5.4.1. Shape measurement

Shape measurement of the µHexFlex device was conducted with both phase modulating and phase stepping interferometry. Both the PMI and PSI system have been implemented and characterized on the same Linnik interferometer with controls from the LabVIEW™ programming environment under functionally identical interfaces. Due to

the stage of development, multiple sizes of the μHexFlex device were available for study. However prior to testing, all samples had previously been subjected to thermal loading until failure and were believed to contain distortions outside of their operating parameters.

For data comparison, shape measurements were recorded using both interferometric methods on the 540 μm diameter μHexFlex device to maximize the number of pixels imaging the central stage. At this size and magnification, the central stage could not be imaged with all substrate connections. Consequently, this device was placed so that the central stage and 2 of the 6 TMAs could be interferometrically imaged. As with the system qualifications carried out in Section 5.1 to 5.3, measurements were carried out using a 4x magnification with a CMOS camera containing 1280 × 1024 active pixels at 8-bit digitization with a region of interest. All tests were conducted at a 1000 × 1000 pixel ROI centered on the imaging array. Measurements taken require:

1) performing high-resolution phase modulation calibration verifying the displacement rate of 100.58 nm/V [Hariharan et al., 1987],
2) optimizing the beam ratio between the reference and objective arms to maximize the fringe contrast,
3) adjustment of the interferometric and focal planes to maximize contrast over the entire device,
4) removal of any carrier fringes from the substrate,
5) adjustment of operation properties within developed control system,
    a) wavelength: 620 nm,

b) modulation frequency: 100 Hz (PMI), 2 Hz (PSI),

c) stroboscopic amplitude: 1.25 V,

d) illumination duty cycle: 10%,

e) trigger mode: Low Integrate,

f) trigger polarity: Positive (PMI) / Negative (PSI).

As shown in Figs 5.13 and 5.14, the small and medium sized µHexFlex devices exhibit a severe tilt and displacement relative to their surrounding substrate. The smaller device exhibits a 1.1 µm positive displacement of its 280 µm diameter central stage from the surrounding substrate.

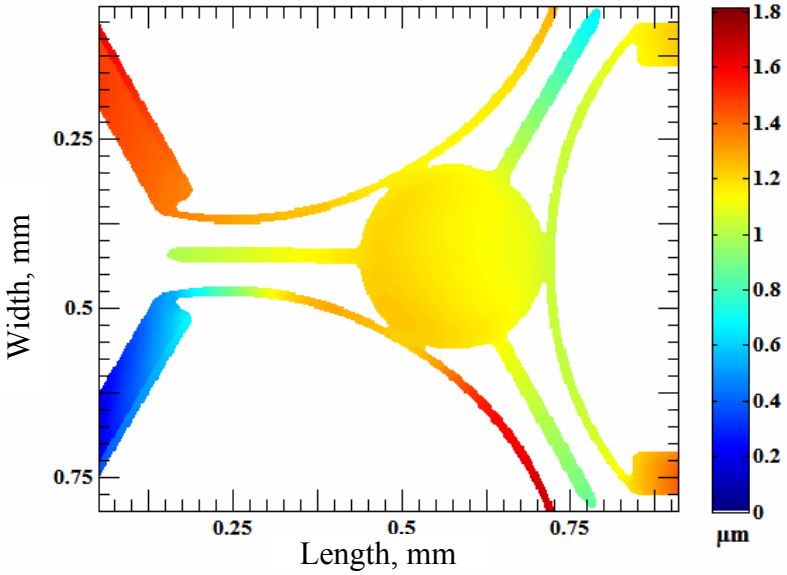

Fig. 5.13. Recovered shape of 280 µm diameter central stage µHexFlex.

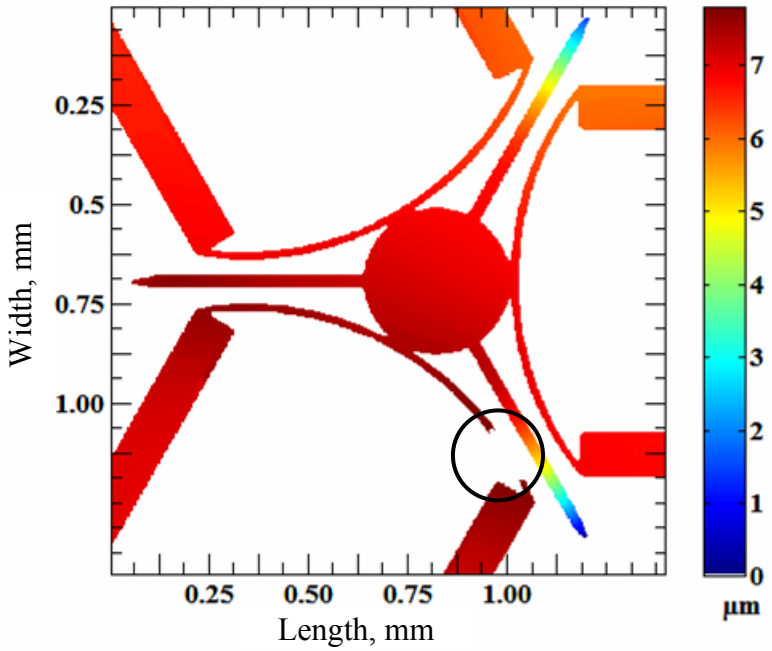

Fig. 5.14. Recovered shape of 375 µm diameter central stage µHexFlex demonstrating damage to the armature structure.

As with the smaller device, the medium sized µHexFlex device exhibits a displacement with respect to the surrounding substrate. In this larger device, this displacement is found to be 7.4 µm with respect to the 375 µm central stage. It is believed that this larger displacement is partially due to the broken area indicated in Fig. 5.14. Within this area, little to no structure was observed, indicating that it had broken away from the connected armature, perhaps during testing, causing this device to fail. It should be noted that the measurement arms, used in other displacement characterizations, radiating from the central stage exhibit non-uniform shapes [Chen and Culpepper, 2006]. This non-uniformity is believed due to residual stresses during the fabrication of these components. As these arms are non-functional, no planar tolerances were enforced during prior qualification. However, this, up to, 6 µm curvature may be used in future work investigating the residual stresses within these µHexFlex devices.

Figures 5.15 and 5.16 depict the recovered shape of the largest µHexFlex device, containing a central stage of 540 µm in diameter, using phase modulating and phase stepping techniques, respectively. As with the smaller devices, this sample had previously undergone testing to failure. Unlike the prior examples, failure in this device involved breakage of both a flexure arm and multiple TMA structures, as indicated in Fig 5.15. However, this device exhibited less distortion, otherwise, than the other two devices compared to the nominally planar structure.

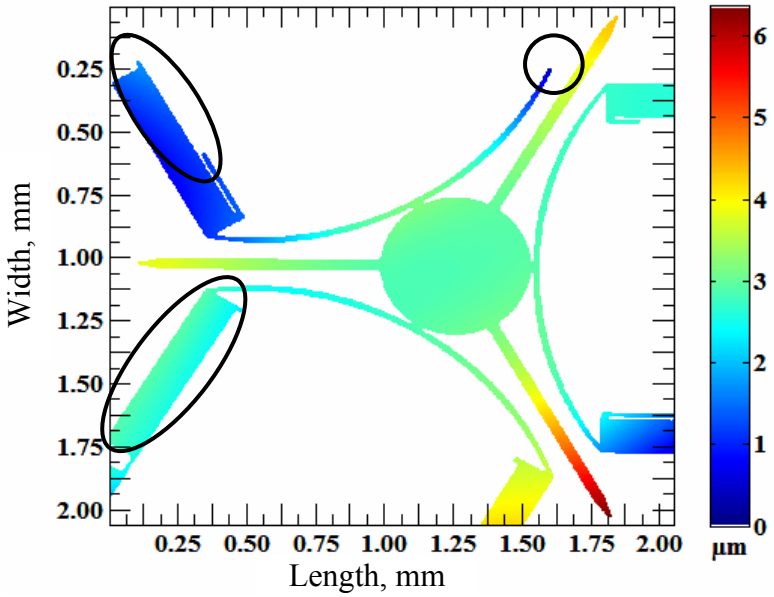

Fig. 5.15. Recovered shape of 540 µm diameter central stage µHexFlex using phase modulating interferometry with damage indicated to the TMA and armature structures.

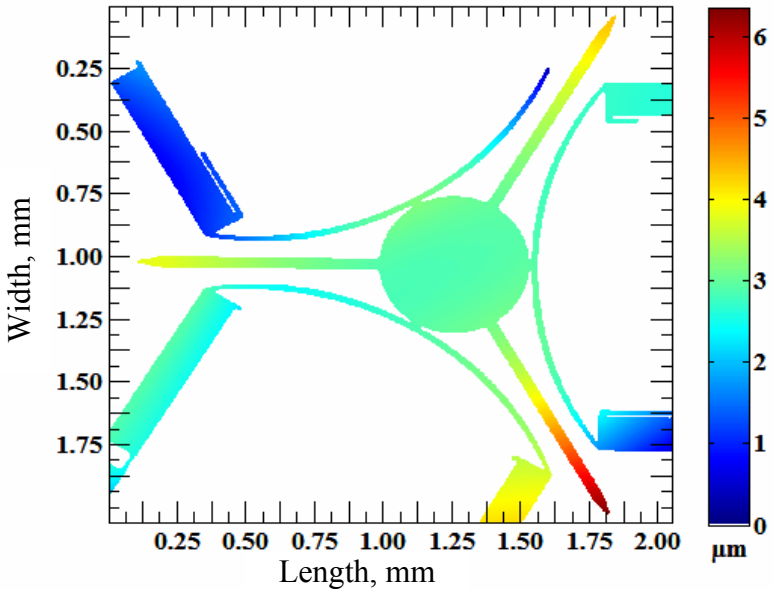

Fig. 5.16. Recovered shape of 540 µm diameter central stage µHexFlex using phase stepping interferometry.

As before, a displacement exists between the central stage and surrounding substrate of 2.1 µm, although this is 3x less than that demonstrated by the medium sized µHexFlex device. The central stage of this device was found to be flat to within σ = 10 nm after removal of all tilt effects. A difference analysis was conducted to compare the recovered shape maps obtained with the PSI and PMI systems. As with the analysis presented in Section 5.2, this involved the subtraction of the shape measurements obtained with PSI from those obtained with PMI. The difference map was then found to have an IQR of 0.201 nm, σ = 0.305 nm and |D| = 0.048 nm. These results readily compare to the comparative results obtained during prior characterization of these systems, further indicating the reliability of the acquired data set.

5.4.2. Quasi-static testing

To further demonstrate the applicability of phase modulating interferometry, quasi-static analysis was conducted on a 375 μm central stage μHexFlex device. Mr. Chen, the lead μHexFlex researcher, had expressed interest in the use of this system for bi-directional measurements as prior testing had been limited to unidirectional studies [Chen and Culpepper, 2006]. Unlike the previously tested devices, the μHexFlex device tested suffered thermomechanical damage to five of the six TMA structures until failure of those TMAs. However, the substrate and device itself remained intact and therefore, potentially available for an additional time variant loading experiment. However, it was unclear what displacement characteristics the device would exhibit due to a lack of prior testing on devices exhibiting this degree of experimental damage.

The interferometric system was configured for operation as with the static tests under a modulation frequency of 100 Hz. The μHexFlex was powered by an HP E36118, voltage limited to 20 VDC, the nominal safe voltage limit for the system. Due to the limited resolution of the power supply, 6 current amplitudes were investigated as indicated in Table 5.3 while allowing the voltage to rise as needed.

Table 5.3. μHexFlex quasi-static loading conditions.

Step, #	Applied Voltage, V	Applied Current, A
1	5.7	0.03
2	7.5	0.05
3	9.6	0.08
4	11.7	0.10
5	13.4	0.11
6	14.0	0.12

Instantaneous shape was recovered at each data point for later analysis with the displacement of the central stage measured relative to the base substrate connected to the active TMA, as shown in Fig. 5.17.

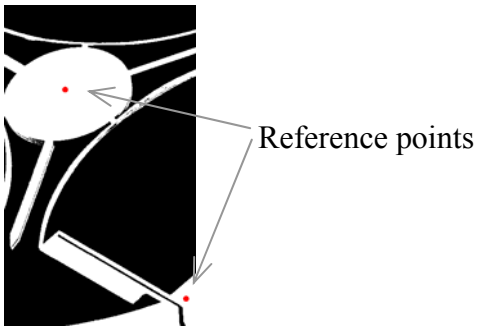

Fig. 5.17. Relative displacement points on central stage and substrate connection of active TMA.

The relative displacement of the central stage was then plotted to determine a displacement/voltage relationship. As shown in Fig. 5.18, the recovered displacements are near linear with respect to applied voltage with a characteristic resolution of 0.75 Å/mV. The nominal displacement behavior of 1.0 Å/mV is also shown for comparison [Chen and Culpepper, 2006].

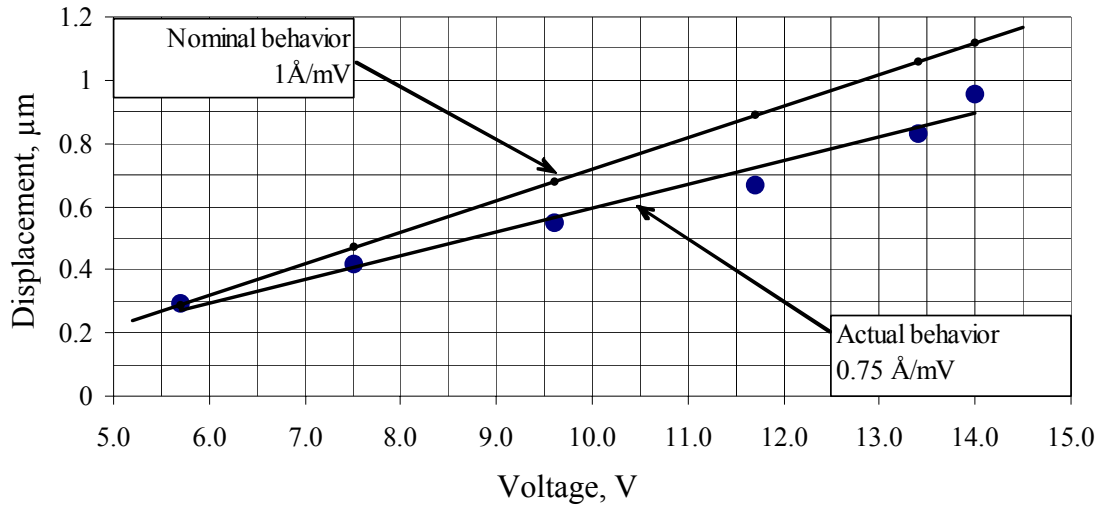

Fig. 5.18. Displacement of the damaged µHexFlex device versus applied voltage as determined through the system developed in this Thesis.

As seen in Fig. 5.18, the actual displacement of the µHexFlex device is 25% below nominal and mean deviation from the trend line of 27.1 nm. Given the construction of the µHexFlex device, it is expected that some of these deviations from ideal are due to unmeasured in-plane displacements of the central stage. According to materials published in Chen and Culpepper [2006] when only the one half of a TMA device is functional, the central stage will undergo both in-plane and out-of-plane motions. The combination of these motions are used to determine the full displacement vector of the central stage and hence its nominal displacement characteristics.

6. CONCLUSIONS AND FUTURE WORK

This Thesis has demonstrated the feasibility of phase modulating interferometry as an alternative to phase stepping and phase-shifting interferometric techniques through comparison of measurement resolution and environmental stability under multiple operating conditions. It has also included the characterization of shape and displacement for a MEMS device.

The objectives of this work were:

1) the derivation of stroboscopically illuminated phase modulating interferometry for use in MEMS characterization,
2) the subsequent development of and implementation of a software package for this technique,
3) the determination of both the spatial and measurement resolutions of the realized system,
4) the application of phase modulating interferometry for characterization of an actual MEMS components, and
5) the verification of those results through the use of a traditional phase stepping interferometer.

The phase modulating interferometry presented in this work serves as an expansion to the techniques presented by Sasaki and Okazaki [1986a, 1987] and Dubois [2001] through the incorporation of stroboscopic illumination for dynamic testing. This inclusion requires the optimization of the phase modulating parameters, both in amplitude and phase relative to the duty cycle of the illumination signal. The derived highly non-linear relationship between these parameters coupled with the synchronization needs

between the modulation, illumination and acquisition cycles requires the development of a complex control system with highly accurate calibration of the modulation source. This calibration is accomplished through procedures presented in Hariharan, et al. [1987].

The LabVIEW™ programming environment was chosen for the software development due to its parallel processing capabilities and flexibility in the control of both an imaging system and multi-channel output cards. This Thesis has required the development of two software packages to meet the objectives indicated above. The first package operates the phase modulating interferometer under stroboscopic illumination while the second implements a phase stepping algorithm, again under stroboscopic illumination. The resultant packages are functionally identical for the operator to minimize transition between the two systems. Both systems operate at several frames per second during calculation of the wrapped optical phase where the frame rate is limited by the generation time of the output voltage signals to ensure the generation of a high quality, low distortion modulation function.

With the developed control system, the Linnik configured interferometer demonstrates a spatial resolution of 2.762 μm over a 2.967 × 2.373 mm field of view using a 1280 × 1024 CMOS array camera and 4x magnification objectives. The measurement resolution of the phase modulating interferometer has been qualified on a NIST traceable 500 Å ± 2.5% thick gold film structure. Through the use of a difference analysis relative to a flat plane, the recorded data cloud indicates a film thickness of 503 Å ± 7 Å which lies within the design tolerance of the investigated sample when operating at a reference modulation frequency of 100 Hz. Similar results are obtainable through the use of phase stepping techniques [Furlong, 2007]. The reproducibility of the shape

measurement data has been shown in comparison to phase stepping interferometry under both low and high frequency sinusoidal modulation.

The qualified system has been applied for both shape measurements and quasi-static testing of the μHexFlex device under a 100 Hz modulation frequency. Due to its prototype development stage, multiple configurations were available for shape measurements with the medium sized system configured for single axis testing. All samples tested had been previously cycled to failure and suffered distortions from their nominal planar configuration. Tilt and deformation from the substrate material ranged from 1.7 μm on the smaller devices to 7.4 μm on the moderately sized systems. To verify the reliability of these results, the largest μHexFlex device was qualified on both the phase stepping and the phase modulating systems and found to have a IQR of 0.201 nm, $\sigma = 0.305$ nm and $|D| = 0.048$ nm between the two techniques, further indicating the reproducibility of the results obtained through phase modulating interferometry.

Quasi-static testing was conducted with a damaged μHexFlex to qualify its out-of-plane motion relative to the system normal. As presented, the damaged device provided a linear displacement of 0.75 Å/mV with a mean experimental deviation of 27.1 nm compared to nominal motion of 1.00 Å/mV and standard deviation of 8 nm. Based on an interview with the developer, Mr. Chen, this difference is within the expected variation of the device under these conditions.

For future works, this Thesis research could be further extended with the following list of tasks:

1) determination of a closed form solution which describes the equivalency between the phase constant equations. This closed form solution would allow for a global optimization of the phase modulating parameters without the use of the power series limits set in this Thesis and the required iterative solver. Removal of the iterative solver will allow for calculation of the modulation parameters automatically under arbitrary stroboscopic illumination duty cycles without the need for interpolation as currently implemented in the software control package,
2) reduction in the software processing time through the use of an external signal generator. As developed, approximately 90% of the program cycle time is used in calculation of the analog voltage output signals. Consequently, the control of an external voltage output device will immediately increase the operational speed of the developed coding, leading to higher processed frame rates,
3) further error qualification of the developed system, particularly focused on comparisons to phase stepping interferometry. It is expected that this work will quantitatively highlight the improvements of phase modulating interferometry over phase stepping interferometry in dynamic motion studies and in its relative immunity to environmental disturbances,
4) the addition of multiple illumination sources for measurement of larger shape variations in both the implemented and other interferometric systems,

5) development of a portable control system for use with additional imaging systems and phase modulators.

The above tasks seek to increase the portability and functionality of the phase modulating interferometer system for use in rapid static and modal MEMS characterization.

7. REFERENCES

4D Technology, Inc., *www.4dtechnology.com/*, last viewed: Sept 7, 2006.

Abramowitz, M. and Stegun, I.A., *Handbook of mathematical functions with formulas, graphs, and mathematical tables*, National Bureau of Standards, Dover Publications, Washington, D.C., 1970.

Agilent Technologies, Inc., *Fundamentals of signal analysis*, Application note: 243, Agilent Technologies, Inc., 1999.

ATIS telecom glossary 2000, ATIS Committee T1A1, prep., *www.atis.org/tg2k*, American National Standards Institute, Inc., 2000, last viewed: Sept. 7, 2006.

Bitter, R., Mohiuddin, T., and Nawrocki, M., *LabVIEW™ advanced programming technique*, CRC Press, NY, 2000.

Boresi, A.P., and Sidebottom, O.M., *Advanced mechanics of materials*, Wiley, NY, 1985.

Caber, P., "Interferometric profiler for rough surfaces," *Appl. Opt.*, 32(19): 3438- 3441, 1993.

Chapman, M., "Heterodyne and homodyne interferometry," Renishaw Group, *www.renishaw.com*, 2002.

Chen, S. and Culpepper, M., "Design of a six-axis micro-scale nanopositioned - μHexFlex," *Prec. Eng.*, 30: 314-324, 2006.

Cohen, J., *Statistical power analysis for the behavioral sciences*, 2nd ed., Hillsdale, NJ: Lawrence Erlbaum Associates, 1988.

Creath, K., "Phase-measurements interferometry techniques," in *Progress in Optics*, Wolf, E., ed., Elsevier Science, NY, 26: 349–393, 1988.

Creath, K., “Phase measurement interferometry: beware these errors,” *Proc. SPIE*, 1553: 213-220, 1992.

Deck, L., “Fourier-transform phase-shifting interferometry,” *Appl. Opt.*, 42(13):2354-2365, 2003.

de Groot, P., “Derivation of algorithms for phase-shifting interferometry using the concept of a data-sampling window,” *Appl. Opt.*, 34: 4723-4730, 1995a.

de Groot, P., “Vibration in phase-shifting interferometry,” *JOSA*, 12(2): 354-365, 1995b

de Groot, P., and Deck, L., “Numerical simulations of vibration in phase-shifting interferometry,” *Appl. Opt.*, 35: 2172-2178, 1996.

de Groot, P., de Lega, X., Kramer, J., and Turzhitsky, M., “Determination of fringe order in white-light interference microscopy,” *Appl. Opt.*, 41(22): 4571-4578, 2002.

Dorrio, B. and Fernandez, J., “Phase-evaluation methods in whole-field optical measurement techniques,” *Meas. Sci. Technol.*, 10:R33-R55, 1998.

Douglass, M., “Lifetime estimates and unique failure mechanisms of the DigitalMicromirror Device (DMD),” *Proc. IEEE*, 36173:9-16, 1998.

Dubois, A., Boccara, A. C., and Lebec, M., ‘‘Real-time reflectivity and topography imagery of depth-resolved microscopic surfaces,’’ *Opt. Lett.*, 24: 309-311, 1999.

Dubois, A., “Phase-map measurements by interferometry with sinusoidal phase modulation and four integrating buckets,” *JOSA-A*, 18: 1972-1979, 2001.

Dyson, J., *Interferometry as a measuring tool*, Machinery Publishing Co., Brighton, Sussex, England, 1970.

Edmund Optics, Inc., *Edmund Optics specification sheet: USAF-1951 target*, Edmund Optics, Inc., Barrington, NY, 2006.

Electronic Design, *MEMS raise testing issues from the beginning to the end of the design cycle*, *Electronic Design,* 2000.

Exponent, Inc., *www.exponent.com*, 2000, last viewed: Apr. 15, 2006.

Furlong, C., and Pryputniewicz, R. J., "Optoelectronic characterization of shape and deformation of MEMS accelerometers used in transportation applications," *Opt. Eng.*, 42(5): 1223-1231, 2003.

Furlong, C., *Microelectromechanical systems: introduction and applications*, ISTFA, Boston, 2004a.

Furlong, C., and Pryputniewicz, R. J., "Study and characterization of a MEMS micromirror device," *Proc. SPIE,* 5531:54-63, 2004b.

Furlong, C., "Optoelectronic holography for testing electronic packaging and MEMS," in *Optical Inspection of Microsystems*, Osten, W., ed., CRC Press, NY, 2007.

Gitterman, M, "Simple treatment of correlated multiplicative and additive noises," *J. Phys. A: Math. & General.*, 32(27): 293-297, 1999.

Glynn, E., "USAF and microscopy resolution test charts and pixel profiles," online, last updated: 2002.

Gorard, S., "Revisiting a 90-year-old debate: the advantages of the mean deviation," Manchester, UK: British Educational Research Association Annual Conference, presented: 2004.

Greivenkamp, J. E., and Bruning, J. H., ''Phase-shifting interferometers,'' in *Optical Shop Testing*, 2nd ed., Malacara, D., ed., 14: 501–598, Wiley, NY, 1992.

Guckel, H., Randazzo, T., and Burns, D.W., "A simple technique for the determination of mechanical strain in thin films with applications to polysilicon," *J. Appl. Phys.*, 57(5): 1671-1675, 1985.

Haasteren, A., and Frankena, H., "Real-time displacement measurement using a multicamera phase-stepping speckle interferometer," *Appl. Opt.*, 33(19): 4137-4142, 1994.

Haddad W., McNulty, I., Trebes, J., and Anderson, E., "Ultrahigh resolution x-ray tomography," in *Nondestructive Evaluation: Theory, Techniques, and Applications*, Shull, P., ed., Marcel Dekker, NY, 2002.

Hariharan, P., Oreb, B.F., Eiju, T., "Digital phase-shifting interferometry: a simple error-compensating phase calculation algorithm", *Appl. Opt.*, 26(13): 2504-2506, 1987.

Hsu, T. R., *MEMS & Microsystem Design and Manufacture*, McGraw-Hill, NY, 2002.

Judy, J. W., "Microelectromechanical systems (MEMS): fabrication, design, and applications," *Smart Mater. Struct,* 10: 1115-1134, 2001.

Kinnstaetter, K., Lohmann, A., Schwider, J., and Streibl, N., "Accuracy of phase-shifting interferometry," *Appl. Opt.* 27: 5082–5089, 1988.

Koliopoulos, C., "Simultaneous phase-shift interferometer," *Proc. SPIE*, 1531: 119-127, 1992.

Krauss, O., "Micro Machining," *Colorado Engineer Magazine*, *cem.colorado.edu*, 2002.

Kreis, T., *Handbook of holographic interferometry*, Wiley-VCH, Weinheim, Germany, 2005.

Kuppers, J., Gouverneur, I., Rodgers, M., Wenger, J., and Furlong, C., "Dynamic characterization of AFM probes by laser Doppler vibrometry and stroboscopic holographic methodologies," *Proc. SPIE*, 6293: 57-68, 2006.

Kwon, O., Shough, D., and Willians, R., "Stroboscopic phase-shifting interferometry," *Opt. Lett.*, 12: 855–857, 1987.

LabVIEW™ 7.1, National Instruments, Inc., Austin, TX, 2006.

Liwei, L., Pisano, A.P., and Howe, T.R., "A micro strain gauge with mechanical amplifier," *JMEMS*, 6(4): 313-321, 1997.

Luth W, "Isolation of Moving Objects in Digital Image Sequences," *Academy of Sciences of the GDR*, Dresden, Germany, 1989.

Mann, C., Lingfeng, Y., Chun-Min, L, and Myung, K., "High resolution quantitative phase contrast microscopy by digital holography," *Opt. Exp.*, 13(22): 8693-8698, 2005.

Mathcad r.12, Mathsoft Engineering & Education, Inc., Needham, MA, 2004.

MatLab 7.3, The Mathworks, Natick, MA, 2006.

MEMS Industry Group, "Industry in transition: 2006 MEMS forecast, an," The MEMS Industry Group, In-Stat, *www.memsindustrygroup.com*, 2006.

MEMS and Nanotechnology Exchange, *www.mems-exchange.org*, last viewed: Nov. 19, 2006.

Metrix, Inc., *Imageware Surfacer*, Metrix, Inc., Montreal, Quebec, 2006.

Montgomery, D., *Applied statistics and probability for engineers*, 3rd ed., Wiley, New York, NY, 2003.

National Instruments, *Specification sheet: PCI-6713*, National Instruments, Inc., Austin, TX, 2006.

North-Morris, M., VanDelden, J., and Wyant J., "Phase-shifting birefringent scatterplate interferometer," *Appl. Opt.*, 41: 668-677, 2002.

Osterberg, P.M. and Senturia, S.D., "M-TEST: a test chip for MEMS material property measurement using electrostatically actuated test structures," *JMEMS,* 6(2):107-118, 1997.

Opto Diode Corporation, *Photodiode specification sheet: OD-620L*, Opto Diode Corporation, *www.optodiode.com*, last viewed: Nov. 15, 2006.

Physik Instrumente, L.P., *Designing with piezoelectric transducers: nanopositioning fundamentals*, Physik Instrumente, L.P., Irvine, CA, 2005.

PixeLINK, Inc., *User Manual: PixeLINK PL-A741*, PixeLINK, Inc., Ottawa, ON, Canada, 2006.

Pryputniewicz, R. J., *MEMS SUMMiT™ technology*, Worcester Polytechnic Institute, Mechanical Engineering Department, Worcester, MA, 2005.

RadioShack®, RadioShack Corporation, Fort Worth, TX, 2006.

Rai-Choudhury, P., ed., *MEMS and MOEMS technology and application*, SPIE Press, Bellingham, WA, 2000.

Ruiz, P., Huntley, J., Shen, Y., Coggrave, C., and Kaufmann, G., "Vibration-induced phase errors in high speed phase-shifting speckle pattern interferometry," *Appl. Opt.*, 40(13): 2117-2125, 2001.

Sandia National Laboratories, *www.sandia.gov*, last viewed: Nov 19, 2006.

Sasaki, O., and Okazaki, H., "Sinusoidal phase modulating interferometry for surface profile measurement," *Appl. Opt.*, 25:3137-3140, 1986a.

Sasaki, O., and Okazaki, H., "Analysis of measurement accuracy in sinusoidal phase modulating interferometry," *Appl. Opt.*, 25:3125-3158, 1986b.

Sasaki, O., Okazaki, H., and Sakai, M., "Sinusoidal phase modulating interferometer using the integrating bucket method," *Appl. Opt.*, 26: 1089-1093, 1987.

Sasaki, O., Takahashi, K., and Suzuki, T., "Sinusoidal phase modulating laser interferometer with a feedback control system to eliminate external disturbance," *Opt. Eng.*, 29: 1511–1515, 1990a.

Sasaki, O., Okamura, T., and Nakamura, T., "Sinusoidal phase modulating Fizeau interferometer," *Appl. Opt.*, 29: 512-515, 1990b.

Schmit, J., and Creath, K., "Window function influence on phase error in phase-shifting algorithms," *Appl. Opt.*, 35(28): 5642-5649, 1996.

Schwider, J., "Advanced evaluation techniques in interferometry,", in *Progress in Optics*, Wolf, E., ed., Elsevier Science, NY, 28: 271–359, 1990.

Shull, P., ed., *Nondestructive evaluation: theory, techniques, and applications*, Marcel Dekker, Inc., NY, 2002.

Sirohi, R. S., and Kothiyal, M. P., ''Heterodyne and phase-shifting interferometry,'' in *Optical Components, Systems, and Measurement Techniques*, Sirohi, R.S. and Kothiyal, M.P., eds., Marcel Dekker, NY, 1991.

Surrel, Y., "Phase Stepping: a new self-calibrating algorithm," *Appl. Opt.*, 32(19): 3598-3600, 1993.

Surrel, Y., "Design of algorithms for phase measurements by the use of phase stepping," *Appl. Opt.*, 35(1): 51-60, 1996.

Suzuki, T., Sasaki, O., Kaneda, J., Maruyama, T., "Real-time two dimensional surface profile measurement in a sinusoidal phase-modulating laser diode interferometer," *Opt. Eng.* 33(8): 2754-2759, 1994.

Takeda M., Ina, H., and Kobayashi, S., "Fourier-transform method of fringe-pattern analysis for computer-based topography and interferometry," *JOSA,* 72(1): 156- 160, 1982.

Thor Labs, *Laser diode combination controller user's manual: ITC502*, Thor Labs, Newton, NJ, 2006.

Tonner, P., and Stanley, J., "Supervoltage Computed Tomography for Large Aerospace Structures," in *Nondestructive Evaluation: Theory, Techniques, and Applications*, Shull, P., ed., Marcel Dekker, NY, 2002.

Van Arsdell, W.W., and Brown, S.B., "Subcritical crack growth in silicon MEMS," *JMEMS*, 8(3): 319-327**,** 1999.

Veeco Metrology Group, *Sloan DekTek calibration standards set*, Veeco Instruments, Inc, Tucson, AZ, 2002.

Wyant, J. C., ''Use of an ac heterodyne lateral shear interferometer with real-time wavefront correction systems,'' *Appl. Opt.* 14(11): 2622–2626, 1975.

Wyant, J. C., "White Light Interferometry," *Proc. SPIE*, 2002.

Zhang H., *Introduction to MEMS*, Lecture Notes, Institute of Microelectronics, *ime.pku.edu.cn*, Peking University, Peking, China, 2004.

Zygo Corporation, *www.zygo.com/*, last viewed: December, 2006.

APPENDIX A. Integration of instantaneous intensity function

As presented in Section 3, the instantaneous intensity of the optical map can be described by

$$I(t) = I_B(t) + I_M(t) \cdot \cos\left[\phi + \psi \sin(\omega \cdot t + \theta)\right] \ , \tag{A.1}$$

removing all spatial dependence terms for simplicity. The derived equation cannot be directly integrated over the acquisition time of the imaging array due to the nested sine function. By first extracting the additive terms through the trigonometric identity

$$\cos(X - Y) = \cos(X)\cos(Y) + \sin(X)\sin(Y) \ , \tag{A.2}$$

the nested sinusoid term can be treated independently. Application of Eq. A.2, results in a new form of the instantaneous intensity function of the form,

$$I(t) = I_B(t) + I_M(t) \cdot \left\{ \begin{matrix} \cos(\phi)\cos\left[\psi \sin(\omega \cdot t + \theta)\right] \\ -\sin(\phi)\sin\left[\psi \sin(\omega \cdot t + \theta)\right] \end{matrix} \right\} \ . \tag{A.3}$$

Through this new representation, the additive terms can be treated independently. According to Abramowitz and Stegun [1970], a sine function nested within either a cosine or sine function can be replaced with an infinite power series, index *m*, consisting of Bessel functions of the First Kind multiplied with a cosine or sine term respectively. As seen in Eq. A.4,

$$\cos\left[X\sin(Y)\right] = J_0(X) + 2\sum_{m=1}^{\infty}\left[J_{2m}(X)\cos(2k\cdot Y)\right] \ ,$$

and

$$\sin\left[X\sin(Y)\right] = -2\sum_{m=0}^{\infty}\left\{J_{2m+1}(X)\sin\left[(2k+1)\cdot Y\right]\right\} \ , \tag{A.4}$$

these identities can be applied to Eq. A.1 and so create an integratable, instantaneous intensity function, as seen in Eq. A.5,

$$\begin{aligned} I(t) &= I_B(t) + I_M(t)\cos(\phi)J_0(\psi) \\ &+ 2I_M(t)\cos(\phi)\left(\sum_{m=1}^{\infty}\left\{J_{2m}(\psi)\cos\left[2m(\omega\cdot t+\theta)\right]\right\}\right) \\ &+ 2I_M(t)\sin(\phi)\left(\sum_{m=0}^{\infty}\left\{J_{2m+1}(\psi)\sin\left[(2m+1)(\omega\cdot t+\theta)\right]\right\}\right) \ . \end{aligned} \tag{A.5}$$

To determine the intensity recovered by the imaging array, the resultant time variant equation must be integrated over the acquisition period of the imaging array. For a stroboscopically illuminated system, the acquisition period is defined as a percentage of the modulation cycle. The integration length, Δt, is then the period of the modulation signal multiplied by the illumination duty cycle, d. To determine the location of this acquisition window in time, the center is defined to be at the quadrature points of the sinusoidal modulation signal where p defines the frame number, 1,2,3, or 4,

$$\frac{p\cdot T}{4} \ . \tag{A.6}$$

Consequently, the limits of integration for the time variant function are

$$I_p = \frac{1}{\Delta t} \cdot \int_{\frac{pT}{4}-\frac{\Delta t}{2}}^{\frac{pT}{4}+\frac{\Delta t}{2}} I(t)dt \quad . \tag{A.7}$$

The first two terms within the time variant intensity function will be integrated to the average background and modulation intensities recovered over the acquisition period. However, integration with respect to time requires that the power series converges and is continuous over for a constant value of time. As both the sinusoidal and Bessel functions are continuous their multiplication will provide a continuous function for any value of time. Consequently, both additive terms can be integrated with respect to time. For simplification, the instantaneous modulated intensity is assumed constant over time to remove its time dependence within the integral. This can be assumed if the coherence length of the illumination source is large relative to the modulation amplitude resulting in a spatially constant fringe contrast. This assumption can be validated after calculation of modulation amplitude.

Integration is carried out by hand and verified through MathCAD® [2004]. The resultant, recovered intensity map is then found to be

$$
\begin{aligned}
I_p = {} & \bar{I}_B + \bar{I}_M \cos(\phi) J_0(\psi) \\
& + \frac{2\bar{I}_M T}{\pi} \cos(\phi) \left\{ \sum_{m=1}^{\infty} \left[\begin{array}{l} (-1)^{m \cdot p} \, \frac{J_{2m}(\psi)}{2m} \cdot \\ \cos(2m\theta) \cdot \sin(m \cdot 2\pi d) \end{array} \right] \right\} \\
& + \frac{2\bar{I}_M T}{\pi} \sin(\phi) \left(\sum_{m=0}^{\infty} \left\{ \begin{array}{l} \frac{J_{2m+1}(\psi)}{2m+1} \cdot \\ \sin\left[(2m+1) \left(\frac{p\pi}{2} + \theta \right) \right] \sin\left[(2m+1) \cdot 2\pi d \right] \end{array} \right\} \right)
\end{aligned}
\qquad \text{(A.8)}
$$

Equation A.8 is similar in form to the results produced in Dubois [2001] with differences in the power series due to the addition of the stroboscopic illumination source. While these differences increase the mathematical complexity of the acquired interferogram, extraction of optical phase can be accomplished, as shown in Section 3, by linear combinations of a set of four acquired frames.

APPENDIX B. Additive noise effects on phase modulating interferometry

To determine the optimal reference excitation amplitude, ψ, and phase, θ, the influence of additive noise on the calculation of the optical phase, ϕ was studied. As with Dubois [2001], this Thesis assumes a zero mean Gaussian noise, represented by

$$\langle n_p \rangle = 0 \tag{B.1}$$

and

$$n_i n_j = \begin{cases} \sigma^2 \text{ if } i = j \\ 0 \text{ if } i \neq j \end{cases} , \tag{B.2}$$

applied to each of the four frames where the magnitude of the additive noise signal is assumed to be much weaker than the recorded signal while equally contributing to all frames in a given set, as shown in Eq. B.3,

$$|n_p| << I_p \quad . \tag{B.3}$$

These additive noise assumptions have been validated by Luth [1989] for high signal-to-noise ratio images acquired through standard CMOS or CCD array systems.

The addition of additive noise, *n*, will cause the instantaneous intensity equation to take the form shown in Eq. B.4, for an arbitrary relative phase, as

$$I(x,y) = I_B(x,y) + I_M(x,y) \cdot \cos[\phi(x,y) + \phi_R(x,y)] + n \quad . \tag{B.4}$$

Following the derivation procedure presented in Section 3, a tangent function, Eq. B.5, can be recovered containing the optical phase and a phase error term, ε, as

$$\tan(\phi + \varepsilon) = \frac{K_c}{K_s} \cdot \frac{\Sigma_s + N_s}{\Sigma_c + N_c} \quad . \tag{B.5}$$

N_s and N_c, shown in Eqs B.6 and B.7 respectively, represent the error present within the linear frame combinations of Σ_s and Σ_c and take the form:

$$N_s = -n_1 + n_2 + n_3 - n_4 \quad , \tag{B.6}$$

and

$$N_c = -n_1 + n_2 - n_3 + n_4 \quad . \tag{B.7}$$

This tangent function shall be represented by η for simplicity in future reference.

The error term must be extracted from within the tangent calculation to determine its magnitude and full field behavior. To accomplish this, the tangent term is approximated with a third order Taylor series with respect to ε, derived through MathCad [2001] shown as Eq. B.8. Equation B.8 is of the form,

$$\tan(\phi + \varepsilon) = \tan(\phi) + [1 + \tan(\phi)^2] \cdot \varepsilon + \tan(\phi) \cdot [1 + \tan(\phi)^2] \cdot \varepsilon^2 + O(\varepsilon^3) \quad , \tag{B.8}$$

which can be written as Eq. B.9,

$$\eta = a_0 + a_1\varepsilon + a_0 a_1 \varepsilon^2 \quad , \tag{B.9}$$

for simplicity. The removal of the third order approximation term simplifies the form of Eq. B.9 although its effect on future calculations must be considered.

Following the procedure outlined in Dubois [2001], the mean error and mean squared error can be extracted from Eq. B.9. While accomplishing this, a third order accurate approximation must be maintained for consistency with the previously indicated Taylor series. Equations B.10 and B.11 show the resultant mean and mean squared error functions,

$$\langle \varepsilon \rangle = \frac{1}{a_1^3}\left[a_0 a_1 \langle \eta^2 \rangle - a_0^3 a_1 - \left(a_1^2 + 2a_0^2 a_1\right)\langle \eta \rangle + a_0 a_1^2 + 2a_1 a_0^2 \right] \quad , \tag{B.10}$$

and

$$\langle \varepsilon^2 \rangle = \frac{a_0^2 - 2a_0\langle \eta \rangle + \langle \eta^2 \rangle}{a_1^2} \quad . \tag{B.11}$$

Direct solution of Eqs B.10 and B.11 assumes knowledge of the magnitude of additive error within the recovered signal through the mean and mean squared η term. To determine the independent contributions of the phase constants and optical phase on the additive error, the right hand side of Eq. B.5 must first be investigated.

The right hand side of Eq. B.5 can be rewritten as shown in Eq. B.12. This allows for calculation of η as a function of the optical phase, ϕ, through the linear frame combinations, Σ_s and Σ_c, and the resultant additive error contributions, N_s and N_c, by

$$\eta = \tan(\phi) \cdot \left(\frac{1 + \frac{N_s}{\Sigma_s}}{1 + \frac{N_c}{\Sigma_c}} \right) \quad . \tag{B.12}$$

As before, this term can be approximated by a third order series [MathCad, 2001] and squared to form two dependant equations, B.13 and B.14 respectively.

$$\eta = \tan(\phi) \cdot \left(1 + \frac{N_s}{\Sigma_s}\right)\left[1 - \frac{N_c}{\Sigma_c} + \left(\frac{N_c}{\Sigma_c}\right)^2\right] \tag{B.13}$$

and

$$\eta^2 = \tan(\phi)^2 \cdot \left[1 + 2\frac{N_s}{\Sigma_s} + \left(\frac{N_s}{\Sigma_s}\right)^2\right]\left[1 - 2\frac{N_c}{\Sigma_c} + 3\left(\frac{N_c}{\Sigma_c}\right)^2\right] \quad . \tag{B.14}$$

An infinite time average can be applied to these error equations, allowing for the calculation of the respective mean and mean squared functions. The infinite time average is based on the assumed additive noise behavior and so results in the statistical properties seen in Eq. B.15. In Eq. B.15, it is shown that the mean noise amplitude is zero due to the assumed zero mean behavior of the Gaussian additive noise. Similarly, the mean combination of the two additive noise constants is non-zero only when the constants have the same amplitude.

$$\langle N_s \rangle = 0 \quad , \langle N_c \rangle = 0$$

and (B.15)

$$\langle N_s N_s \rangle = 4\sigma^2 \quad , \langle N_c N_c \rangle = 4\sigma^2$$

With the properties determined in Eq. B.15, the infinite time average of Eqs B.13 and B.14 can then be written as shown in Eqs B.16 and B.17,

$$\langle \eta \rangle = \tan(\phi) \cdot \left(1 + \frac{4\sigma^2}{\Sigma_c} \right) \tag{B.16}$$

and

$$\left\langle \eta^2 \right\rangle = \tan(\phi)^2 \cdot \left[1 + 4\sigma^2 \left(\frac{1}{\Sigma_s^2} + \frac{1}{\Sigma_c^2} \right) \right] \quad . \tag{B.17}$$

Combining equations B.16 and B.17 with B.10 and B.11 and simplifying, we can find that the mean error and mean squared error are inversely related to the magnitude of the sine and cosine constants while being directly related to the obtained optical phase. Therefore it is possible to represent the mean and mean squared error in Eqs B.18 and B.19 as,

$$\langle \varepsilon \rangle = \frac{\sigma^2 \pi^2}{8 {I_M}^2 T^2} \sin(2\phi) \left[\frac{1}{K_c(\psi,\theta)^2} - \frac{1}{K_s(\psi,\theta)^2} \right] \tag{B.18}$$

and

$$\left\langle \varepsilon^2 \right\rangle = \frac{\sigma^2 \pi^2}{4 {I_M}^2 T^2} \left[\frac{\sin(\phi)^2}{K_c(\psi,\theta)^2} + \frac{\cos(\phi)^2}{K_s(\psi,\theta)^2} \right] . \tag{B.19}$$

From Eq. B.18, we find that the mean error is equal to zero for equal values of K_c and K_s. As this condition of equality was enforced to eliminate the contribution of the phase constants during recovery of optical phase, the mean squared error is used to provide a secondary indication of the error effects within the developed system. As shown in Eq. B.19, the mean squared error is minimized when the phase constants, K_c and K_s, are maximized. These error terms can then be minimized through appropriate selection of the reference excitation amplitude and phase.

A consequence of this derivation is the realization that any inequality between K_c and K_s will result in a non-random error, appearing as a sinusoidal-type pattern at twice the frequency of the optical phase.

The standard deviation of the additive noise errors can be found as the square root of the mean squared error term. Assuming that K_c and K_s are equivalent, its magnitude is found as Eq. B.20,

$$\sqrt{\left\langle \varepsilon^2 \right\rangle_{\min}} = \frac{\sigma \pi}{2 I_M T \cdot K_s} . \tag{B.20}$$

From Eq. B.20, we see that maximization of the magnitude of the phase constants will minimize the standard deviation of any recovered error due to additive noise effects.

APPENDIX C. Front panel of the developed LabVIEW™ VI for control of the phase modulating interferometer

Figures C.1 to C.3 display the various settings and controls available within the developed user interface. Each figure displays a different set of usable tabs. As mentioned in Appendix F, settings under the "Data Processing" and "Image Analysis" tabs have not been enabled in the current software build. However, the underlying functions are present within the block diagram (Appendix D.) and can be implemented in future builds as needed. These tabs are designed to provide image feedback, specifically concerning contrast and the mean, minimum, maximum pixel values. The graph shown next to the tab controls displays the values of the mid-row or mid-column within the wrapped phase or modulation maps, based on which calculation is currently being displayed. If both calculations are called simultaneously, the chart will alternate between viewing of both processed maps. Selection of the mid-row/column is done through the "Operation Mode" block, as shown in Appendix F.

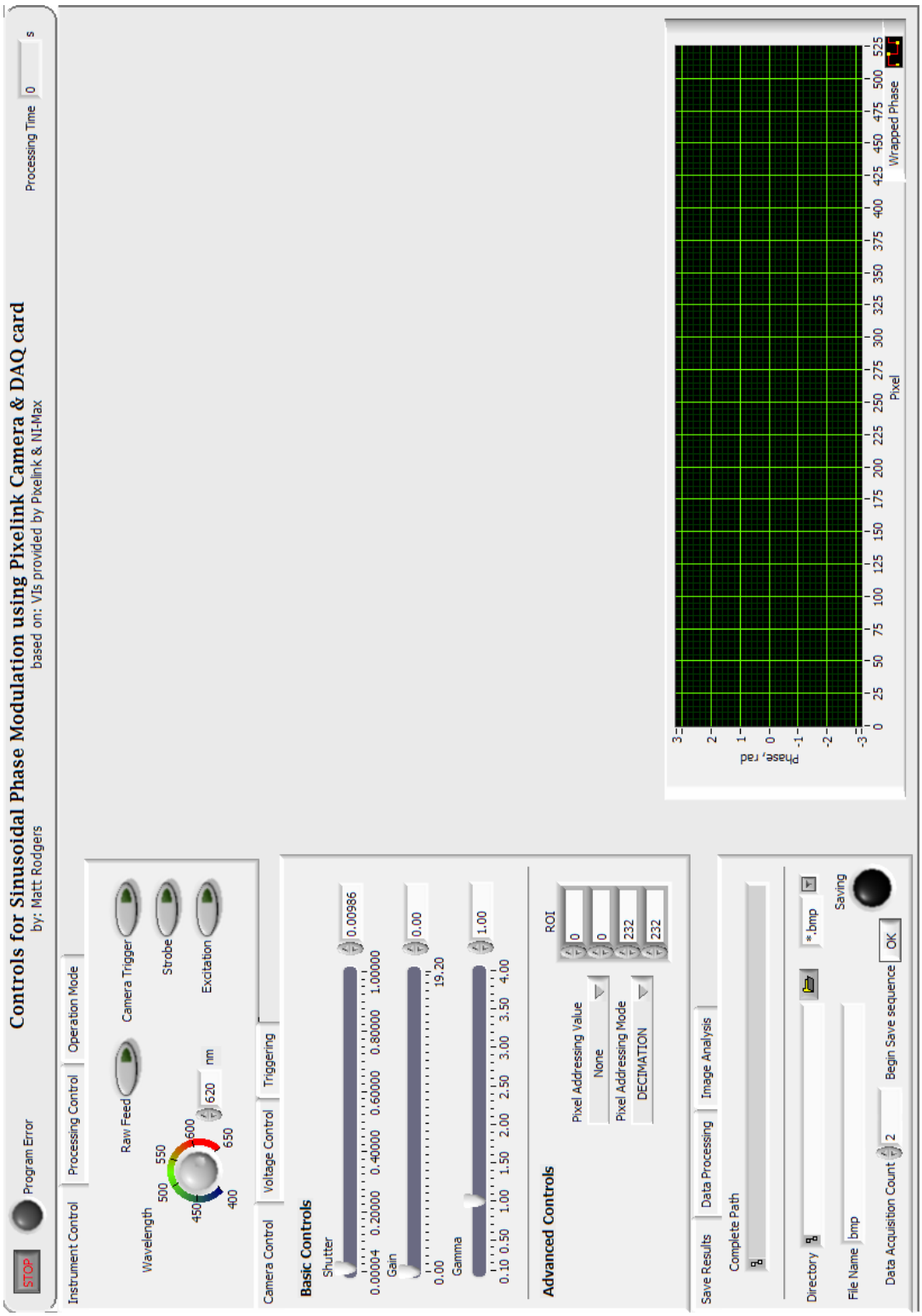

Fig. C.1. Settings 1: Basic software controls, Base camera settings, Save Results.

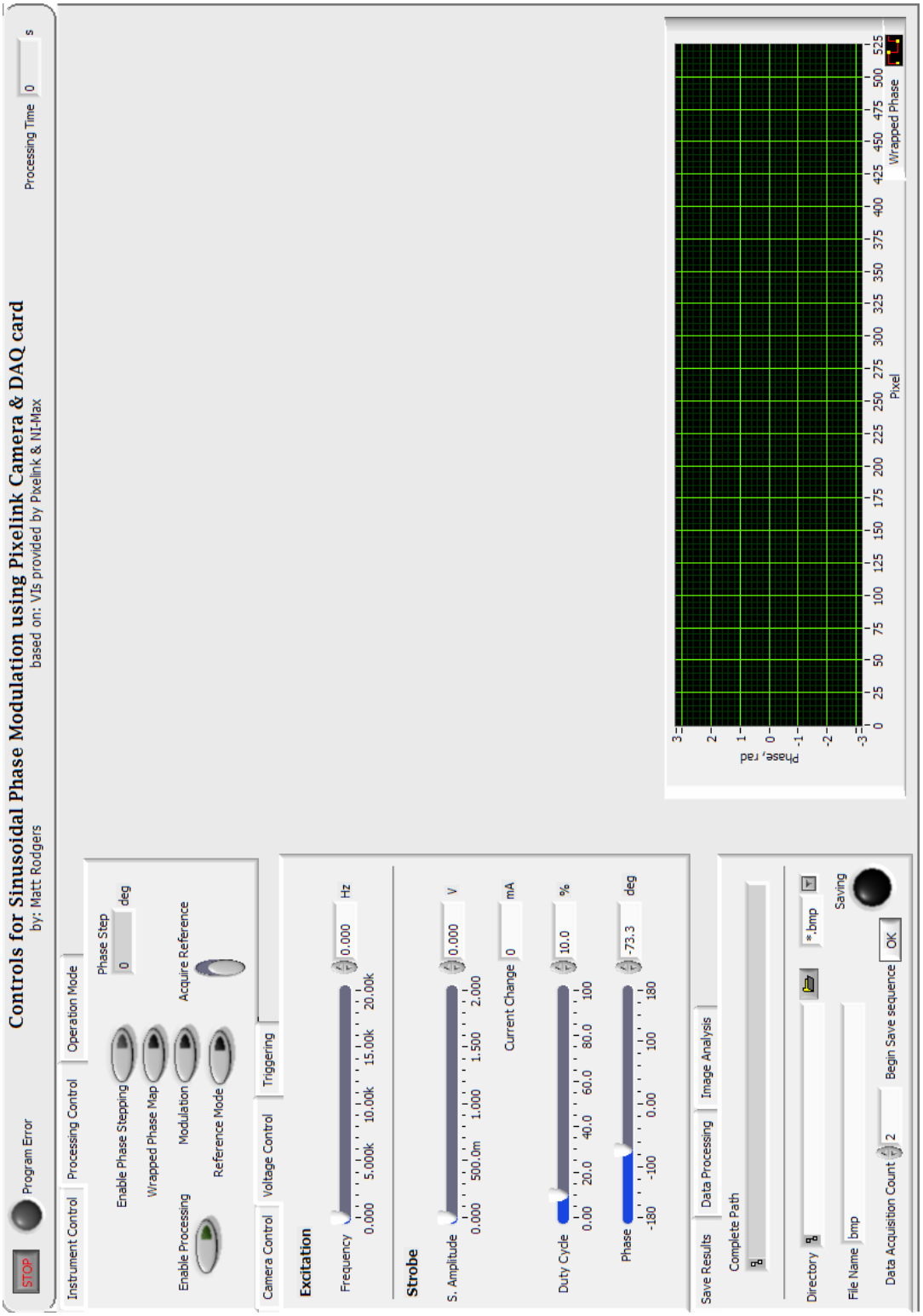

Fig. C.2. Settings 2: Image processing settings, Output voltage controls, Save Results.

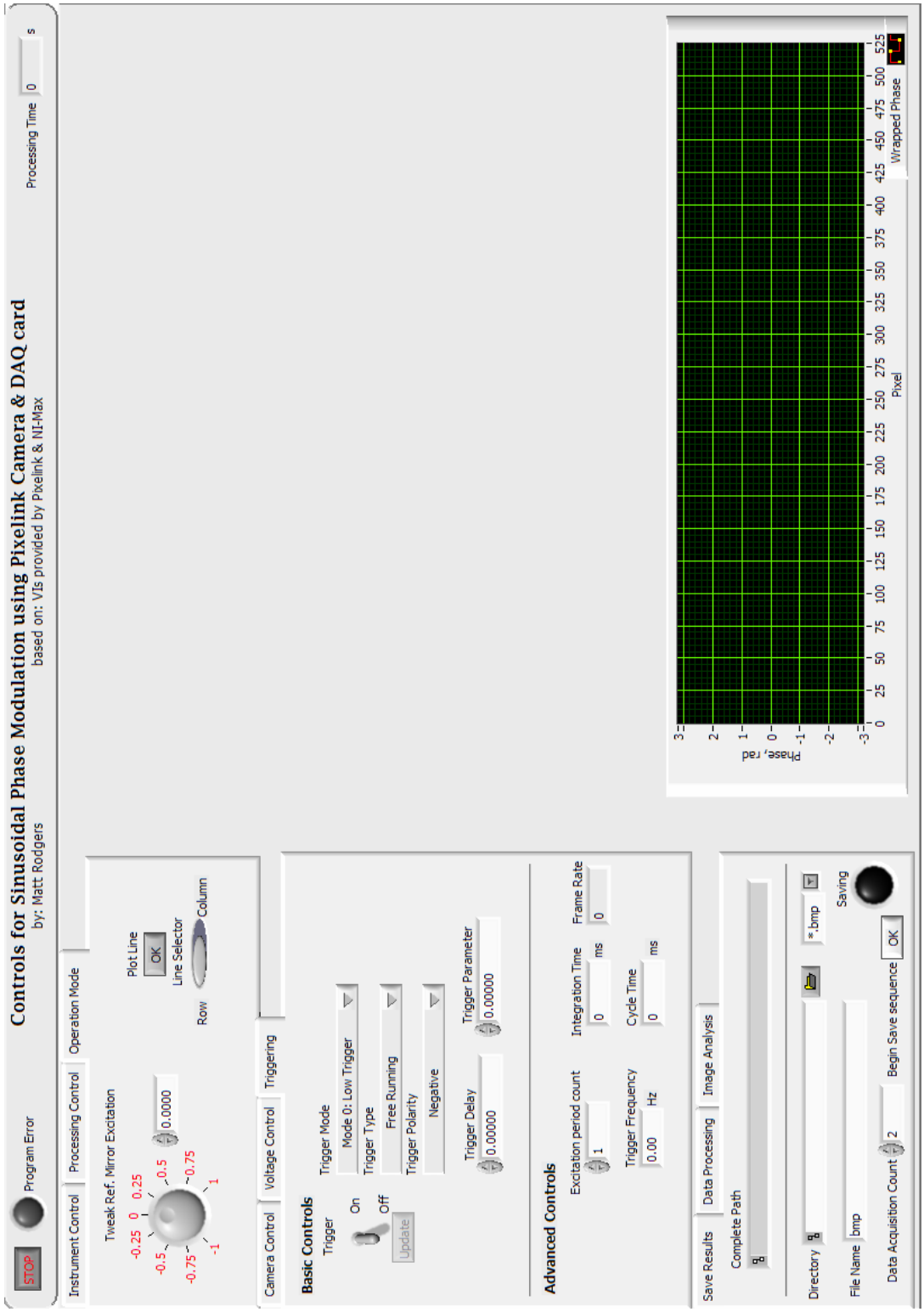

Fig. C.3. Settings 3: Operation/Plot mode, Camera triggering controls, Save Results.

APPENDIX D. Block diagram of the developed LabVIEW™ VI for control of the phase modulating interferometer

The following is the developed LabVIEW™ block diagram code for implementation of the phase modulating interferometer using the hardware and software modules indicated in Section 4.2.1. The main body is presented in Fig. D.1 and commented to highlight the functionality of major code blocks. Case blocks and operational event structures are presented in their default operational state within the completed block diagram. LabVIEW™ case structures are equivalent to the "If… then…" statements found in other programming languages. Figures D.2 – D.6 display alternate forms of each case structure with functional descriptions of each structure. Event cases which provide responses to changes on the user interface are shown with functional descriptions in Figs D.7 – D.22. The function of individual structures is described with each event case.

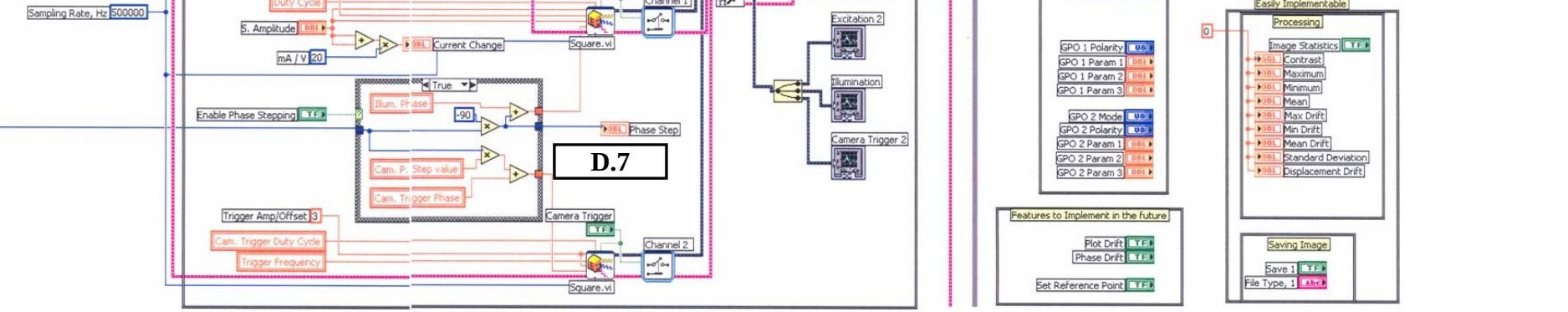

True: Display raw image feed
False: Close window

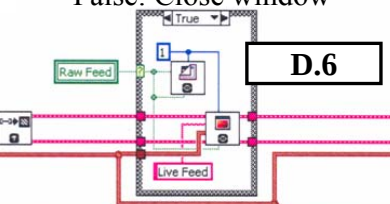

Transform 16-bit 2-D
image array to double

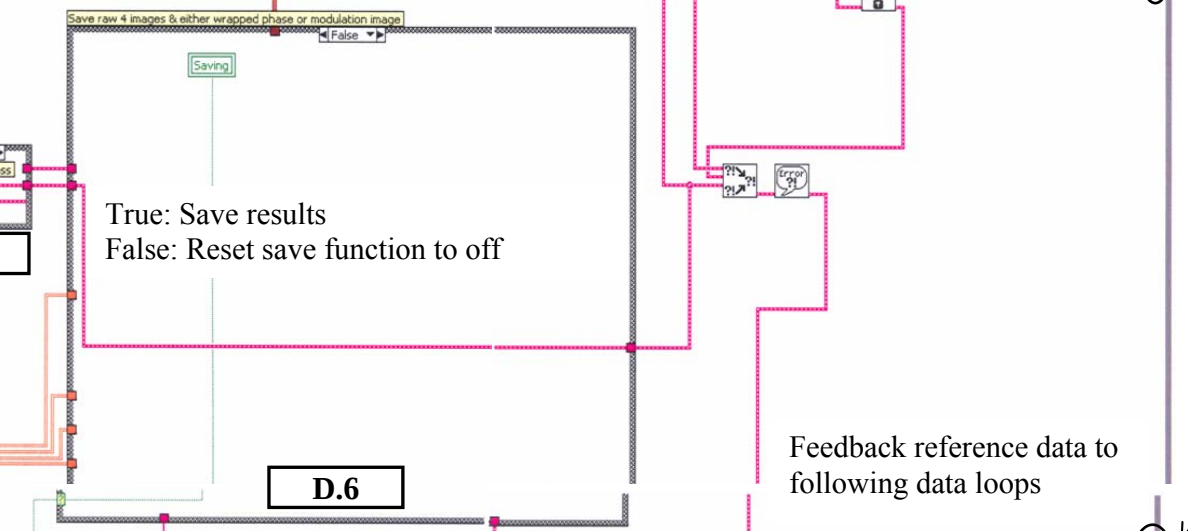

True: Save results
False: Reset save function to off

Feedback nodes to pass data between
program loops

Feedback reference data to
following data loops

lculate Ref. values
o function

Save sequential data set(s)
based on UI settings

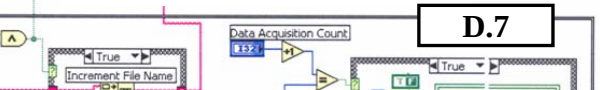

Case Structures:

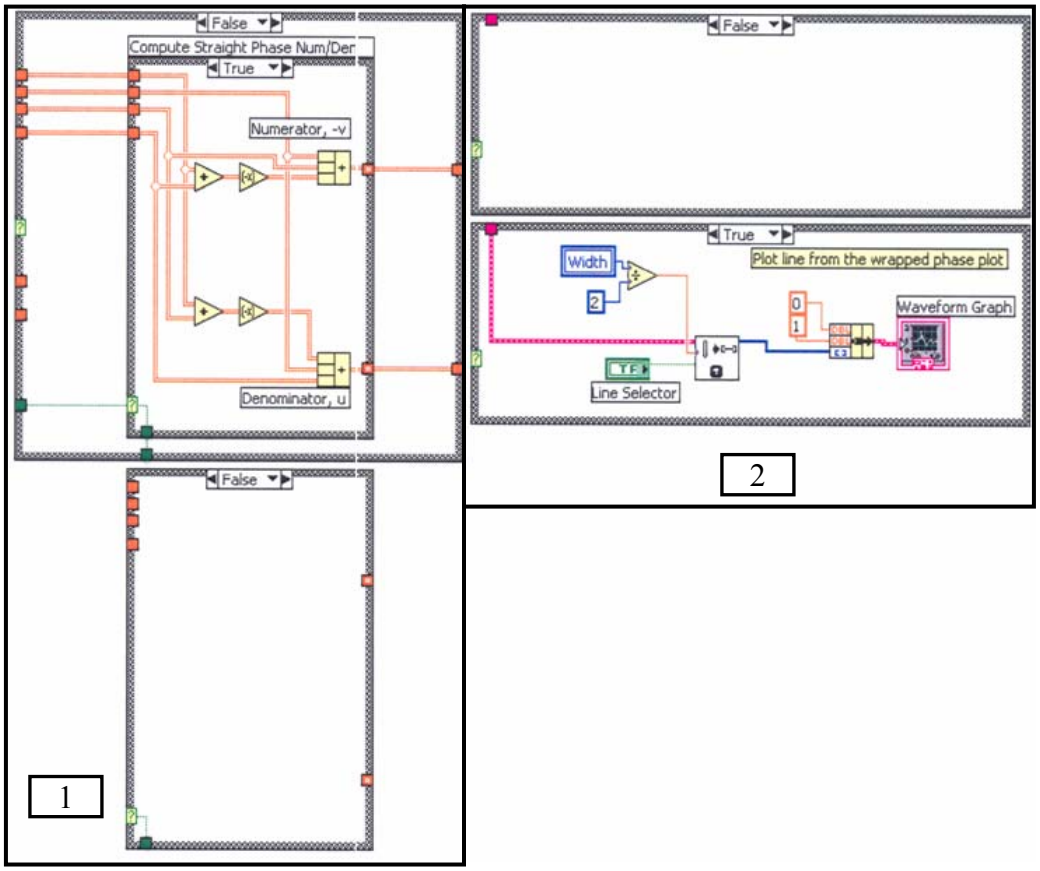

Fig. D.2. Block diagram case structure set 1.

Group 1 – Calculates the numerator and denominator terms used in the arctangent wrapped phase map calculation. The case shown in the block diagram calculates the numerator and denominator terms used for calculation of the relative wrapped phase map.

Group 2 – When true, displays the middle row or column of the displayed wrapped phase map or optical modulation map.

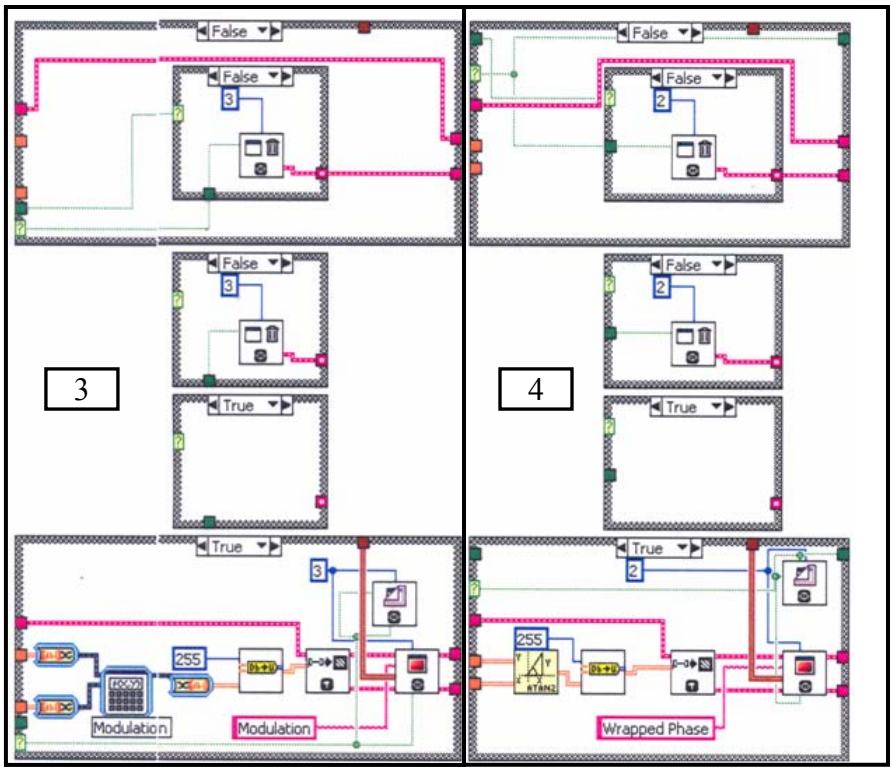

Fig. D.3. Block diagram case structure set 2.

Group 3 – Calculates the optical modulation of within the imaged region of interest. Normalizes and displays the resulting map with an 8-bit resolution in window number 3. If the modulation is low, the display will appear with a low signal-to-noise ratio. If the optical modulation display is set to off, window 3 is automatically closed and the modulation is not calculated.

Group 4 – Calculates the wrapped phase map using a $-\pi - +\pi$ arctangent calculation within the imaged region of interest. Normalizes and displays the resulting map with an 8-bit resolution in window number 2. If the optical modulation is low, the display will appear with a low signal-to-noise ratio. If the wrapped phase map display is set to off, window 2 is automatically closed and the wrapped phase is not calculated.

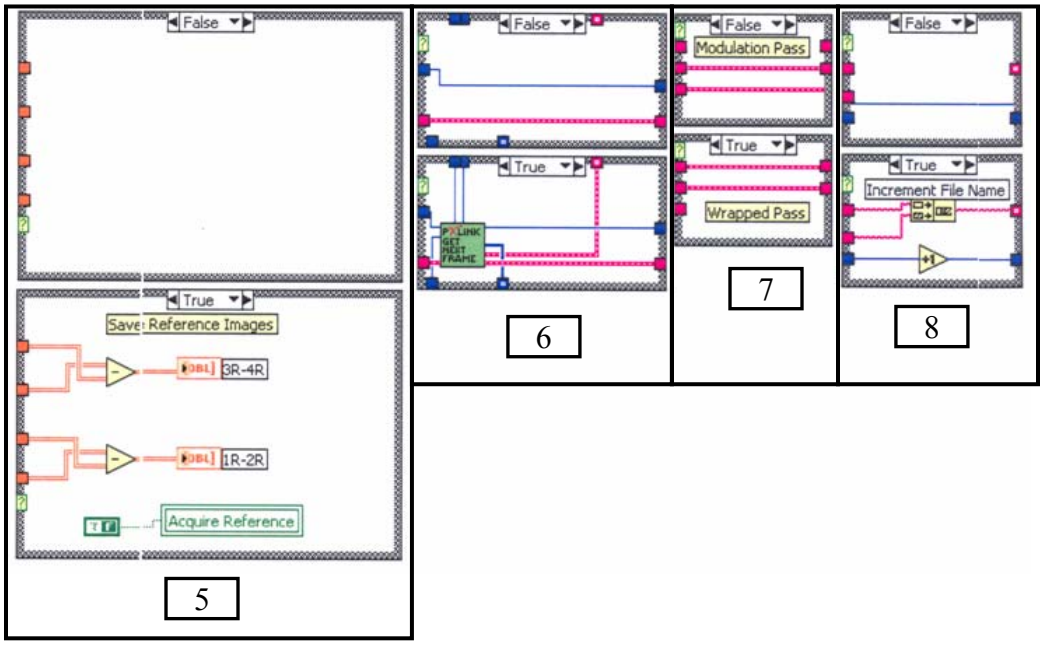

Fig. D.4. Block diagram case structure set 3.

Group 5 – When true, pre-calculates terms used in calculation of the numerator and denominator for determination of the relative optical phase and modulation maps.

Group 6 – Grabs the next available frame from the onboard buffer of the operating PixeLink camera for calculation purposes.

Group 7 – Transfers the calculated wrapped phase or optical modulation map for creation of a saved output file.

Group 8 – During a sequential save operation, automatically increments the save file name to prevent overwriting.

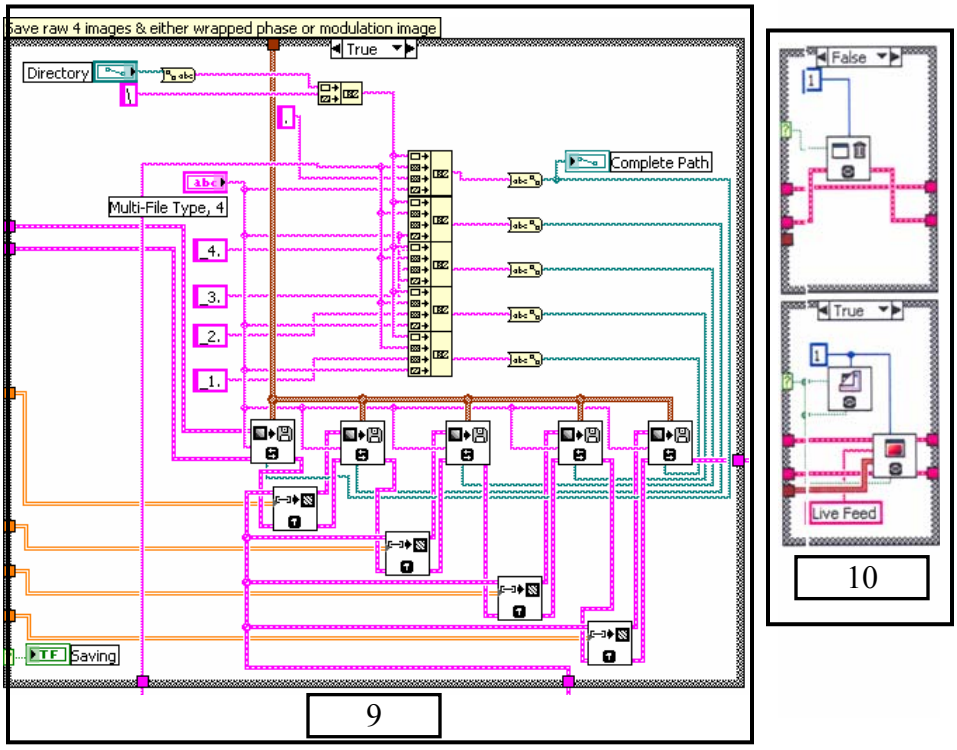

Fig. D.5. Block diagram case structure set 4.

Group 9 – Saves the four acquired images needed for calculation of the wrapped phase map and optical modulation map with the calculated wrapped phase or modulation map.

Group 10 – Displays the unprocessed feed from the attached camera system.

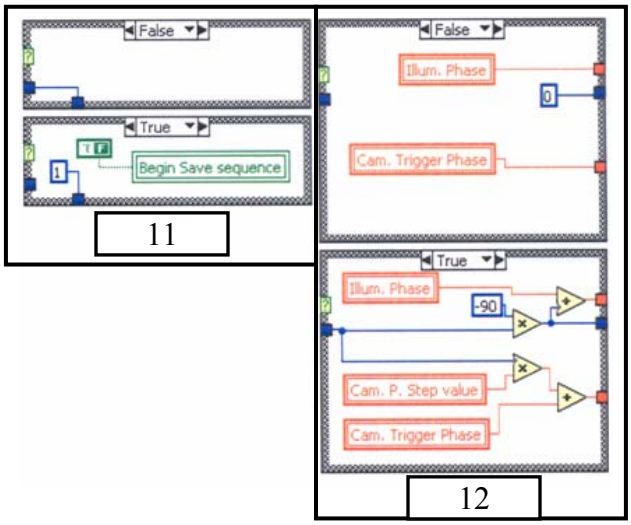

Fig. D.6. Block diagram case structure set 5.

Group 11 – Once the save operation is completed; reset the file count to 1 for future sequential save operations.

Group 12 – Calculates the relative phase between the stroboscopic illumination signal and the modulation signals at the current phase step and returns this value for signal generation.

Event Structures: Cases 0 – 10

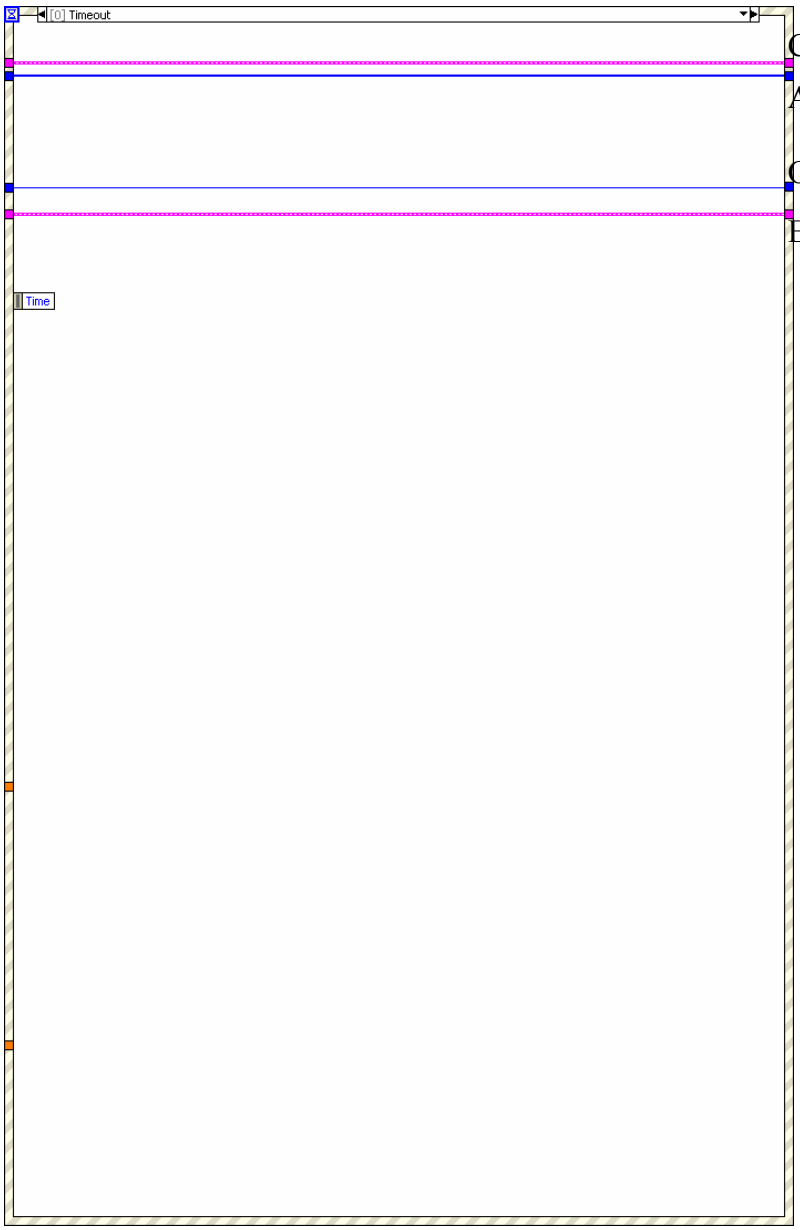

Fig. D.7. Default event, when there has been no changes on the user interface, continue program with all prior settings.

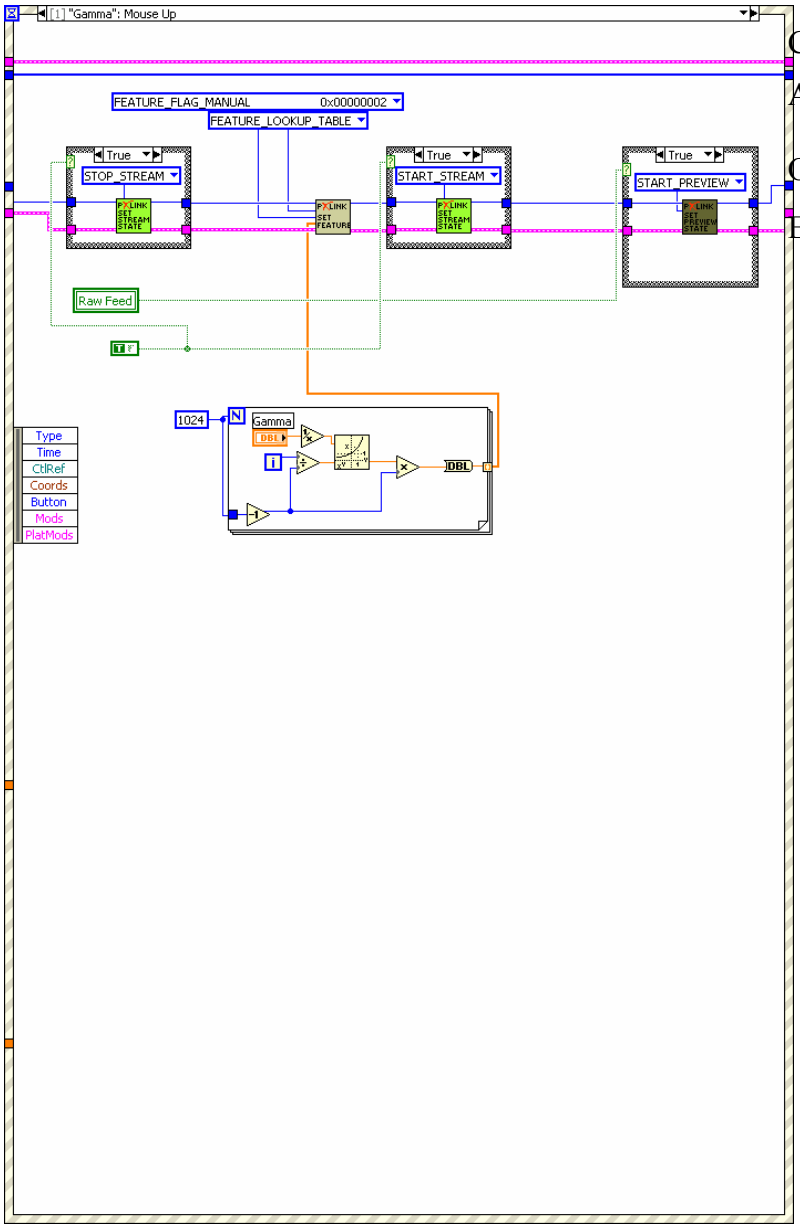

Fig. D.8. Event structure 1a, when the gamma has been adjusted: Stop the camera feed while adjusting the camera gamma value and restart the camera feed.

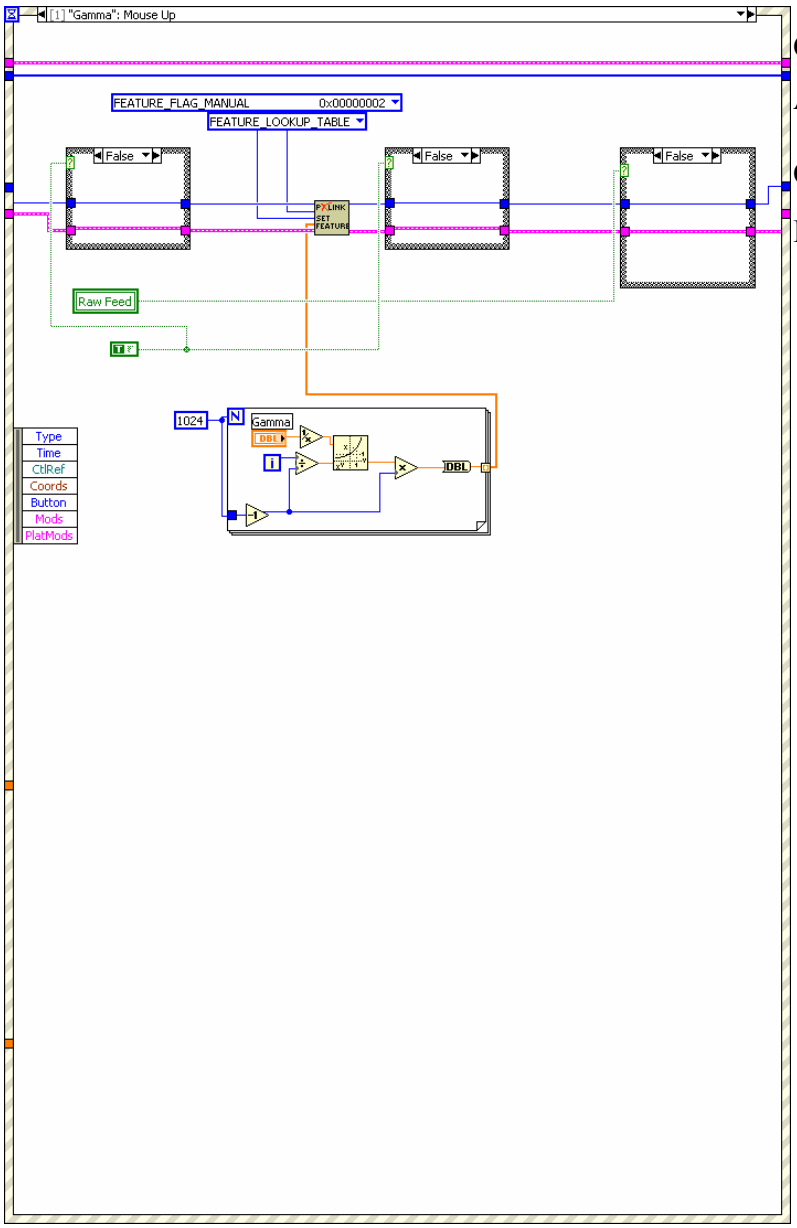

Fig. D.9. Event structure 1b, when the gamma has been adjusted:
adjusting the camera gamma value when the camera is not providing an image feed.

Fig. D.10. Event structure 2, if the shutter exposure time has been adjusted, send the new value to the camera system. This setting is not read when the camera is operating in "Low Integrate" trigger mode.

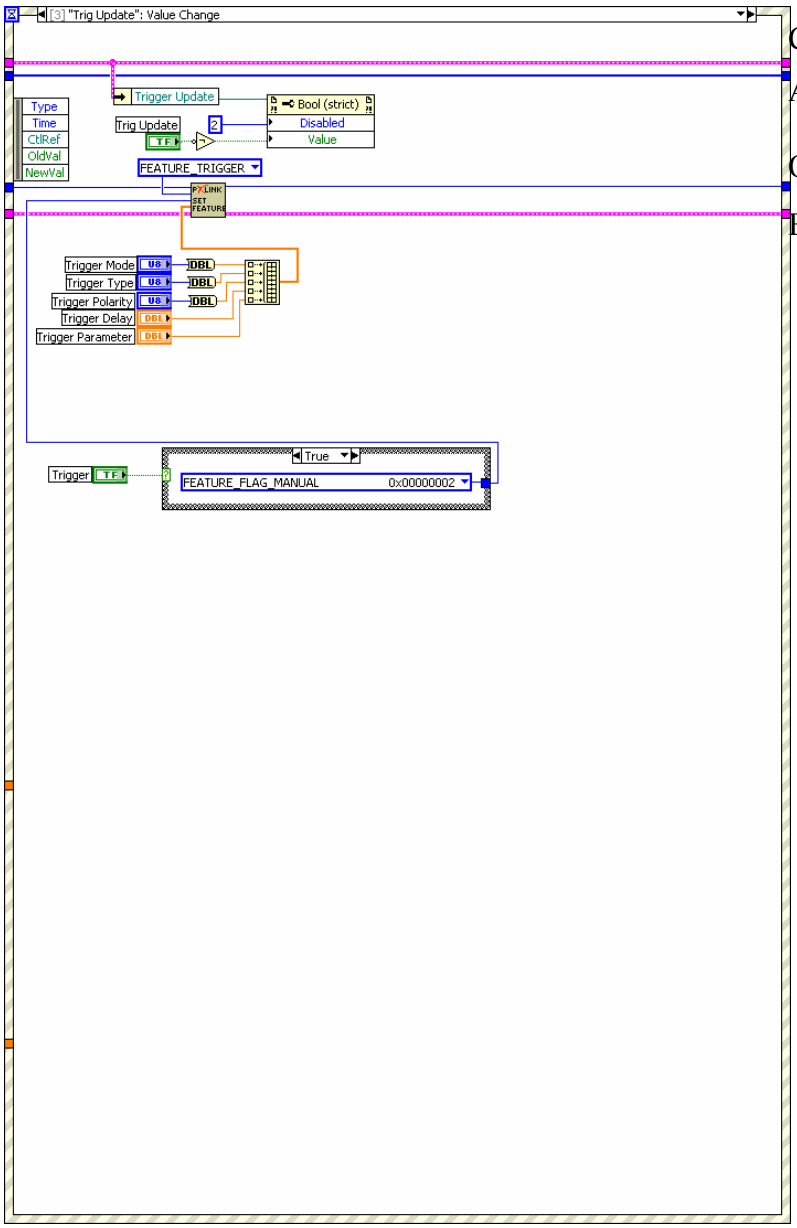

Camera control settings

Attached camera id numbers

Operating camera id number

Error flow

Fig. D.11. Event structure 3a, update the current camera trigger settings based on parameters found on the user interface and operate under the new settings. Parameters are explained in Appendix F.

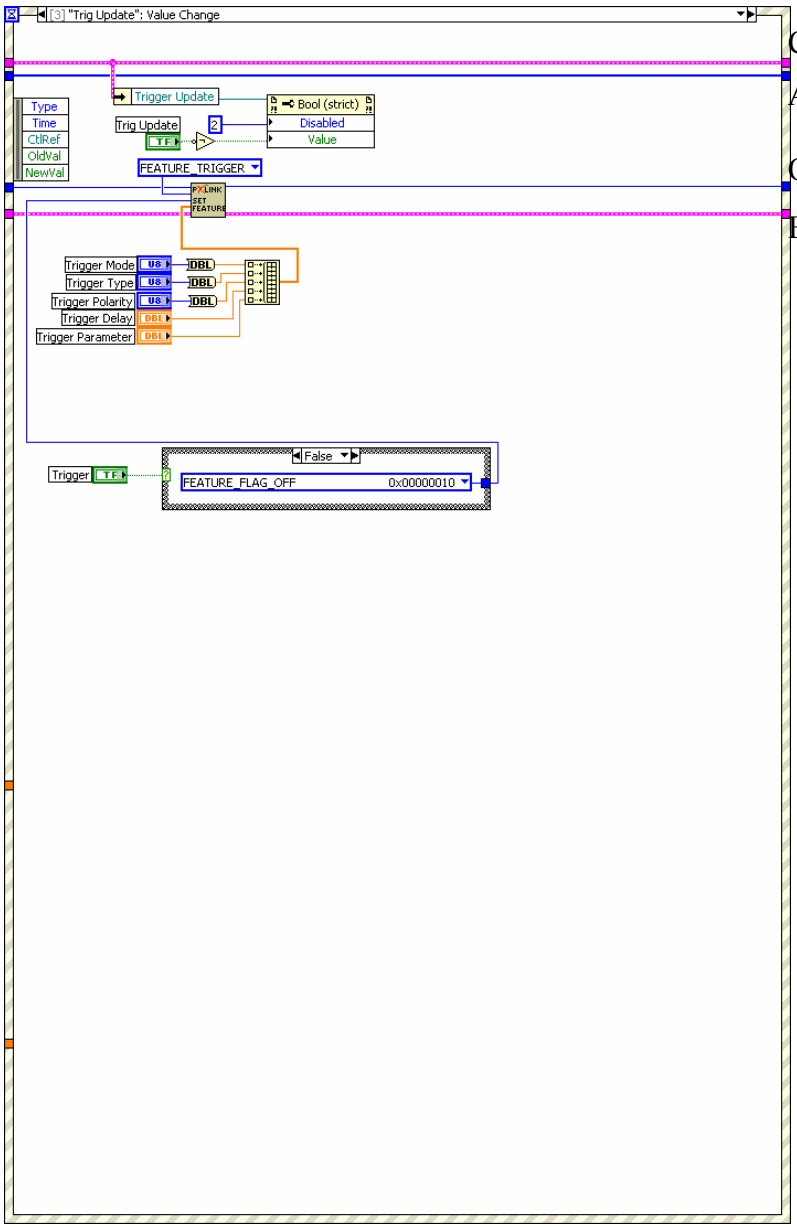

Fig. D.12. Event structure 3b, update the current camera trigger settings based on parameters found on the user interface. Deactivate reading of the trigger settings for camera operation.

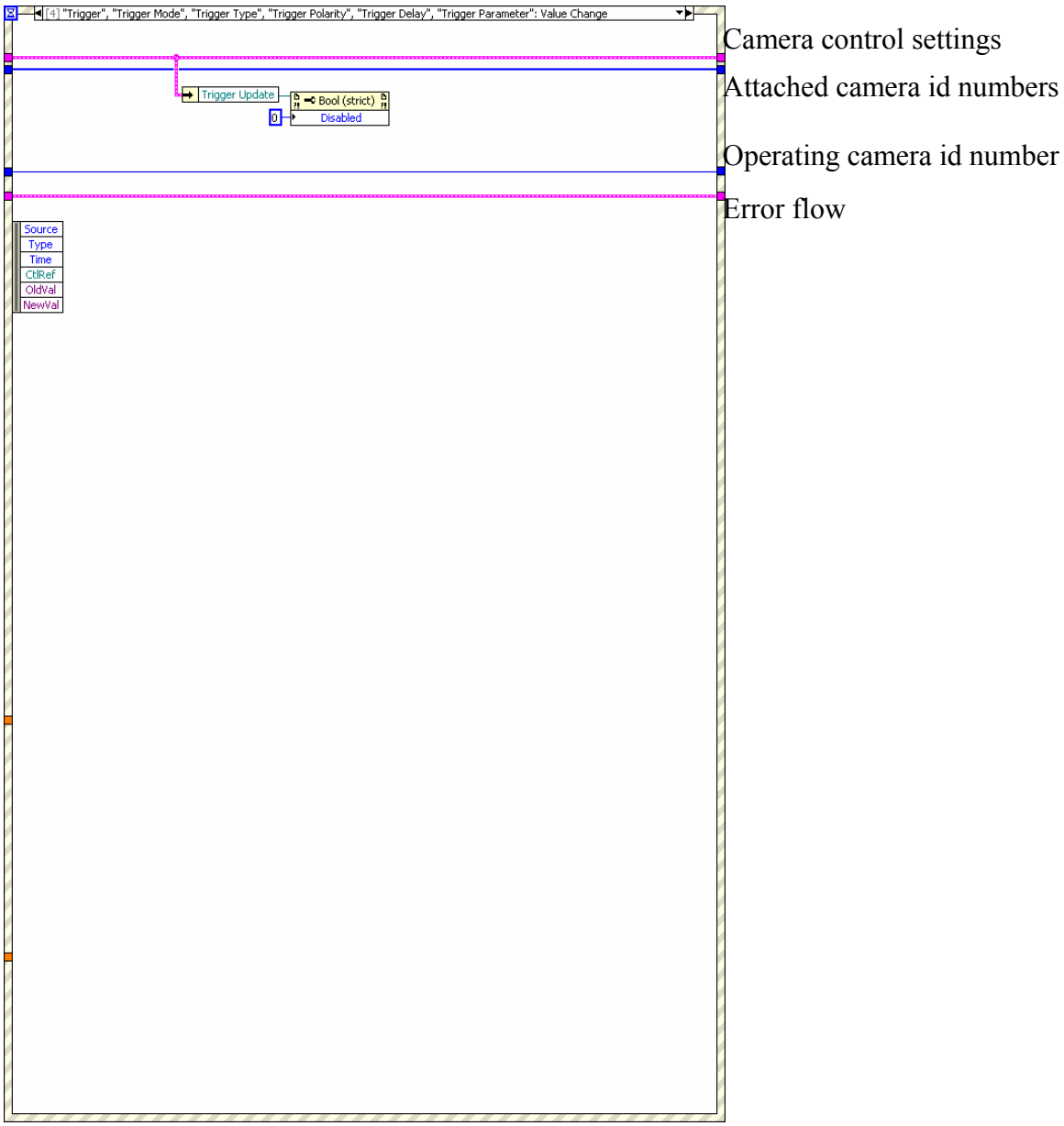

Fig. D.13. Event structure 4,this event enables the "Trigger Update" button on the interface to set triggering parameters on selected camera system.

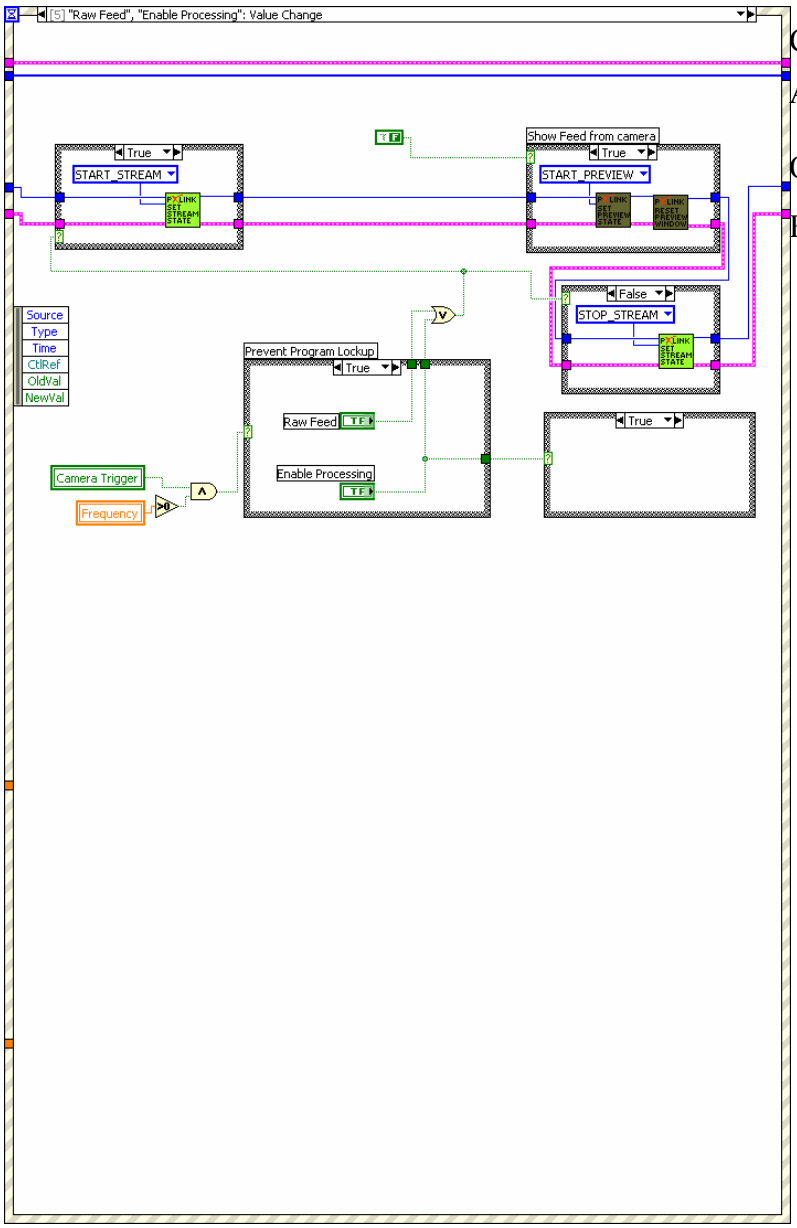

Fig. D.14. Event structure 5a, this event begins the display of the unprocessed camera feed if the trigger signal is being generated at a frequency above 0 Hz.

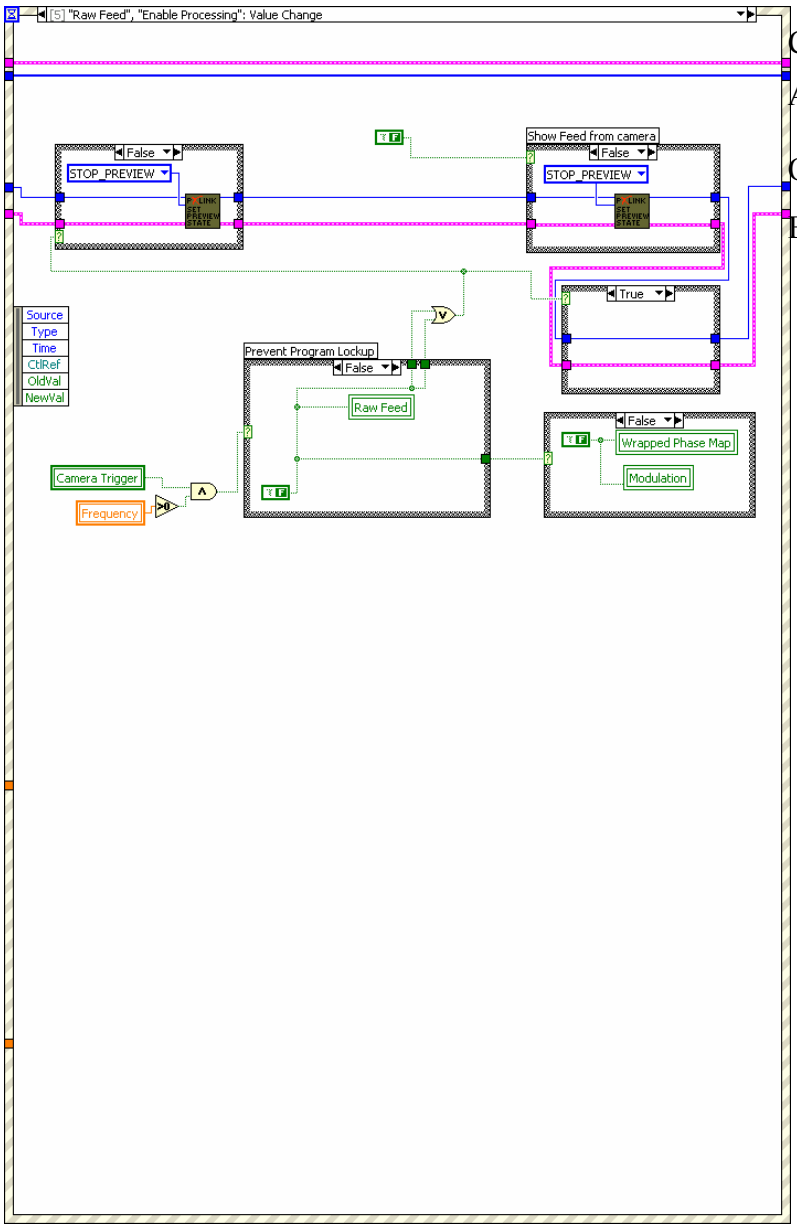

Fig. D.15. Event Structure 5b, this event displays the unprocessed camera feed but does not allow for image processing when either the camera trigger signal is not output or the modulation frequency is set to 0 Hz.

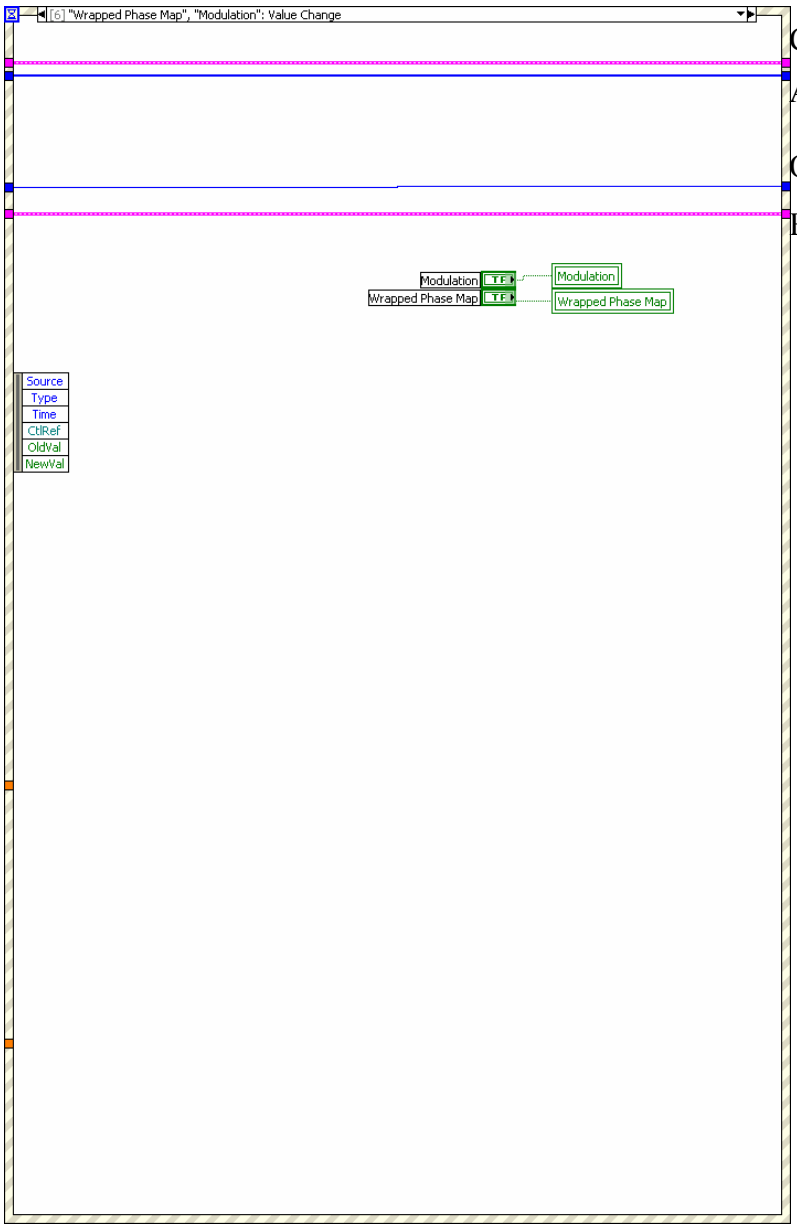

Fig. D.16. Event Structure 6, this event reads the current value of the "Wrapped Phase Map" and "Modulation" buttons from the user interface.

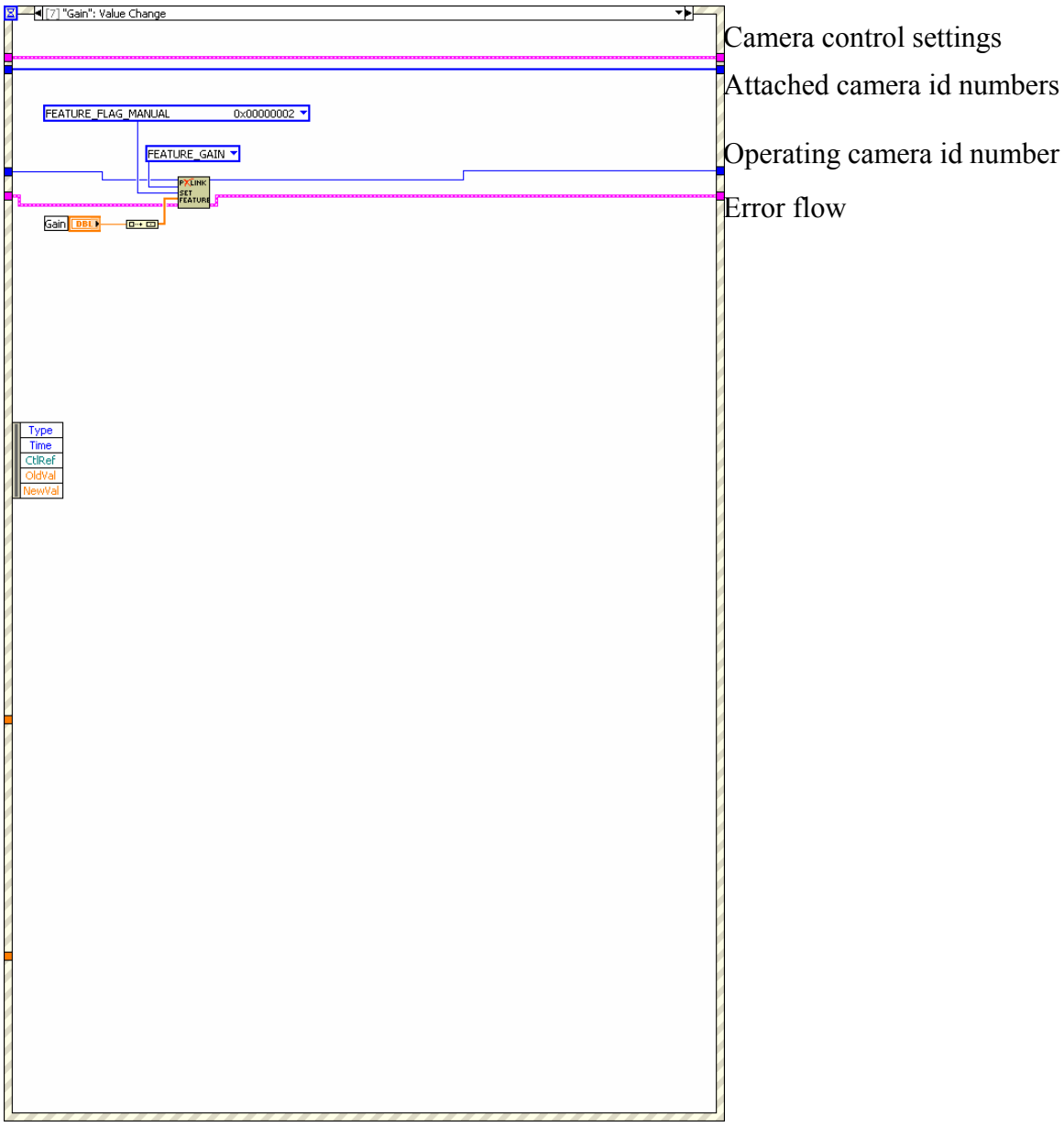

Fig. D.17. Event Structure 7, this event sets the gain value of the acquired images based on the currently selected value on the user interface.

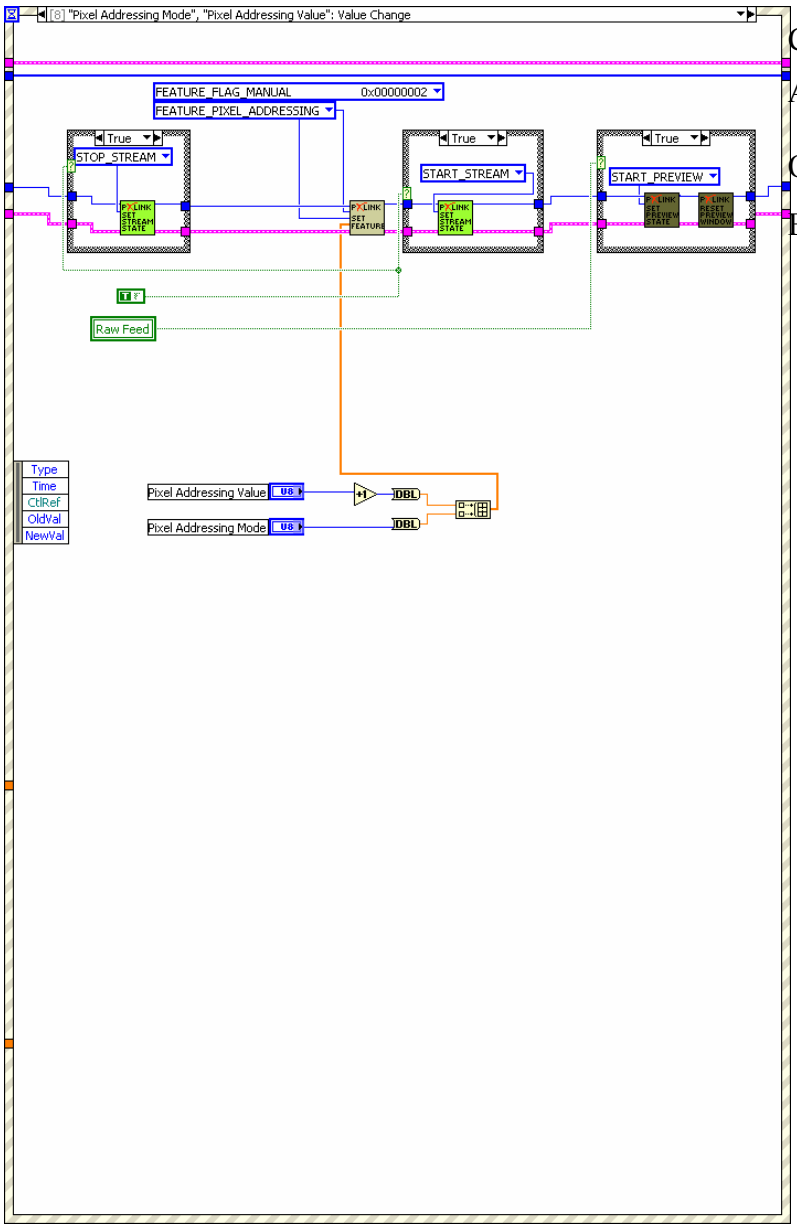

Fig. D.18. Event Structure 8a, this event stops the current image feed to set the pixel addressing mode and value as explained Appendix F. It then re-starts the feed stream and re-opens any image displays if previously enabled.

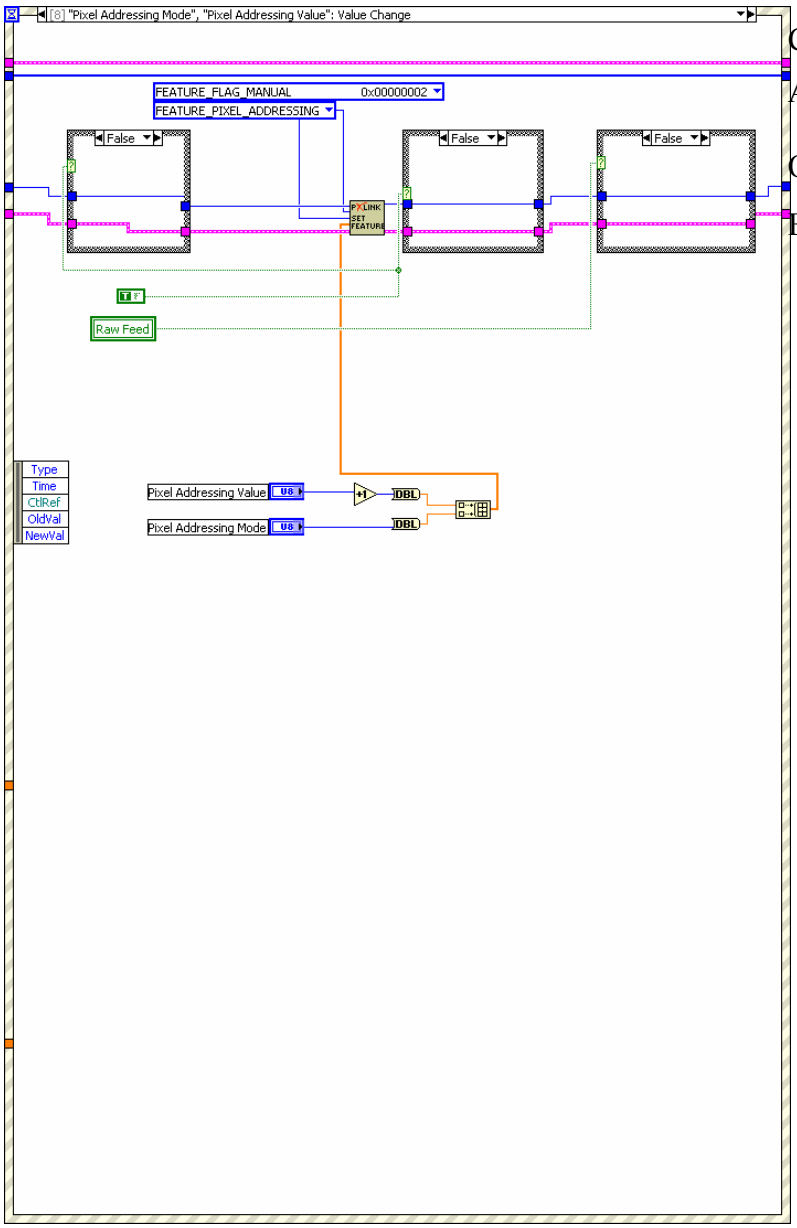

Fig. D.19. Event Structure 8b, this event sets the pixel addressing mode and value as explained Appendix F when the camera feed has not been enabled.

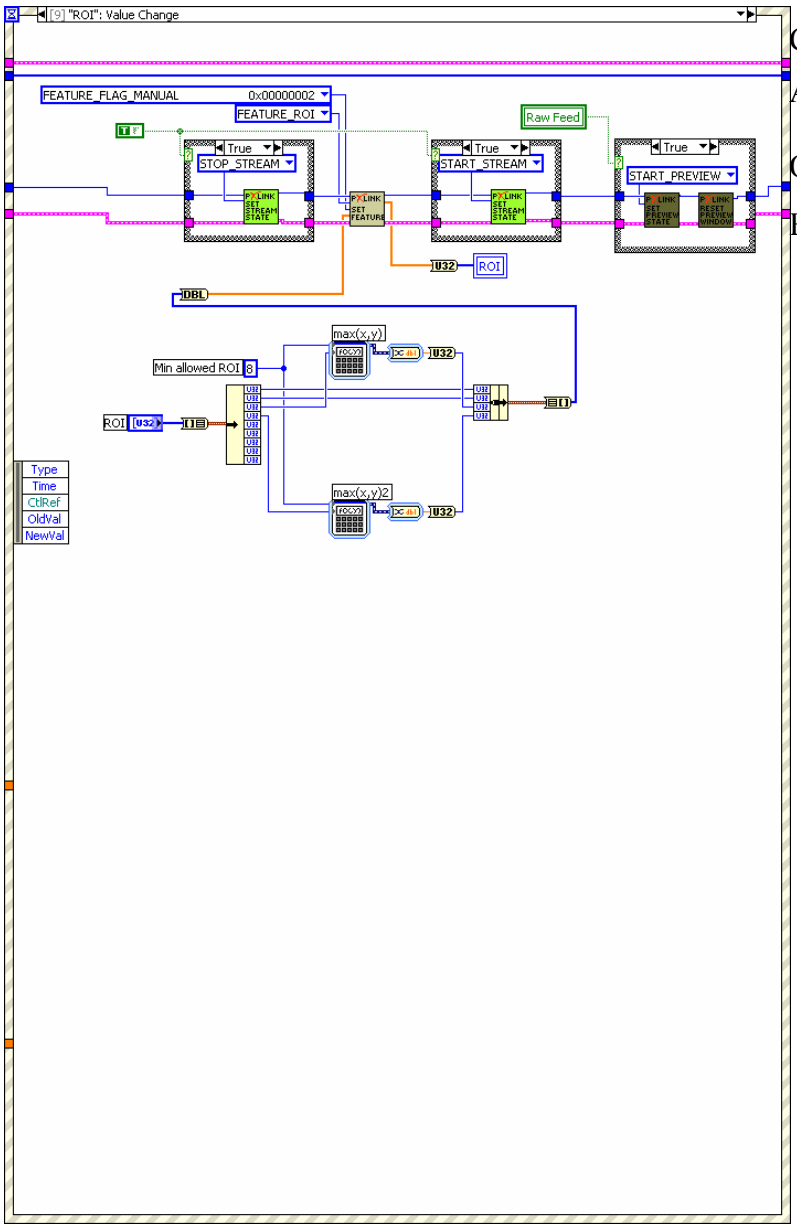

Fig. D.20. Event Structure 9a, this event stops the current camera feed to alter the region of interest (ROI) within camera view both in size and location. ROI values must be multiples of 8 and width/height must be equal for proper display and processing. No error checking has been implemented to ensure that the selected ROI is within the imaging array area

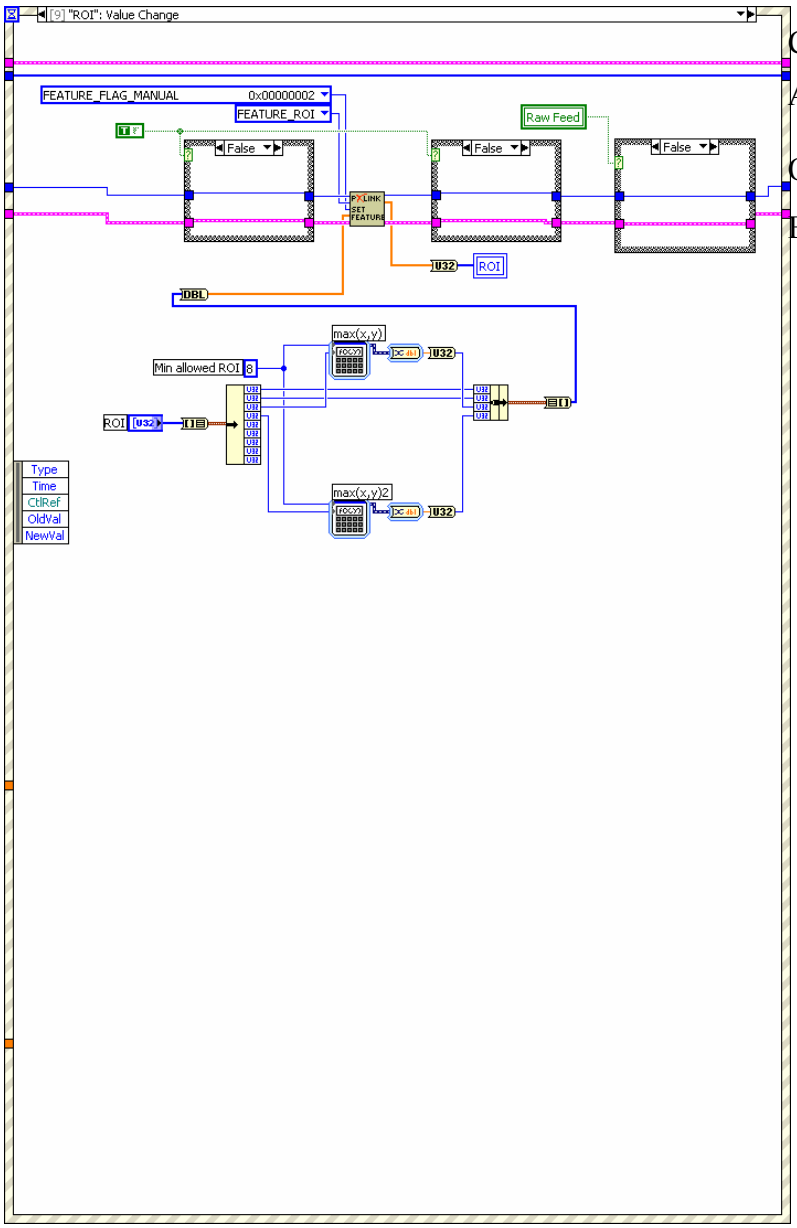

Fig. D.21. Event Structure 9b, this event alters the ROI within camera view both in size and location when camera feed is not previously enabled. Restrictions from figure D.20 apply.

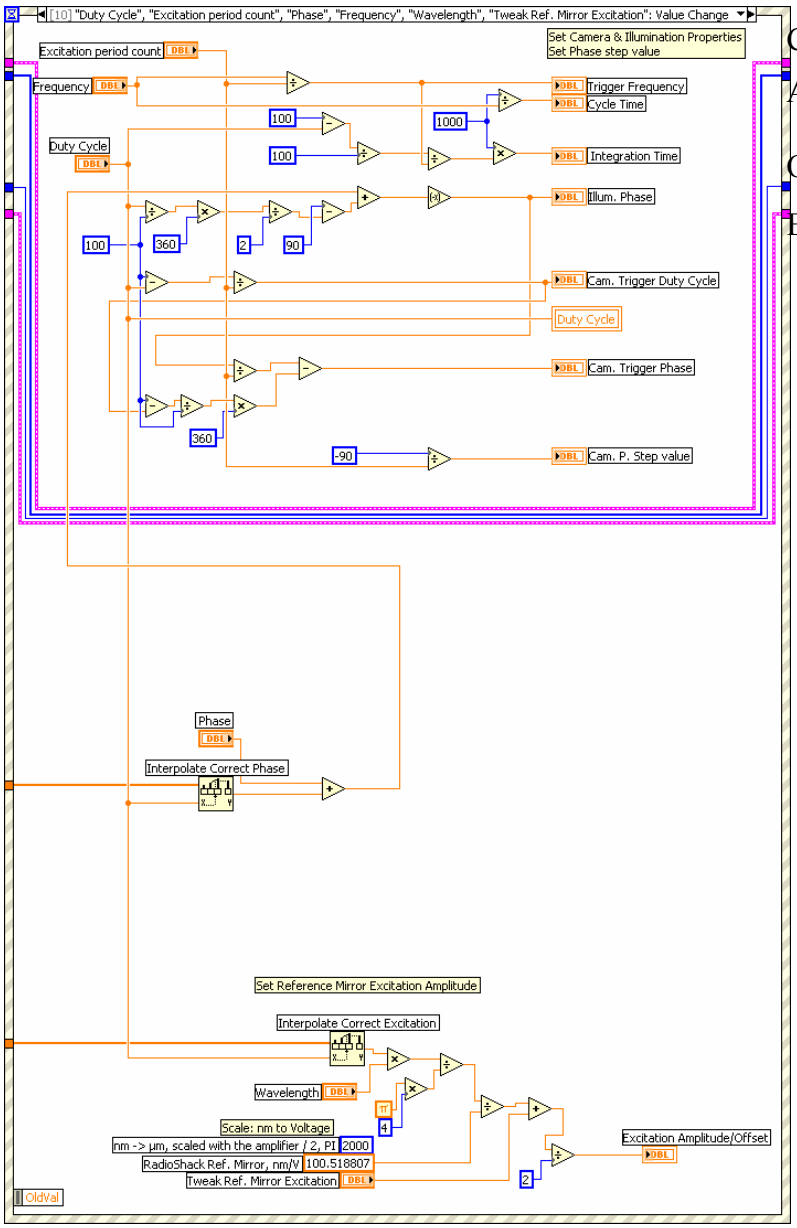

Camera control settings

Attached camera id numbers

Operating camera id number

Error flow

Fig. D.22. Event Structure 10, this event calculates the modulation and synchronization parameters for output voltage generation based on current UI settings and data read from the excitation parameter file. (Default Excel file is excite.xls).

APPENDIX E. Operation package installation

The code developed in this Thesis requires installation of National Instrument's LabVIEW™ 7.0, Measurement & Automation Explorer (MAX) 4.0.2, Image Acquisition software (IMAQ) with Vision 6.0, and IMAQ Vision Builder 6.0, or higher. The basic LabVIEW™ package is an open programming environment designed to interface interactive assistants and code generation to multiple hardware devices [LabVIEW™ 7.1, 2006]. Addition of the Measurement & Automation Explorer package allows for the control and simulation of National Instruments' and compatible devices. LabVIEW™ image acquisition/processing/saving capabilities are then expanded with the addition of IMAQ with Vision and IMAQ Vision Builder. With these modules the additional VIs presented in Table E.1 are made accessible to the LabVIEW™ run-time environment.

Table E.1. Virtual instruments installed with LabVIEW™ IMAQ modules.

Image Acquisition Palette *(Vision...)* IMAQ Snap IMAQ Grab Setup IMAQ Grab Acquire IMAQ Close **Pixel Manipulation Palette** *(Vision-->Vision Utilities...)* *IMAQ Image To Array*	**Low-Level Palette** *(Vision-->Image Acquisition...)* IMAQ Configure List IMAQ Configure Buffer IMAQ Start IMAQ Fit ROI IMAQ Get Buffer IMAQ Extract Buffer IMAQ Copy Acquired Buffer IMAQ Stop IMAQ Status IMAQ Set User LUT
Image Management Palette *(Vision-->Vision Utilities...)* IMAQ Create IMAQ Image Bit Depth IMAQ Get Image Size IMAQ Get Image Info	**External Display Palette** *(Vision-->Vision Utilities--> External Display)* *IMAQ WindDraw* *IMAQ WindClose* *IMAQ WindShow* *IMAQ WindSize* *IMAQ WindSetup* *IMAQ GetPalette*
Files Palette *(Vision-->Vision Utilities...)* IMAQ Read File IMAQ Write File IMAQ Get File Info IMAQ Write BMP File IMAQ Write JPEG File	IMAQ Write PNG File IMAQ Write TIFF File IMAQ Write JPEG 2000 File IMAQ Read Image and Vision Info IMAQ Write Image and Vision Info

Installation of all additional LabVIEW™ modules is accomplished through automated installers on their respective data CDs.

In addition, two developed code libraries, Read_Excel_Values.llb and Dbl2usgned.vi, must be installed to allow the phase modulating system to read the optimized reference excitation parameters and convert double precision values to unsigned 8-bit precision, respectively. The latter library is required during the display and saving of processed interferograms due to limitations within the base IMAQ image output libraries.

A FireWIRE bus must be installed for control of the PixeLINK PL-741 monochrome CMOS camera. General control software for the camera system comes with device purchase; however, integration with the LabVIEW programming environment requires installation of VI libraries available from either the camera developers or included in the attached data CD. A list of these VI libraries is given in Table E.2.

Table E.2. Programming control blocks required for operation of the PixeLINK PL-741 monochrome CMOS camera system.

PxLLabVIEW.dll	ACQUISITION.llb
CAMERA_FEATURES.llb	Debug Examples 7.1.llb
Debug Examples.llb	Demo Examples 7.1.llb
Demo Examples.llb	DESCRIPTOR_CONTROL.llb
DETECTION.llb	ERROR_REPORTING.llb
GENERIC.llb	IDENTIFICATION.llb
INITIALIZATION.llb	LabVIEW_6.1_IMAQ_for_IEEE_1394_Examples.llb
PREVIEW.llb	TRANSLATION.llb

The developed code may work for other monochrome PixeLINK cameras; however, all other brands will require the replacement of the PixeLINK control blocks with code

available from that particular camera's developer. Control of the exposure cycle of the camera system requires the subsequent installation of National Instruments' PCI-6713 analog voltage output card. Installation software is available with purchase of this card. It is assumed that this card is connected to the interferometer as outlined in Table 4.1.

After installation of the required LabVIEW™ control libraries, the developed code may be copied with "excite.xls" to a readable working directory on the host computer. "Excite.xls" contains the modulation amplitude and phase information required to operation in a stroboscopic duty cycle range of 0 – 25% and is only read during operation of the phase modulating interferometer. The location of this file must be updated within the code block unless saved to the default location of "C:\Labview\Controls\" on the host system.

The stroboscopic modulation parameters within the developed code assume the use of the ThorLab's ITC 502, laser diode controller. In the event a different laser diode controller is needed, the default voltage-to-current proportion set in the voltage control section of the developed code, presented in Fig. D.1, must be adjusted from its default value of 20 mA/V to ensure proper operation. Similarly, Fig. D.22 contains the linear displacement rate of the attached piezoelectric device, calibrated using an algorithm presented in Hariharan, et al. [1987]. This parameter must be adjusted based on the currently attached piezoelectric actuator where units are specified as nm/V. With this installation procedure, the developed control systems can be run as outlined in Appendices F and G.

APPENDIX F. Standard operation flow chart

Presented in Figs F.1 to F.3 is an operational flowchart for nominal operation of developed software and user interface as described in Appendices C and G. Procedurally, Fig. F.1. initializes the camera and voltage output devices and allows the operator to align and focus on their object of interest. Figure F.2 begins the phase modulating once the user is satisfied with the optical focus and fringe contrast. Lastly, Fig. F.3 describes how the wrapped phase and/or optical modulation maps can be saved with the 4 phase-shifted interferograms required to recreate them. Textually, this flow can be described as by the following:

1. Enabling camera trigger signal and setting the base illumination to create a black unprocessed image feed signal.
2. Setting the modulation frequency, illumination duty cycle, and illumination amplitude modulation for viewing within the raw feed view. The image should appear with excellent contrast while maximizing the optical intensity range within the raw feed stream. This assumes that the focal and interferometric planes have been set coplanar and the object of interest is in focus.
3. Once all image settings appear appropriate, the wrapped phase and/or optical modulation maps can be viewed. If the wrapped phase map appears to have a non-smooth transition between its extreme values, the modulation amplitude can be adjusted in the “Operation Controls” tab. Small adjustments can be made to the modulation amplitude through the

spin control. However, optimization of the sine and cosine constants as outlined in Section 3 above will eliminate this need with a well calibrated, linear piezo-actuator.

4. If the resultant phase/modulation maps appear appropriate, the results can be saved to the directory and file of choice. When selecting the save directory, press "Select Cur. Dir." to ensure the current directory is properly selected for saving. File type can be set as indicated in Appendix F. "Data Acquisition Count" can be adjusted to save multiple sequential data sets for comparison and post-processing.
5. If an error occurs during operation, an error dialog will appear. Select "Stop" to end the program safely and attempt to restart code. If error persists, restart LabVIEW™ and continue testing. If the camera or output card is not properly released by selection of the in-program "Stop" or the in-error "Stop," LabVIEW™ will incorrectly read the connected hardware disabling camera control or creating a DC-offset to the output voltage signals respectively.
6. If the interface freezes after a user command, wait for 30s – 1 minute. If function has not been restored, force a LabVIEW™ close and restart program. System will restart and operate correctly with forced restart.
7. End program through the in-program "Stop."

Automatically input parameters from:

1) Camera memory
2) Modulation parameter file
3) Default settings within LabVIEW™ block

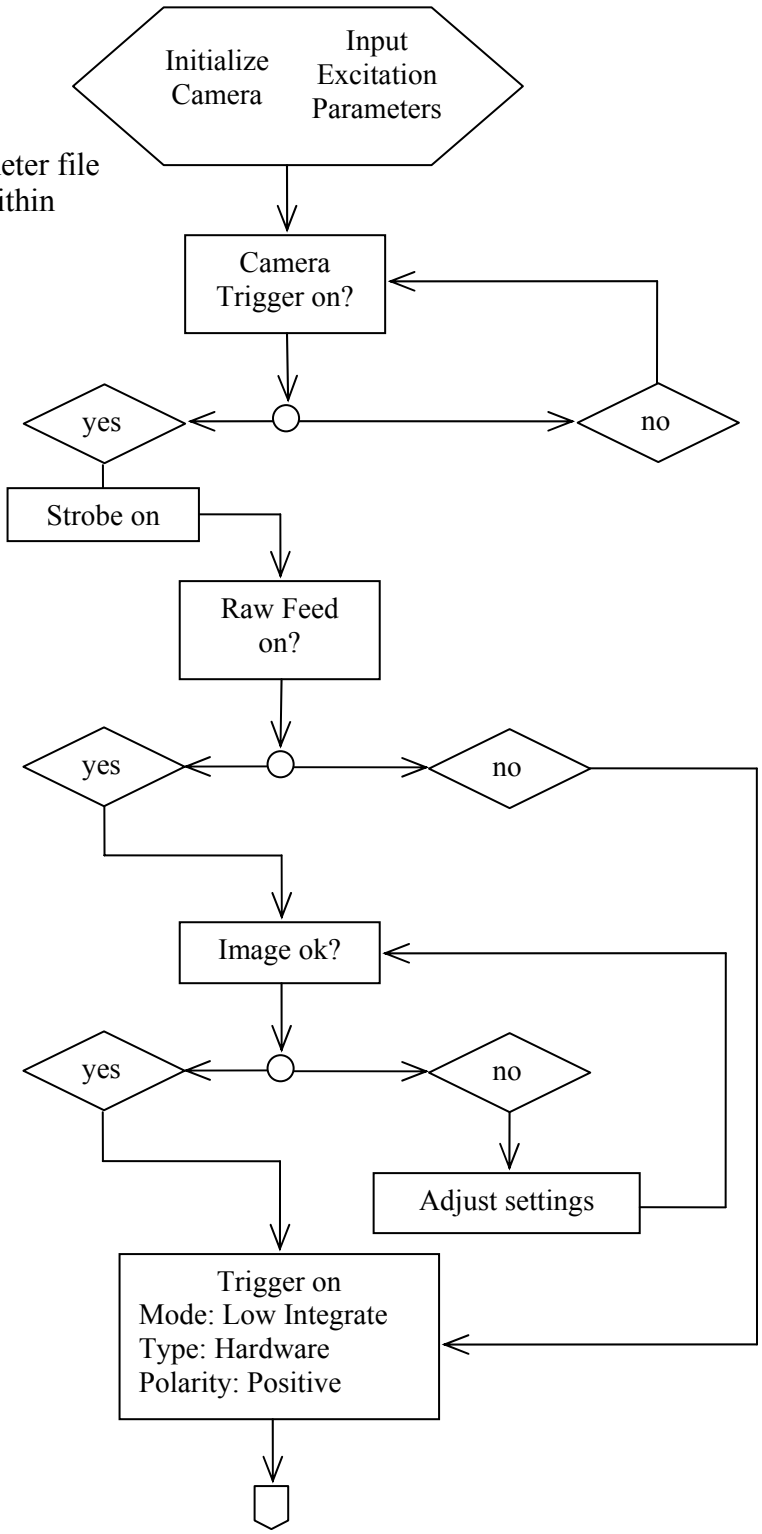

Fig. F.1. Turn on the developed code and ensure that the raw camera feed is ready for processing.

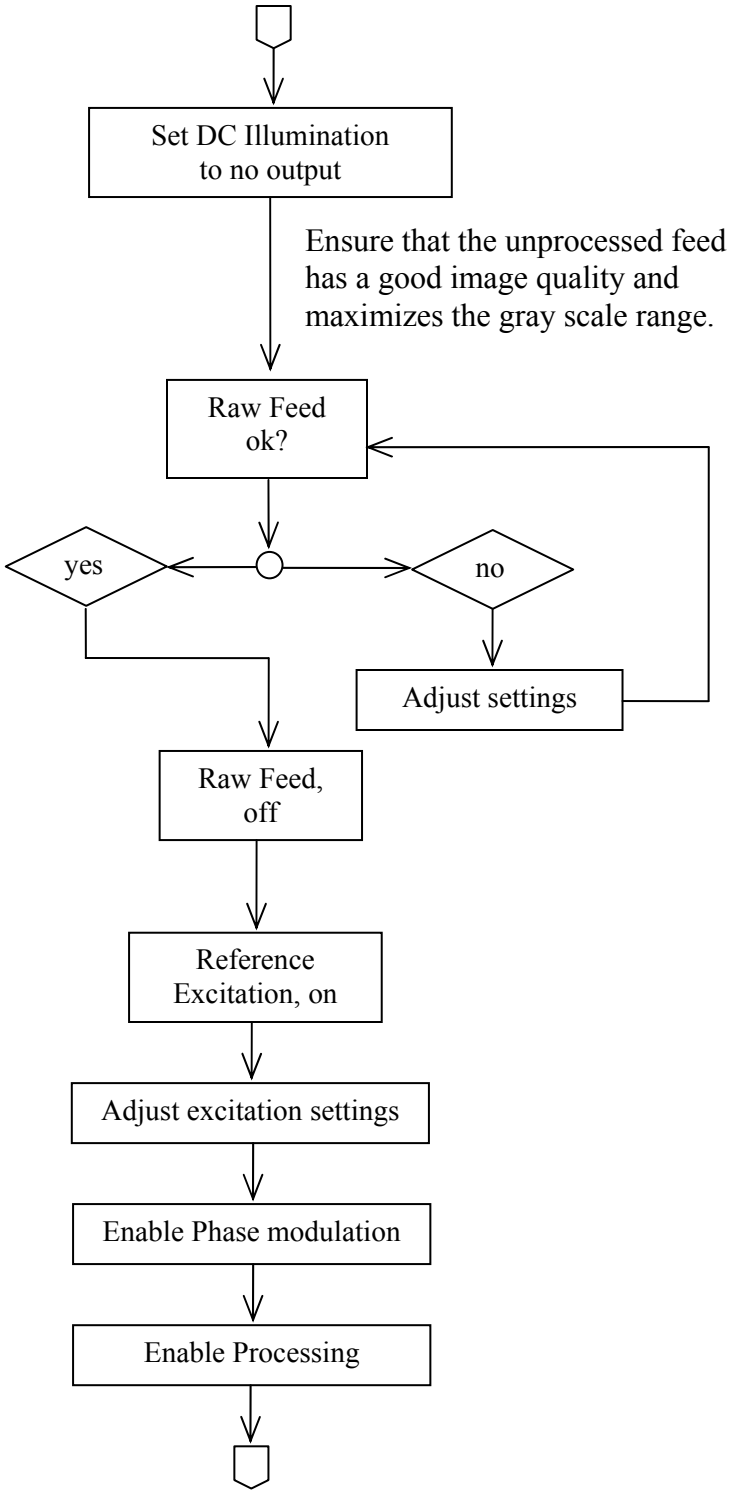

Fig. F.2. Remove the DC component of the illumination signal and begin modulation output control for image processing.

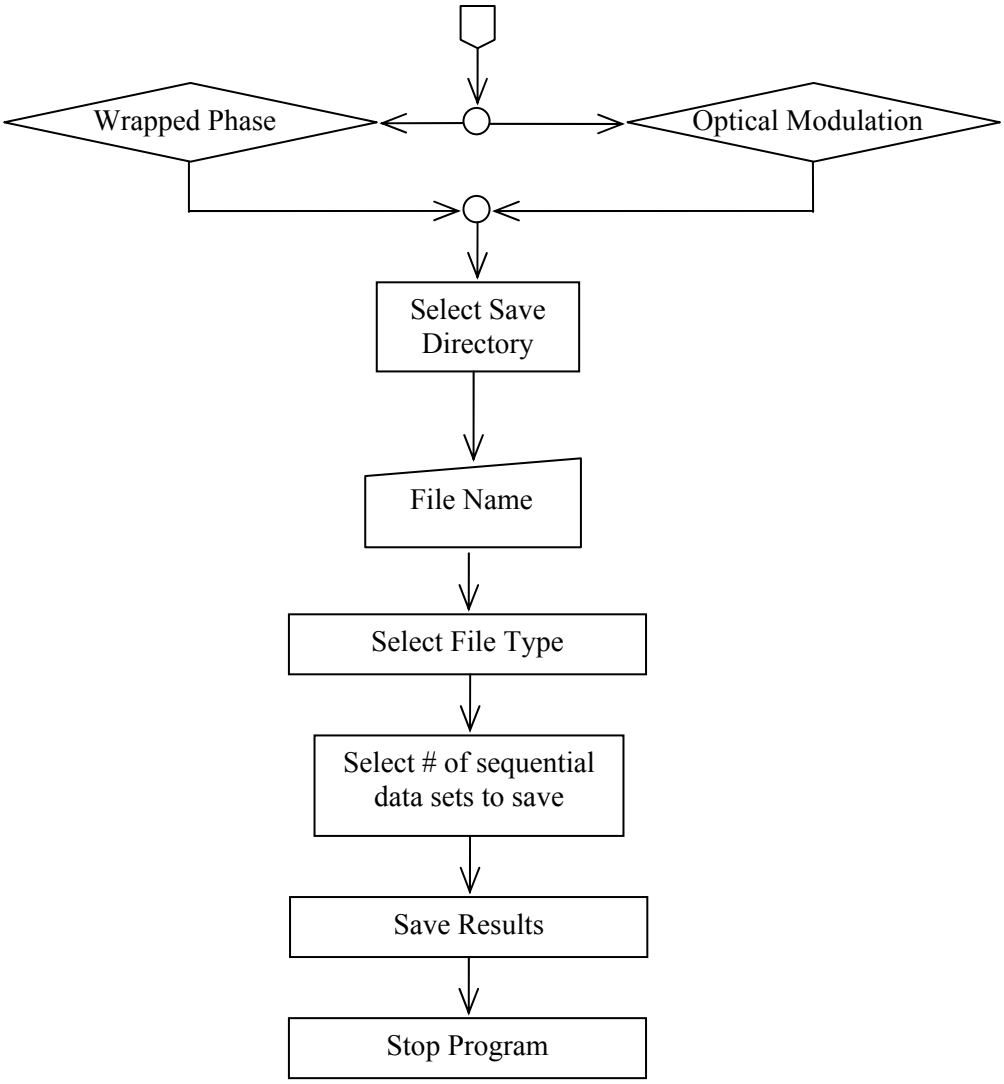

Fig. F.3. View the wrapped phase map or the optical modulation map and save the results to the selected directory. End the program using the implemented program stop.

APPENDIX G. Detailed description of developed user interface

Program Stop:

- Stops the program. Only end the program with this button or in the optional stop when an error occurs. If the program is ended any other way, the camera will not be properly released and so will not run again until LabVIEW™ is restarted.

Program Error - Displays that an error has occurred during the current operation.

Control Block:

Instrument Control:

Camera Trigger - Begins sending a trigger signal to the camera attached to Channel 2 of the NI PCI-6713 card. Must be enabled before any other settings are adjusted whether or not it will be required for the particular mode of operation.

Raw Feed - Displays the raw feed from the attached camera system. This will only display correctly when the system is set to a square ROI.

Strobe - Sends the illumination modulation signal through Channel 1 of the NI PCI-6713 card.

Excitation - Sends the reference excitation modulation signal through Channel 0 of the NI PCI-6713 card.

Wavelength 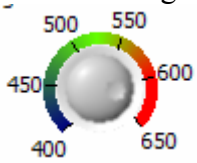

- Set to the primary wavelength of the illumination source for scaling the excitation modulation amplitude.

Processing Control:

Enable Phase Stepping - Begins stepping the relative phase between the illumination and excitation modulations for optical phase extraction.

Phase Step

- Displays the current relative phase between the illumination and excitation cycles

Enable Processing - Allows for image processing to occur.

Wrapped Phase Map - Displays the wrapped phase map if *Enable Processing* is on.

Modulation - Displays the optical modulation map if *Enable Processing* is on.

Reference Mode - Enable double-exposure mode.

Acquire Reference - Acquire the reference image set.

Operation Mode:

Tweak Ref. Mirror Excitation

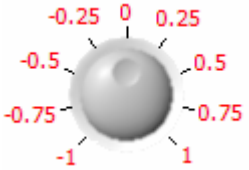

- Normally set to 0, allows for a small change in the reference mirror excitation amplitude.

Plot Line

- Plots the midline of the wrapped phase or modulation map on the line graph displayed. This plot will alternate between the two maps if both are displayed.

Line Selector

- Determines if the midline shown is along the row or the column of the wrapped phase or modulation image.

Settings block:

Camera Control:

Shutter

- Controls the shutter acquisition time of the camera when in free run mode, in ms. Not used otherwise.

Gain

- Adjusts the signal amplitude of the camera system at the expense of increasing the noise level by a similar amount, default: 0

Gamma

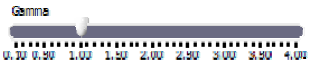

- Affects the brightness of mid-level tones in an image by: output = input^{gamma}

Region of Interest

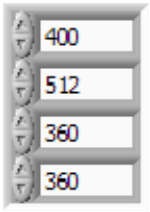

- Sets the region of interest (ROI) of the camera view

Left:	Distance from the left edge of the CMOS
Top:	Distance from the top edge of the CMOS
Width:	Width of display window
Height:	Height of display window

Width and Height values will default to a multiple of 8 & must be equal for proper image display.

Pixel Addressing Value

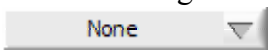

- None / Every 2nd Pixel; Sets the pixels read in addressing mode

Pixel Addressing Mode

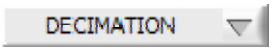

- None / Decimate; Decimate only displays every Nth pixel as defined in the pixel addressing value

Voltage Control:

Frequency

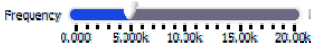

- Set the primary excitation modulation frequency (Hz), related to the camera trigger and stroboscopic illumination frequencies as seen in the block diagram. Normal operating range: 50 – 100 Hz.

S. Amplitude

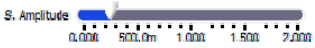

- Sets the amplitude, in Volts, of the modulation signal sent to the illumination source. The modulation automatically ranges from 0.02 V to 2.00 V.

Current Change

- The maximum change in illumination current, assuming use of Thor Labs ITC-502.

Duty Cycle

- Sets the integration period of the camera and the length of the strobe signal as a percent of the reference excitation period. Static measurement operation: set to 14%

Phase

- Adjusts the relative phase between the illumination and excitation signals, Default: 0.

Triggering:

Trigger

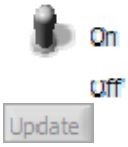

- Enables reading of the trigger signal pin by the camera.

Trigger Mode

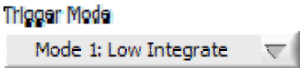

-

Mode 0: Low Trigger	Acquires when the trigger signal reaches the camera for the set shutter speed.
Mode 1: Low Integrate	Acquires while the trigger signal is low, must be set for proper operation
Mode 2: Integrate, N Trigger	Acquires for N trigger signal periods.
Mode 3: I. Trigger, N x FPS	Acquires N times at the set shutter speed.
Mode 4: N Frame Capture	Acquire N frames when the trigger signal reaches the camera

Trigger Type

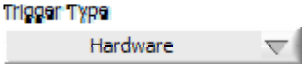

- Hardware/Free Running, Default: Hardware

Trigger Polarity

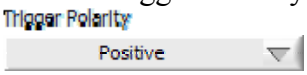

- Positive/Negative, defines which side of the signal pulse to trigger on. This parameter should be:
Positive – Sinusoidal Phase Modulation
Negative – Phase Stepping

Trigger Delay

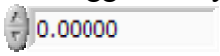

- Delay acquisition for #### ms, Default: 0 ms

Trigger Parameter

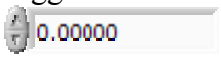

- Sets the value of N for the above modes. Must be >0 for Modes 2-4

Excitation Period Count

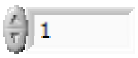

- Sets the minimum number of reference excitation periods per phase step, Default: 1

Integration Time

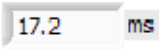

- Integration time of the camera at current settings.

Frame Rate

- Maximum possible frame rate at current settings.

Trigger Frequency

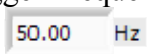

- Frequency of the camera trigger signal.

Cycle Time

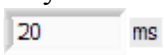

- Period of the camera trigger signal

Results Block:

Save Results:

Complete Path

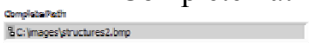

- Displays the current save path & most recently saved file.

Directory

- Select the directory to save the acquired images to. On the pop-up selector, be sure to click "Select Cur. Dir." to set the directory properly.

File Name

- Base save file name

File Type

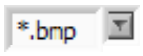

- Type of image file:
*.bmp, *.jpeg, *.tiff, *.png, *.aipd

Data Acquisition Count

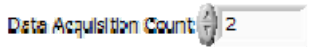

- Number of sequential data sets to automatically save.

Begin Save Sequence

- Save the files

Data Processing: (not enabled)
Image Analysis: (not enabled)